Co-phasing segmented mirrors: theory, laboratory experiments and measurements on sky

Isabelle Surdej

München 2011

Co-phasing segmented mirrors: theory, laboratory experiments and measurements on sky

Isabelle Surdej

Dissertation
an der Fakultät für Physik
der Ludwig–Maximilians–Universität
München

vorgelegt von
Isabelle Surdej
aus Liège, Belgien

München, den 15. Juli 2011

Erstgutachter: Priv. Doz. Dr. Andreas Glindemann
Zweitgutachter: Prof. Dr. Wolfgang Zinth
Tag der mündlichen Prüfung: 10. Oktober 2011

Acknowledgements

First and foremost, I want to express my deepest gratitude to my supervisor, Lothar Noethe. His scientific and pedagogic competence, and his meticulousness have largely contributed to the present work. I am indebted to him for encouraging me to pursue this PhD, for all the freedom and trust he offered me to conduct this work, for all his precious remarks during the last weeks of the thesis, and for guiding my steps, from the supervision of the diploma thesis to the conclusion of my PhD studies. My admiration for him goes beyond scientific aspects: his idealistic vision of the world, his modesty, his sensibility and kindness are for me a source of personal enrichment.

My utmost gratitude goes to Priv. Doz. Andreas Glindemann for accepting with enthusiasm to be my supervisor and for his valuable comments on this dissertation.

I would also like to show my gratitude to Prof. Dr. Wolfgang Zinth, Prof. Dr. Thomas Preibisch, Prof. Dr. Ralf Bender, and to Priv. Doz. Dr. Markus Kissler Patig, members of my thesis committee, for accepting to read and evaluate this work.

This work would not have been possible without the help of Natalia Yaitskova. First, her outstanding scientific research has contributed to the basis of the work presented in this thesis. She has introduced me to the world of scientific research, continually encouraged me, advised me, motivated me and inspired me, as a colleague but also as a friend. Working with her in the laboratory and on more theoretical aspects was often very exciting, and it was very stimulating and a real pleasure to work with her. All the long nights spent together observing at the telescope are unforgettable. Throughout the years, she became much more than a colleague, a very precious friend.

I am forever indebted to Robert Karban. When I started at ESO, he has guided me during the whole APE project, he has given me responsibilities, he encouraged me when I needed it the most, and was always there for me in more difficult moments. I thank him for the exceptional amount of time and his infinite patience to teach me all I know about programming, and guiding me through all the data analysis software of APE, the famous universal generic phasing library. It was such a pleasure to work with Robert, and he became very fast an irreplaceable and faithful friend, but also a triathlon partner and coach.

I would like to thank also Frédéric Gonté. First, the APE experiment would not have been such a success if it wasn't for him. The APE bench was in optimal conditions to deliver high quality scientific data. He pushed every one from the team to do hist best, and guided the whole APE team towards a real success. But also, he was a very nice person to work with, very devoted and stimulating, and many ideas from our discussions are present throughout this work. I also thank him for his patience with me on an optical bench.

Lothar, Natalia, Robert, and Frédéric have guided me at ESO since I arrived, and everything that I have learned during these years, from software to Fourier optics, through optical alignment,

active optics, SysML, and also non-scientific aspects, I owe it to them.

I owe my deepest gratitude to Roberto Tamai for always supporting me and giving me the opportunity to do this PhD thesis.

I also want to thank Philippe Dierickx for giving me the opportunity to come to ESO and to work on so exciting projects, as APE and the E-ELT. His generosity and kindness have always provided me a fantastic source of comfort. I have spent an unforgettable time at ESO, and I hope, some day, to be involved again in very exciting projects, with nice and interesting people around.

I would like to express my warmest thanks to the wonderful APE team, which created a great working atmosphere, in Garching but also in Paranal, and probably as well at the guest house, during our unforgettable PISCO (PIStON COrrection) meeting.

It is an honor for me to thank Frédéric Derie who has always been so positive and who has given me responsibilities within the APE project.

I would also like to thank Gary Chanan and Mitchell Troy for all the stimulating discussions and the very precious collaboration.

This thesis would not have been possible without the LAM and IAC who were fully involved in the concept, the design, the alignment, and the validation of the ZEUS sensor. I would like to show my deepest gratitude to Kjetil Dohlen who is the inventor of the Zernike Phase Contrast Sensor but also to Arthur Vigan and Silvio Mazanti who have greatly contributed to this project.

Working with Reynald Bourtembourg, Bruno Luong, Alfio Puglisi and Ruben Mazzoleni has always been a real pleasure and encouraging for the great working atmosphere they have created. All those hours we have been hypnotized by the 4 CCDs of the Internal Metrology. I can never thank enough Bruno Luong who has helped me find a bug in my software, and all the outstanding work he has done with the Internal Metrology.

Even if he said he never had the time, Christophe Dupuy would always help as much as he could, and his magic fingers would align everything, and it was always a pleasure to have a chat with him.

I would like to acknowledge the rest of the APE team: Luigi Andolfato, Constanza Araujo, Roland Brast, Philippe Duhoux, Christophe Frank, Julio Navarrete, Marcos Reyes, Sergio Chueca, Enrico Pinna, Simone Esposito and Fernando Quiros Pacheco.

Of course, I would like to thank all my friends, that make me go ahead in life, everyone in his own way ... Babak, Judith, Jérôme and Natalia, Kurt and Bet, Céline, Marc, Philippe and Almudena, Fernando, Robert, Bérénice, Emilie and Vincent, Virginie, Elise, Pierre and many, many others.

Last but not least, I want to thank all my family, for all their love, their support and their stimulation. A special thanks to the grand-parents who accompanied Romain and me to Munich several times. I finally have the opportunity to thank my parents for giving me their infinite love which gives me the energy to go beyond my limits.

I will not finish without a special note for Marin and Romain, who have been very patient with me during these last days of intensive work. I owe all my positive energy to them. They illuminate every moment of my life.

Contents

Abstract

Future Extremely Large Telescopes (ELTs) will be segmented. To achieve the desired image quality, in particular for high contrast imaging, the segments of the primary mirror must be phased to an accuracy which corresponds to a small fraction of the observing wavelength.

Information on the misalignments of the segments of the primary mirror will be provided with a phasing camera. The Zernike phase contrast method is a novel technique to phase the primary mirrors of segmented telescopes.

The present thesis aims at studying the phasing of segmented mirrors using the Zernike phase contrast method. The theoretical background of this sensor and the algorithm used to retrieve the piston, tip, and tilt information are described.

The Zernike Phase Contrast Sensor has been tested in the laboratory and on-sky on a Unit Telescope of the ESO Very Large Telescope with a segmented mirror conjugated to its primary mirror to emulate a segmented telescope. The performance of the sensor as a function of various parameters such as star magnitude, seeing, and integration time is discussed.

The phasing accuracy obtained on sky has always been below 15 nm root mean square wavefront error under normal conditions of operation. Equivalent limiting star magnitudes of 18 and 15.7 achieved in the laboratory and on-sky, respectively, with this sensor would be sufficient to phase segmented telescopes in closed-loop during observations.

Part I

Introduction

Chapter 1

Introduction

The year 1609 signalled a true revolution in astronomy with the first use of a refracting telescope for astronomical observations by Galileo Galilei. In 1669, Isaac Newton introduced the first reflecting telescope, with a parabolic primary mirror. The refractive and reflecting design concepts have then been competing against each other for the following 300 years. For apertures larger than 1 meter, the reflecting telescopes have proved to be the most efficient, in particular since reflecting telescopes are exempt of chromatic aberrations.

Since then, the need to study fainter objects with higher resolution has led to telescopes with larger aperture diameters. The evolution of telescope aperture diameter over the last 400 years is illustrated in Figure 1.1. The diameter of the largest telescopes doubles about every 40 years. The 20- to 30- meter class telescopes planned for the 2015 time frame display a somewhat faster growth rate than the historical trend [3].

In the 1980s and 1990s, many technological advances have been made that allowed scientists to build larger telescopes. These included computerized design, faster and improved optical figuring techniques, the use of the altitude-azimuth configuration to reduce the mass and cost of telescope mounts, and faster focal ratios of the primary mirrors for smaller domes and buildings [3]. Also the invention of active optics on thin meniscus mirrors has had a major impact on this new generation of telescopes. This technology has been tested for the first time on the 3.5 m primary mirror of the New Technology Telescope in 1989. The fundamental advantage was that the residual intrinsic stiffness, which was required in passive telescopes to cope with the inaccuracies of the forces applied by the astatic supports, could now be reduced even further, which made the fabrication of telescopes with mirror diameters of 8 m feasible and affordable [58].

The positive results obtained with the active optics developed on the NTT served as a baseline for the design of the four Unit Telescopes (UT) of the *Very Large Telescope* (VLT), which were completed between 1998 and 2001. Similarly, the *Gemini* observatory consisting of two 8.1-meter telescopes located in Hawaii and Chile, was completed in 2000 as well as the *Subaru* telescope in Hawaii, with a primary mirror of 8.2 meter, which started to take scientific images in 1999.

An increase in telescope size does not only improve the amount of collecting area, which allows the observation of fainter objects, but also affects the angular resolution of

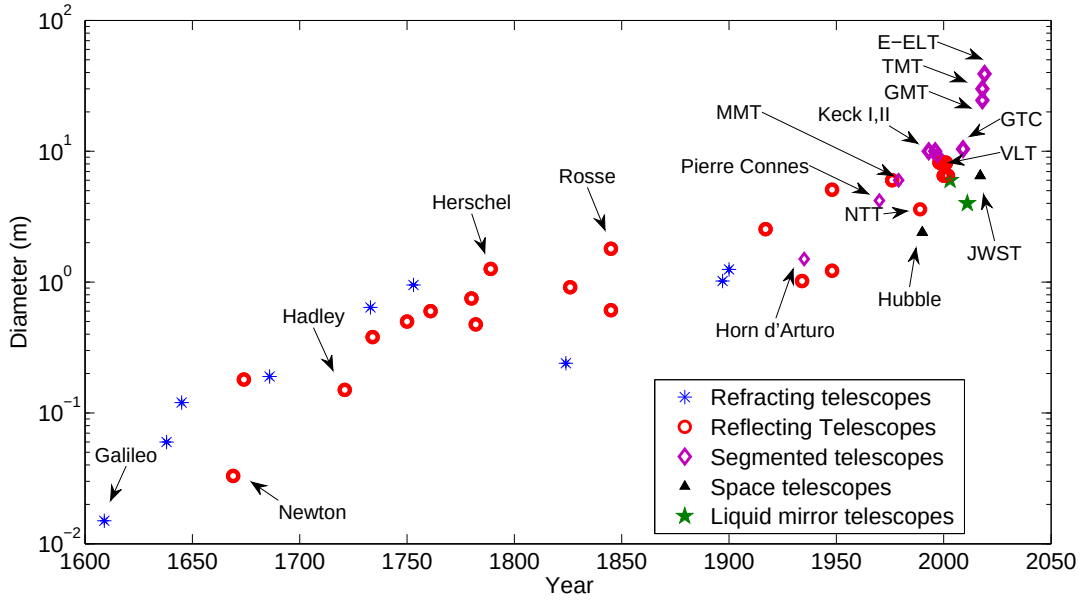

Figure 1.1: Evolution of telescope aperture diameter in time. Adapted from [3], [61].

the astronomical target observed. This is only true for diffraction limited observations. In the presence of atmospheric turbulence, the resolution is limited by the seeing disk. Gains in resolution were made possible by moving the telescopes to better sites, by going into space, or even by compensating the effects of the atmospheric turbulence with adaptive optics.

Building a giant telescope from a monolithic mirror presents many difficulties. These difficulties typically grow rapidly with the increasing size, and quickly make monolithic mirrors impractical [55]. One solution to build telescopes with primary mirror diameters larger than 8 meter is to construct segmented primary mirrors. Segments are much easier to fabricate, transport, install, and maintain than large monolithic mirrors. However, new problems arise with segmentation: the segments are difficult to polish, they need active position control, the edges of the segments and the gaps produce diffraction effects, and there are more degrees of freedom to control which leads to an increase in complexity [55].

Before the very successful Keck telescope, different attempts to build segmented telescopes had been undertaken.

- In 1932, Horn d'Arturo in Italy made a 1.5 m mirror, which could only be used facing zenith [55].
- Pierre Connes in France made a 4.2 m segmented mirror telescope for infrared astronomy. Unfortunately, the optical quality was too low to be useful for astronomy [55].
- The MMT, before the conversion of its primary mirror to a monolithic one, has been in operation between 1979 and 1998 with 6 mirrors, each with a diameter of 1.8 m.

Figure 1.2: The first three segmented telescopes: The mirror of Horn d'Arturo (Courtesy of J. Nelson [55]), the segmented telescope of Pierre Connes (Courtesy of [52]) and the MMT (Courtesy of [53]).

In the late 1970s, a very ambitious idea to build a telescope with a segmented 10-meter diameter primary mirror was initiated [55]. The primary mirror of the Keck telescope is made of 36 hexagonal segments. This project officially started in 1984 and was completed in 1993. Due to the success of the telescope, a second identical telescope has been built and saw first light in 1996. Both telescopes can be combined and used for interferometry.

In 1997, the *Hobby-Eberly Telescope* (HET), a telescope with 91 segments polished spherically to form an effective 8-meter telescope, was completed in Texas. With a very similar design, the *South African Large Telescope* (SALT) saw first light in 2005.

The Spanish project *Gran Telescopio Canarias* (GTC) [1] saw first light in 2009 and is today the world's largest single-aperture optical telescope. This telescope is based on a design very similar to the Keck, with 36 segments and an equivalent primary mirror of 10.4 meter.

The desire to build ever larger mirrors did not come to an end here. Even more challenging telescope projects, of more than 20-meter in diameter, all of them with segmented primary mirrors, are currently in their design phase: the *Thirty Meter Telescope* (TMT) [56], the *Giant Magellan Telescope* (GMT) [42], and the *European Extremely Large Telescope* (E-ELT) [31].

These three telescope projects are part of a new class of telescopes: *the Extremely Large Telescopes*.

1.1 Extremely Large Telescopes

1.1.1 Thirty Meter Telescope (TMT)

The TMT project began after the merging of three earlier large-telescope projects: the California Extremely Large Telescope, which was a partnership between Caltech and the University of California; the Very Large Optical Telescope, led by ACURA; and GSMT, the Giant Segmented Mirror Telescope, which was a partnership between the National Optical Astronomical Observatory (NOAO), and the Gemini Observatory [76].

On April 1 2009, TMT officially entered in Early Construction Phase and is expected to see first light in 2018 (Fig. 1.3), on Mauna Kea, in Hawaii.

The optical design of the telescope is a folded Ritchey-Chrétien. The thirty meter primary mirror consists of 492 hexagonal segments with diameters of 1.44 meter from corner to corner. The segments are closely spaced, with gaps between the segments of only 2.5 mm.

The secondary mirror has a diameter of 3.1 meter and converts the focal ratio of 1 of the primary mirror to a focal ratio of 15 for science instruments.

The elliptical tertiary mirror has diameters of 3.6 and 2.5 meter. The M3 mirror can be rotated around a vertical axis to direct the light beam into the scientific instruments mounted on the Nasmyth Platforms [56, 57].

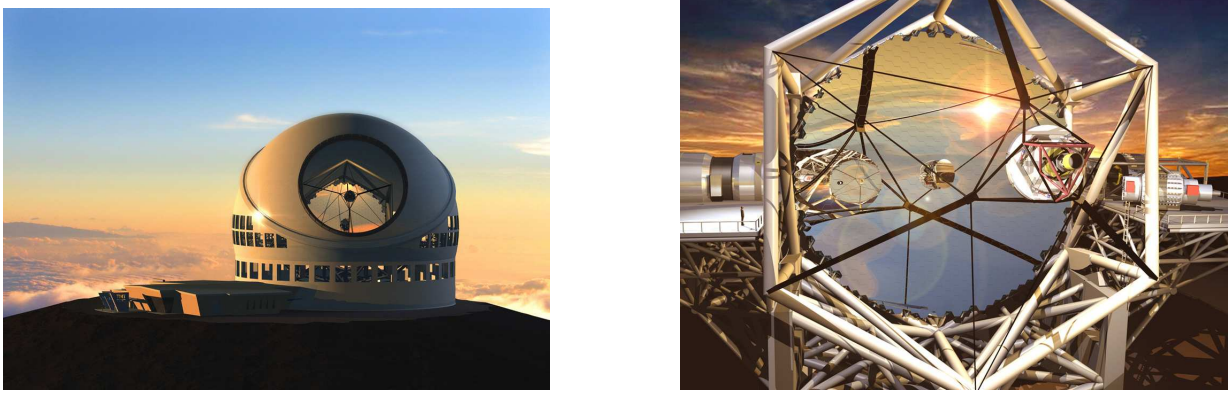

Figure 1.3: Left: The Thirty Meter Telescope on Mauna Kea in Hawaii and its spherical dome with a calotte design. Right: The segmented primary, the secondary and the tertiary mirrors. Courtesy of [76].

1.1.2 Giant Magellan Telescope (GMT)

The design of the GMT is unique within the class of Extremely Large Telescopes. The optical design is based on a Gregorian telescope [42] with a primary mirror comprised of six off-axis circular mirrors and a central mirror on axis. Each mirror has a diameter of 8.4 meter. The equivalent collecting area is that of a 21.4 meter telescope and the resolving power is that of a 24.5 meter aperture.

The secondary mirror (M2) is also segmented with seven thin adaptive shells for adaptive optics operation. Each of the seven 1.1 meter M2 segments maps to a single primary mirror segment. This arrangement greatly simplifies the alignment of the telescope optics: the primary mirror segment misalignments are compensated by the motions of the more agile M2 shells [42].

The GMT is expected to see first light in 2018. It will be erected in the Las Campanas Observatory, in Chile.

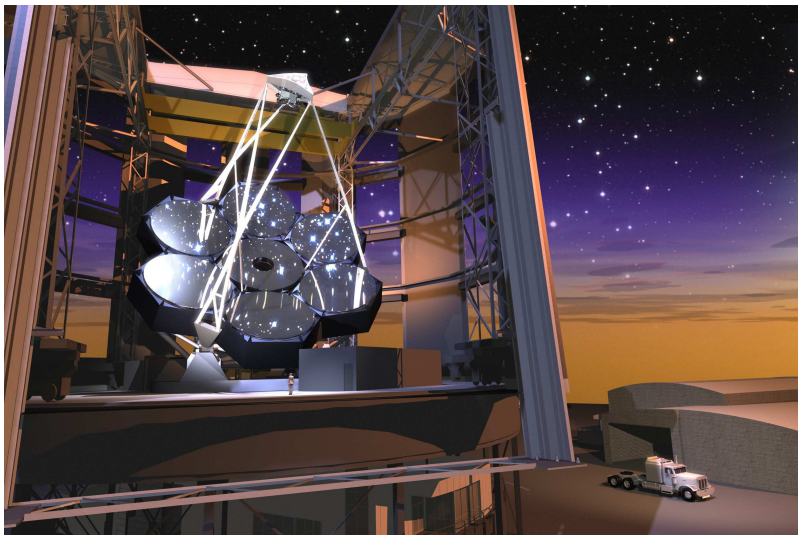

Figure 1.4: View of the GMT with its primary mirror made of 7 circular segments of $8.4m$ each.

1.1.3 The European Extremely Large Telescope (E-ELT)

ESO studied the concept of the Overwhelmingly Large Telescope (OWL) [19], with an optical design based on a 6 mirror solution, with a spherical primary of 100 meter, a flat secondary and a corrector consisting of 4 elements, including two 8 meter class active mirrors and two adaptive mirrors, of 2.3 meter and 3.2 meter (M6 and M5, respectively) [27]. The primary and secondary mirrors of the OWL would have been segmented with 3048 and 216 segments respectively. However, substantial technical risks were identified, associated especially with the large segmented secondary mirror. The estimated cost was also too high. It was then decided to proceed with a detailed design phase aiming for a smaller primary diameter, a less complex and less risky telescope. In 2007, a new concept was born, with a primary mirror of 42 meter, the European Extremely Large Telescope (E-ELT).

The optical design of the E-ELT is a 5 mirror design [31] shown in Figure 1.5:

- three powered mirrors to improve the optical correction over a larger field (10-arcminute field of view): M1, M2 and M3.

- two additional folding flat mirrors to steer the beam to the Nasmyth foci: M4 and M5.

The segmented aspheric primary mirror will measure 42 meter with 984 hexagonal segments of 1.45-m (corner to corner). A new option with a 39 meter primary mirror (the two external rings would be removed) is also considered today. The pupil of the telescope is the primary mirror. The convex secondary mirror will measure six meter (and only 4 meter for the 39 meter design) and the tertiary mirror four meter.

Adaptive optics is embedded inside the telescope by means of M4 which is a deformable mirror of 2.6 meter. M4 is naturally conjugated to the ground layer of the atmosphere and

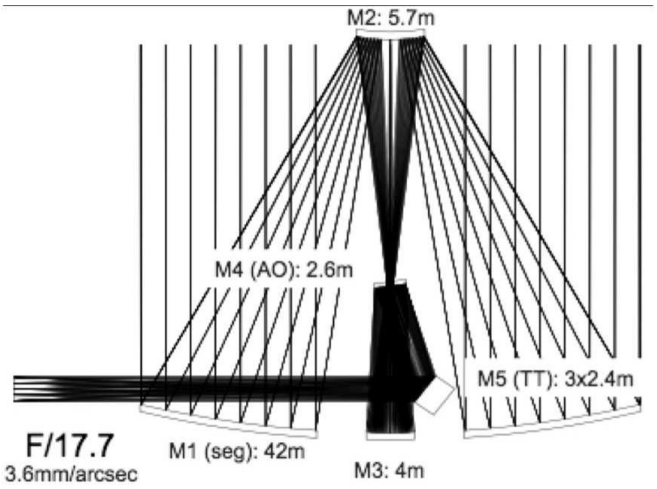

Figure 1.5: The 5 mirror optical design of the E-ELT.

inclined at 11 degrees. Embedding adaptive optics (AO) into the telescope is a natural evolutionary step in the design of telescope.

The 5th mirror, a flat tip-tilt mirror of 2.7-m in diameter located near the pupil, redirects the beam to the f/15 Nasmyth focus. The fifth mirror is envisaged to provide for field stabilization of the telescope beam. A simultaneous rotation of the fourth and fifth mirror around the axis through the centers of the first three mirrors allows access to either of the two Nasmyth foci.

An artist's impression of the future E-ELT can be seen in Figure 1.6.

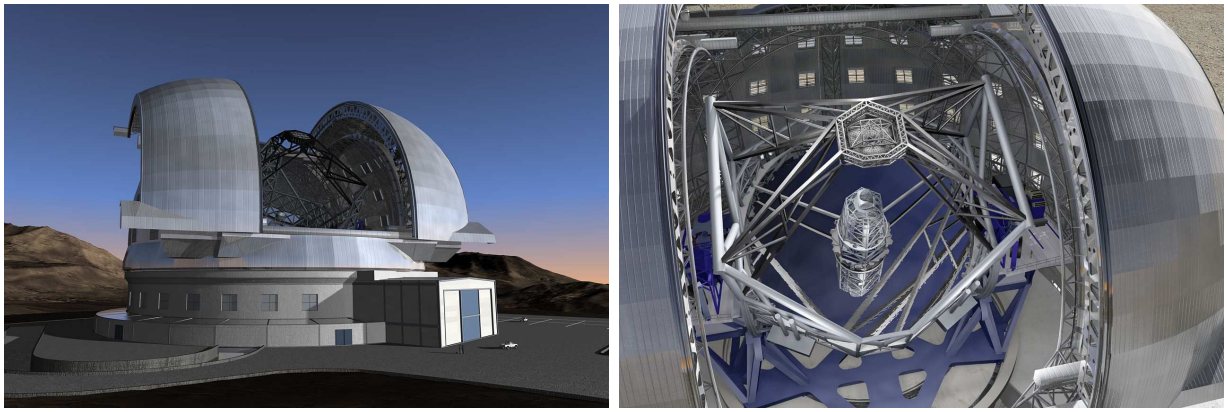

Figure 1.6: Left: The E-ELT and the dome. Right: View inside the telescope.

The Council of the European Southern Observatory selected Cerro Armazones in Chile (Figure 1.7) as the baseline site for the E-ELT.

Figure 1.7: View of Cerro Paranal (VLT) and Cerro Armazones (E-ELT). Cerro Paranal is in the lower right, and left is the VISTA telescope. Cerro Armazones is the peak in the middle on the left. In the background, the volcano Llullaillaco (6739 m). Courtesy of [24].

1.2 Space telescopes

For ground-based observations, the main limitation comes from the atmosphere. The wavefront emitted by a distant star is perturbed by the different layers in the atmosphere and the resolution of the telescope will not be limited by its optical design but by the seeing disk. Moreover, the atmosphere acts as a window for ground-based observations, absorbing the ultraviolet, X and gamma-rays and being transparent only to a small part of the electromagnetic spectrum, i.e. the visible, the near, mid and far infra-red, and radio wavelengths. Last but not least, in space, instrumental stability is excellent. Apart from thermal variations, space offers a more stable environment, e.g. no disturbances are induced by the wind [3].

Going to space presents many advantages over ground-based observations. One of the most famous examples of space telescopes is the Hubble Space Telescope (HST), launched in 1990, which covers wavelengths from the near ultra-violet to the near infrared. However, the telescope was only real success three years later, after the installation of COSTAR, a system designed to correct for the spherical aberration of the 2.4 meter primary mirror.

The planned successors of HST are the James Webb Space Telescope and, much further out, the Advanced Technology Large-Aperture Space Telescope (AT-LAST). AT-LAST is a proposed 8 to 16-meter optical space telescope, which would be a true replacement and successor for the Hubble Space Telescope (HST).

The *James Webb Space Telescope* (JWST) is a space telescope designed for infrared imaging and spectroscopy. The novelty of this telescope is that the 6.2 meter primary mirror will be made of 18 independent, hexagonal mirror segments [16].

The primary mirror will be in a folded configuration during the launch and deployed

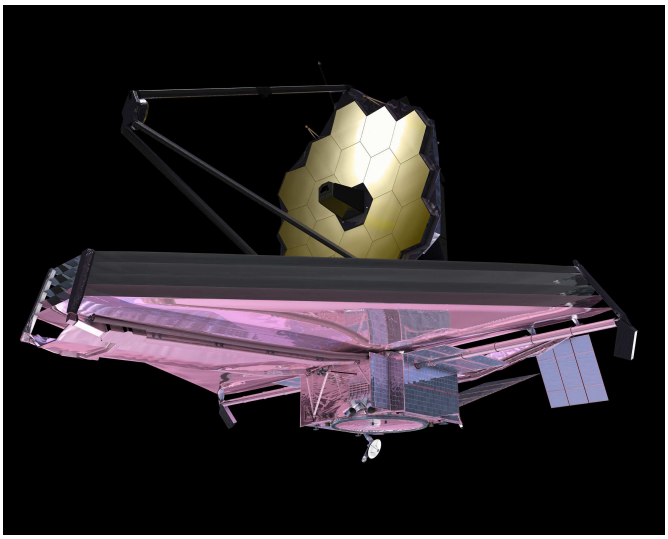

Figure 1.8: The James Webb Space Telescope.

in space. The alignment of the primary mirror with the secondary mirror will be done in orbit.

1.3 Outline of the thesis

Chapter 1 has presented a brief history of telescopes and how this led to the segmentation of the primary mirrors of current and future telescope projects.

However, new problems arise with segmentation. The misalignments of the segments in piston, tip and tilt, the misfigure of the edges of the segments, the inter-segment gaps, the aberrations of individual segments, and the variations in reflectivity between the segments, all these effects will affect the image quality of a segmented mirror. The telescope errors, introduced by segmentation are presented in Chapter 2. The requirements on the alignment of the segments, in particular for applications such as high-contrast imaging, are defined in Section 2.2. To achieve these stringent requirements, the segments must be actively controlled by means of a control loop between edge sensors and position actuators (Section 2.3). However, the edge sensors require a periodic calibration of their readings, which is achieved with an optical phasing sensor (Section 2.4).

In Chapter 3, different concepts of phasing sensors are presented. Four of them, the curvature sensor, the pyramid sensor, the Shack-Hartmann type phasing sensor and the Zernike Phase Contrast Sensor, have been tested in the laboratory and on sky at the VLT, in the framework of the Active Phasing Experiment (APE) (Chapter 4).

The Shack-Hartmann type sensor has been successfully used for the phasing of the Keck telescopes. While this technique is optimal for a 10 meter class telescope, the fine alignment required between the sensor and the pupil of the telescope will be harder to achieve in an ELT, with possible distorsions of the pupil. Therefore, in the framework

of the Active Phasing Experiment, alternative techniques have been investigated. One of them, the Zernike Phase Contrast Sensor, constitutes the main topic of the present Ph.D. thesis. Part II is dedicated to this sensor.

In Chapter 5, a theoretical study of the Zernike Phase Contrast Sensor, using Fourier optics, is presented. All the algorithms which have been implemented to test the sensor in the framework of APE are discussed in Chapter 6. The results obtained in the laboratory and on sky, are shown in Chapter 7 and Chapter 8, respectively. Finally, in Chapter 9, the results obtained on sky are analyzed with a complementary approach, based on the use of the diffraction theory for segmented mirrors.

Chapter 2

Image quality of a highly segmented mirror

Segmentation has enabled astronomers to build larger and larger telescopes. However, as already mentioned in the introduction, new problems arise with segmentation. For a segmented system to deliver an image quality comparable to that of a monolithic telescope, the segments have to be coaligned, cofocused and cophased (Figure 2.1). Coaligning consists of stacking the images produced by the individual segments, cofocusing ensures that the focal length of all the individual segments is the same, and cophasing (or phasing) ensures that there is no piston discontinuity between the edges of neighboring segments [3].

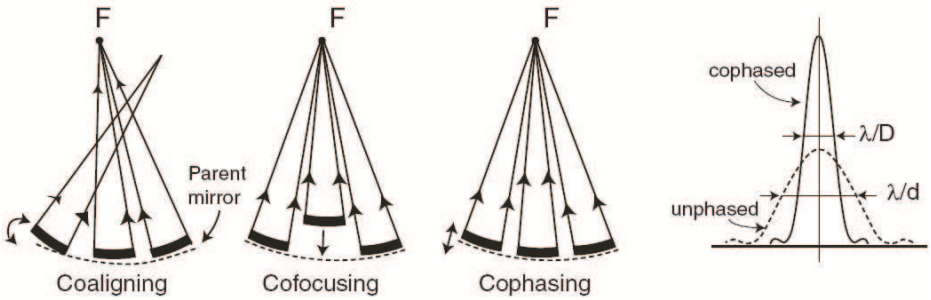

Figure 2.1: Left: Coaligning, cofocusing, and cophasing a segmented system. Right: the PSF of a segmented system where the mirror segments are unphased or phased. The width of the PSF is λ/d in the first case, where d is the diameter of the mirror segments, and it is λ/D in the second case, where D is the diameter of the full primary mirror [3]. (Courtesy of [3], page 334).

If not phased, the image quality or the resolution of a segmented telescope is equivalent to that of a single segment. When phased, the resolution is better by a factor of $\sqrt{N}$ where N is the number of segments [13].

A segment has a total of six degrees of freedom: translation along the axis perpendicular to the segment (piston), rotation about two axes horizontal to the segment (tip and tilt), and translations and rotation in the plane of the segment. The strongest wavefront discontinuities are generated by the piston and tip-tilt movements of the segments.

Other parameters which also affect the image quality of a segmented mirror are the inter-segment gaps, the misfigure of the segment edges, the shape aberrations of individual segments, variations in reflectivity between the segments. All these effects have been studied in the following publications [84, 77, 11, 82, 90].

The effect of segmentation, and in particular the effect of piston errors on the point spread function of a segmented telescope are shown in the following section.

2.1 Point spread function of a segmented telescope

The theory in this section is extracted from the publication by N. Yaitskova et al. [84] on the analytical study of diffraction effects in extremely large segmented telescopes.

The aperture function of a telescope with N segments can be written as

$$F(\mathbf{x}) = \sum_{j=1}^{N} f_j(\mathbf{x}-\mathbf{r}_j) = \sum_{j=1}^{N} \theta_j(\mathbf{x}-\mathbf{r}_j)\exp[i\phi_j(\mathbf{x}-\mathbf{r}_j)], \tag{2.1}$$

where f_j is the aperture function of an individual segment, $\mathbf{x}$ is the position vector in the aperture plane, j corresponds to the segment index, $\mathbf{r}_j$ is the segment center point, and ϕ_j is the phase corresponding to the segment j. θ_j is the transmission function of the segment j, which is unity inside the segment and zero outside.

The point spread function (PSF) $\mathrm{P}(\mathbf{w})$ is, by definition, the modulus of the square of the Fourier transform of Eq. (2.1) and is given by:

$$\mathrm{P}(\mathbf{w}) = \left(\frac{AN}{\lambda z}\right)^2 \left| \frac{1}{N}\sum_{j=1}^{N}\left[\exp\left(i\frac{2\pi}{\lambda z}\mathbf{w}\cdot\mathbf{r}_j\right)\ \frac{1}{A}\int \theta_j(\xi)\exp\left[i\phi_j(\xi)\right]\ \exp\left(i\frac{2\pi}{\lambda z}\mathbf{w}\cdot\xi\right)d^2\xi\right]\right|^2, \tag{2.2}$$

where λ is the wavelength, $\mathbf{w}$ is the position vector in the image plane, z is the focal distance, $\xi = \mathbf{x} - \mathbf{r}_j$ is the local position vector for the segment j and A is the area of an ideal segment.

2.1.1 Perfect telescope

In the particular case of a perfect telescope, with $\phi_j = 0$, $\theta_j = \theta$, Eq. (2.2) takes the form [32, 84]

$$\begin{aligned}\mathrm{P}(\mathbf{w}) &= \left(\frac{AN}{\lambda z}\right)^2 \left|\frac{1}{N}\sum_{j=1}^{N}\exp\left(i\frac{2\pi}{\lambda z}\mathbf{w}\cdot\mathbf{r}_j\right)\right|^2 \times \left|\frac{1}{A}\int\theta(\xi)\exp\left(i\frac{2\pi}{\lambda z}\mathbf{w}\cdot\xi\right)d^2\xi\right|^2 \\ &= (\frac{AN}{\lambda z})^2 \mathrm{F_g}(\mathbf{w})\mathrm{P_s}(\mathbf{w}).\end{aligned} \tag{2.3}$$

The PSF of a perfect telescope is the product of two factors: a grid function $\mathrm{F_g}$ and the PSF of an individual segment, $\mathrm{P_s}$.

The grid function is a periodic function with sharp peaks, since it is the Fourier transform of the segmentation grid. The analytical expression for $\mathrm{P_s}$ is given by:

$$\begin{aligned}\mathrm{P_s} &= |t_1(\mathbf{w})|^2 \\ &= \left|\frac{1}{A}\int \theta(\xi)\exp\left(i\frac{2\pi}{\lambda z}\mathbf{w}\cdot\xi\right)\mathrm{d}^2\xi\right|^2 \\ &= \left|\frac{\sin(\sqrt{3}\alpha-\beta)\mathrm{sinc}(\alpha\sqrt{3}+\beta)+\sin(\sqrt{3}\alpha+\beta)\mathrm{sinc}(\alpha/\sqrt{3}-\beta)}{2\sqrt{3}\alpha}\right|^2 \end{aligned} \tag{2.4}$$

where $\alpha = (\pi d/2\lambda z)w_x$ and $\beta = (\pi d/2\lambda z)w_y$ are normalized coordinates in the image plane. d represents the size of a hexagon defined as the flat-to-flat distance between two opposite edges. The segment point spread function P_s is shown in Figure 2.2.

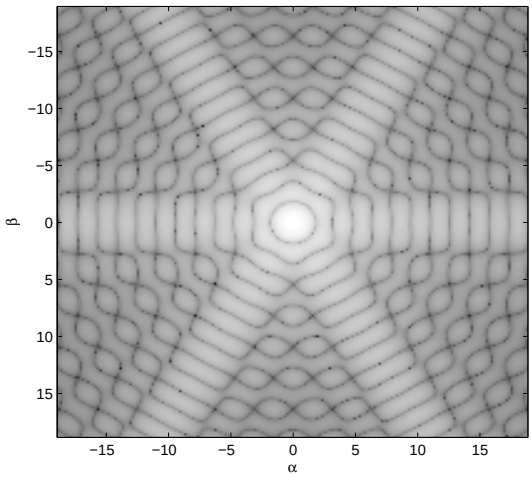

Figure 2.2: The point spread function of a segment $\mathrm{P_s}$ plotted as a function of the normalized coordinates α and β.

2.1.2 Piston errors

If the only errors are random piston errors such that $\phi_j(\xi) = \delta_j$ is the piston error on the segment j, the general expression (2.2) becomes

$$\begin{aligned}\mathrm{P}(\mathbf{w}) &= \left(\frac{AN}{\lambda z}\right)^2\left|\frac{1}{N}\sum_{j=1}^{N}\exp\left(i\frac{2\pi}{\lambda z}\mathbf{w}\cdot\mathbf{r}_j\right)\exp\left(i\delta_j\right)\right|^2 \times \left|\frac{1}{A}\int\theta(\xi)\exp\left(i\frac{2\pi}{\lambda z}\mathbf{w}\cdot\xi\right)d^2\xi\right|^2 \\ &= \left(\frac{AN}{\lambda z}\right)^2\mathrm{F'_g}(\mathbf{w})\mathrm{P_s}(\mathbf{w}). \end{aligned} \tag{2.5}$$

The piston errors modify only the grid function, which is defined for perfectly aligned segments in Eq. (2.3). The modified grid function F'_g introduces an irregular speckle background, which also reduces the Strehl ratio[1].

From Equation (2.5), one can derive an expression for the Strehl ratio. For an unphased segmented telescope with a RMS piston error of δp nm, measured on the wavefront[2], the ensemble-averaged Strehl ratio for a telescope with phase errors distributed over its N segments is given by [11, 85]:

$$S = \frac{1 + \exp(-\sigma^2)(N-1)}{N} \tag{2.6}$$

where $\sigma = k\delta p$ and $k = 2\pi/\lambda$ is the wavenumber.

For large piston errors, this expression converges to $1/N$ and the Strehl ratio is reduced by a factor N. The telescope quality in terms of Strehl is therefore equivalent to that of a single segment. However, for small piston errors with $\sigma \to 0$, the Strehl ratio converges to 1 (Figure 2.3).

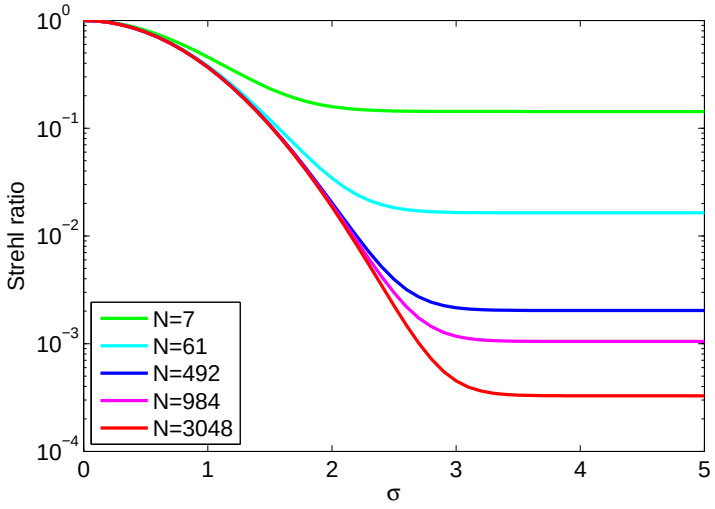

Figure 2.3: Strehl ratio of a segmented system with N segments and in the presence of piston error with σ RMS.

For an E-ELT with 984 segments, reducing the piston error measured on the wavefront from $\delta p = 60$ nm to $\delta p = 20$ nm results in a substantial improvement of Strehl ratio from $S = 0.71$ to $S = 0.96$.

For a perfectly phased telescope, the zeros of the P_s coincide with the peaks of the F_g so that in the resulting PSF a single central peak is observed (Fig. 2.4 a). It is interesting

[1]The ratio between the normalized peak intensity of an aberrated telescope to that of the same telescope working at the diffraction limit.

[2]We suppose that the piston errors are independent and that they obey Gaussian distribution statistics with zero mean.

to note that gaps, tip-tilt errors, and turned-down edges modify only the segment PSF $\mathrm{P_s}$ while leaving the grid function $\mathrm{F_g}$ unchanged. These perturbations therefore lead to the appearance of higher-order peaks in the telescope PSF (Fig. 2.4 b), as described in the next paragraph.

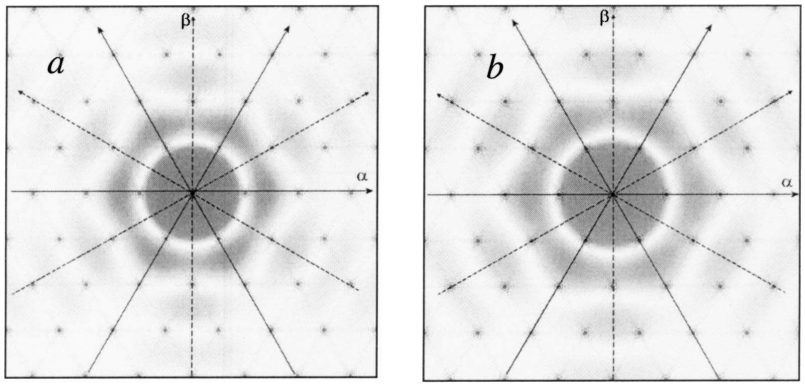

Figure 2.4: a. Grid factor (regular spots) and the segment $\mathrm{P_s}$ for a perfect telescope without gaps. b. The same but with gaps between segments. Courtesy of N. Yaitskova [84].

2.1.3 Arbitrary segment aberration

The phase error on each individual segment can be represented as a set of aberrations, described by a Zernike polynomial.

The term segment aberration refers to a particular aberration of an individual segment and the term segmentation error refers to the shape of the wavefront reflected by the whole segmented mirror.

When the segmentation error is described by the polynomial Z_N with the coefficients a_{jn} randomly distributed over the whole population of segments

$$\phi(\mathbf{x}) = \sum_{j=1}^{N} a_{jn} Z_n(\mathbf{x} - \mathbf{r}_j)\theta(\mathbf{x} - \mathbf{r}_j), \tag{2.7}$$

the ensemble-averaged PSF of a segmented aperture can be written in the canonical form [82, 83]:

$$\mathrm{P}(\mathbf{w}) = \mathrm{F_g}(\mathbf{w})\mathrm{B}(\mathbf{w}) + \frac{\mathrm{D}(\mathbf{w}) - \mathrm{B}(\mathbf{w})}{N}. \tag{2.8}$$

$$\mathrm{B}(\mathbf{w}) = \left| \frac{1}{A} \int < \exp\left[ia_n Z_n(\xi)\right] > \theta(\xi) \exp\left(i\frac{2\pi}{\lambda}\mathbf{w}\cdot\xi\right) \mathrm{d}^2\xi \right|^2, \tag{2.9}$$

$$\mathrm{D}(\mathbf{w}) = \frac{1}{A^2} \int\int < \exp\left\{ia_n[Z_n(\xi) - Z_n(\xi')]\right\} > \times \exp\left(i\frac{2\pi}{\lambda}\mathbf{w}\cdot(\xi - \xi')\right) \theta(\xi)\theta(\xi')\mathrm{d}^2\xi\mathrm{d}^2\xi'. \tag{2.10}$$

The first term of Eq. (2.8) [3] describes the diffraction pattern and its modification, and the second one describes a halo. The halo consists of quasi-static speckles, each having the size of the Airy disk of the telescope. The speckled field covers an area inversely proportional to the size of a segment, i.e., an area much larger than the Airy disk of a segment [83].

If $\sigma_n = \sqrt{a_n^2}$ is the coefficient of a segment aberration in form of the Zernike polynomial Z_n, the halo term in Eq. (2.8) can be expressed as

$$\frac{\mathrm{D}(\mathbf{w}) - \mathrm{B}(\mathbf{w})}{N} \approx \frac{\sigma_n^2}{N} \left| t_n(\mathbf{w}) \right|^2, \tag{2.11}$$

where

$$t_n(\mathbf{w}) = \frac{1}{A} \int Z_n(\xi)\theta(\xi) \exp\left(i \frac{2\pi}{\lambda} \mathbf{w}\xi \right) \mathrm{d}^2\xi. \tag{2.12}$$

The halo is proportional to the variance of the segment aberration coefficient, inversely proportional to the number of segments, and its shape is the square of the modulus of the Fourier transform of the polynomial corresponding to this aberration within a segment's boundary [83].

In the case of pure piston error, $t_1(\mathbf{w})$ is given by Eq. (2.4) and

$$\frac{\mathrm{D}(\mathbf{w}) - \mathrm{B}(\mathbf{w})}{N} \approx \frac{\sigma_1^2}{N} \left| t_1(\mathbf{w}) \right|^2, \tag{2.13}$$

For pure piston error, the halo of the PSF is shown in Figure2.2.

2.1.4 Power spectral density of phase errors

The result presented here will be used in Chapter 9.

The power spectral density (PSD) Φ_{phase} of arbitrary wavefront error, is the square of the modulus of the Fourier transform of the phase error $\varphi(\mathbf{x})$, given by:

$$\Phi_{\text{phase}}(\mathbf{w}) = \left| \frac{1}{AN} \int \varphi(\mathbf{x}) \exp\left(i \frac{2\pi}{\lambda} \mathbf{w} \cdot \mathbf{x} \right) \mathrm{d}^2 x \right|^2. \tag{2.14}$$

If, across individual segments, the phase errors are described by Zernike polynomials and the coefficients of the Zernike modes are randomly distributed over the set of segments with RMS-values σ_n, Φ_{phase} is given by

$$\Phi_{\text{phase}}(\mathbf{w}) = \sum_n \frac{\sigma_n^2}{N} |t_n(\mathbf{w})|^2 \tag{2.15}$$

which coincides with the PSF halo given by Eq. (2.11). The PSF halo is the statistically averaged PSD of the phase error [83].

[3] The segment index is omitted in a_{jn}, assuming that the values of the aberration coefficients a_{jn} for any pair of segments are uncorrelated and assuming that the statistical properties of the aberration coefficient do not change from one segment to another.

2.2 Requirements

The importance of the phasing of segmented mirrors in a telescope has been demonstrated in several papers [84], [85], [77].

We have seen that in a segmented telescope, the image quality is strongly affected by wavefront errors introduced by the segment aberrations including segment misalignments. The PSF halo, and the Strehl ratio, are both strongly affected by the variance of the segment aberration coefficients. The first is proportional to the variance of the segment aberration coefficients and the Strehl ratio decreases rapidly with an increase of the phasing error, as shown in Figure 2.3.

The requirements on the shape of the primary mirror of future ELTs will strongly depend on the science case and on the astronomical instruments used for the observations. For applications such as direct detection of exoplanets with extreme adaptive optics and coronagraphy on an ELT, as is the case of the future instrument EPICS[4] [43], the requirements are more stringent. The PSF halo will particularly affect the contrast. The challenge of high contrast imaging is to directly image an exoplanet, against the bright background of its parent star. In order to reach contrasts of 10^{-8} or 10^{-9}, a precision of the order of 30 nm RMS must be reached [83, 6, 49].

2.3 Active control

As seen in the previous section, the image quality of a segmented telescope will be affected by segment misalignment errors of the primary mirror. In order to achieve an optical quality equivalent to the corresponding monolithic telescope, the segments have to be phased.

If not actively controlled, the segments of the primary mirror will move in a random manner. At high temporal frequencies, they are affected by the wind and by vibrations of the structure. At lower temporal frequencies, gravitational load and thermal variations will also induce misalignments of the segments.

The control of the primary mirrors of the future E-ELT and the TMT will be based on the well proven strategy used at the Keck telescope. The 10-meter primary mirror of the Keck telescope is made of 36 hexagonal segments which measure 180 cm corner to corner. The segments are supported by three 12-point whiffletrees (Figure 2.5). A warping harness, foreseen to correct the lower-order aberrations of the segments, is attached to the whiffletree support. Three mechanical actuators, called position actuators, will move the whiffletree, and consequently the segment, in its three out-of-plane rigid body degrees of freedom: piston and tip-tilt [5].

The primary mirror segments of the E-ELT will be supported by a 27-point whiffle tree [20], shown in Figure 2.6.

During observations, the relative displacements of the segments in real time are measured by edge sensors. Typical edge sensors measure only one direction of the displacement.

[4] EPICS is a near infra-red instrument foreseen for the E-ELT, aimed at the research of exo-planets.

[5] The optical performance is less sensitive to the translation and rotation in the plane of the segment

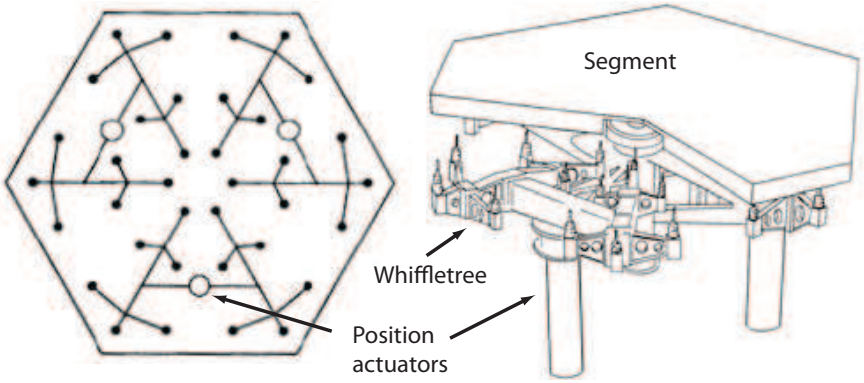

Figure 2.5: Left: The segments are supported by three 12-point whiffle trees. Right: View of one of the whiffletrees and of two position actuators. The foot prints of the three position actuators can also be seen on the left figure, shown as circles. (Courtesy of [3], page 220.)

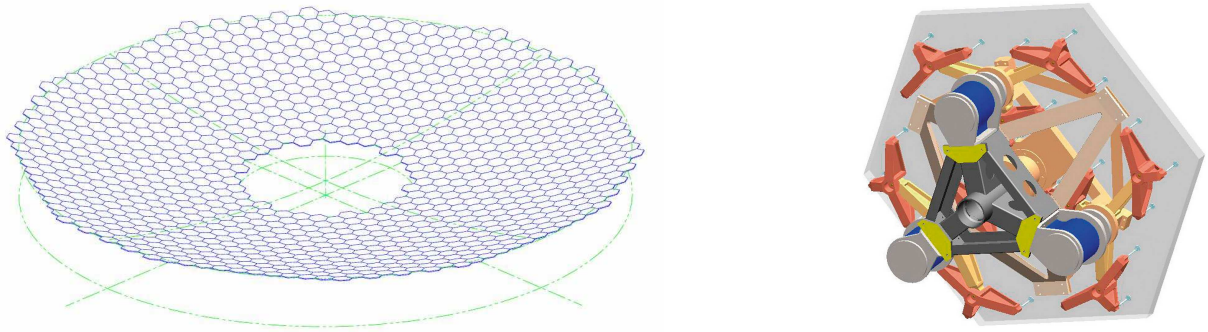

Figure 2.6: Left: Primary mirror of the 42-meter E-ELT with 984 segments. Right: The segment is shown on the 27 point whiffletree; the three blue cylinders are the actuators for piston and tip-tilt control. Courtesy of M. Dimmler [20].)

Therefore, two edge sensors per edge are required to provide the relative piston and the relative tip-tilt between neighboring segments. The typical bandwidth for the control loop between the edge sensors and the position actuators is a few Hertz (2-3 Hz). The accuracy of the edge sensors can reach sub-nm level [20].

Existing segmented telescopes such as Keck, SALT and GTC use capacitance-based edge sensors. The edge sensors on the Keck telescopes are made of low-expansion ceramic glass and have an operating range of $\pm$ 20 μm [3]. However, capacitive edge sensors are sensitive to humidity variations, dust and condensation. As a result, the sensors drift by about 2 nm per day, and therefore require calibrations at regular intervals. Currently, such reference values can only be obtained with a precision of the order of a few nanometers by optical measurements, with a phase sensor, preferably using the light of a star in the field of the telescope.

2.4 Optical phasing

Optical phasing is performed with a phasing sensor which uses the light of a star outside the science field to produce an image, in which the misalignments of the segments can be detected.

There are two scenarios where optical phasing is required:

- during the integration of new segments (or after the exchange of a segment) to provide an initial zero reference value for the edge sensors,
- periodically to re-calibrate the reference values of the edge sensors.

In the first case, the positions of the newly installed segments on the primary mirror will be within a range of 20 μm wavefront with respect to the neighboring segments. It is foreseen to replace two segments per day for re-coating in the future E-ELT and to phase them with the light of bright stars. With a large number of detectable photons, high accuracies can be obtained during this process [60].

For the periodic calibration, there are different possibilities. The first one is to perform the optical phasing at the beginning of the night before the observations, as is done at the Keck telescope [12]. The phasing is undertaken at intervals of about four weeks, using relatively bright guide stars, and takes between half an hour and two hours. For the rest of the time the control of the segment positions relies on the stability of the edge sensors. The alternative solution is to perform optical phasing during the scientific observations. In this case, one has to cope with a small number of photons[6], but has to correct only comparatively small differential segment phase errors [60]. This would result in a second control loop, which would work at a bandwidth of approximately 0.01 Hz.

In the next Chapter (Chapter 3), different concepts of phasing sensors are presented.

[6]This option is valid provided that a sufficiently bright reference star for the phasing camera can be found in the field of view.

Chapter 3

Phasing sensors

The general problem of wavefront sensors is to recover the phase $\varphi(\mathbf{r})$ of a given wavefront although only intensity measurements are available. Let $U(\mathbf{r})$ be the complex amplitude of the wavefront, such that $U(\mathbf{r}) = |u(\mathbf{r})| \exp(i\varphi(\mathbf{r}))$ where $\mathbf{r}$ is a two dimensional spatial coordinate.

The light is taken to be monochromatic, with wavelength λ. In the case of pure piston errors, the general problem of phasing becomes one-dimensional. With a local coordinate

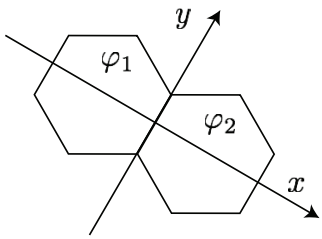

Figure 3.1: Cartesian coordinate system at the boundary between two segments and the phases φ_1 and φ_2 due to piston in each segment.

system centered at the border between two segments (the x-axis being perpendicular to the edge as shown in Figure 3.1), and with φ_1 and φ_2 being the piston phase values of two segments with piston values p_1 and p_2, the phase $\varphi(\mathbf{r})$ can be expressed as:

$$\varphi(\mathbf{r}) = \varphi(x) = \begin{cases} \varphi_1 = (2\pi/\lambda)\ p_1 & \text{if } x < 0 \\ \varphi_2 = (2\pi/\lambda)\ p_2 & \text{if } x > 0 \end{cases} \tag{3.1}$$

and the complex amplitude as $U(\mathbf{r}) = U(x) = |u(x)| \exp(i\varphi(x))$. We define $\Delta\varphi$ as:

$$\Delta\varphi = \varphi_2 - \varphi_1 = \frac{2\pi}{\lambda}\Delta p \tag{3.2}$$

where $\Delta p = p_2 - p_1$ is the differential piston generated by the phase jump $\Delta\varphi$.

With the development of large segmented telescopes, the phasing of segmented apertures is a major concern and many different phasing technologies have been proposed. In this section a review of different phase sensors will be presented.

Depending on the technique used, the recovery of the phase can be done directly in the image plane, in a pupil plane or in intermediate planes.

Image plane techniques include phase retrieval [33, 28], where the phase is directly determined from a focal plane image. The solution is not unique. However, this ambiguity can be resolved with the use of a second image where a phase perturbation, typically a defocus, has been added. This second method is called phase diversity [35, 34, 62]. Both techniques, which are strongly affected by atmospheric effects, are particularly advantageous for space applications since they require little or no additional hardware.

Intermediate plane techniques include curvature sensing, where the wavefront reconstruction is performed with defocused images of the pupil. In classical curvature sensing with a continuous wavefront, the image planes are sufficiently far from the focus to justify approximations of geometrical optics: local differences in the intensities between two de-focused images, taken at the same distance from the focus, are proportional to the local wavefront curvature [68]. However, for the measurement of wavefront discontinuities, diffraction effects have to be taken into account.

Pupil plane techniques include the Shack-Hartmann type wavefront sensor, the Pyramid sensor, the Mach-Zehnder interferometer and the Zernike Phase Contrast Sensor. A major advantage of pupil-plane techniques is that there is a unique and simple relation between the location on the sensor and the location in the pupil.

3.1 Image plane techniques

Different techniques exist which allow phase differences to be detected from one or more in- or out-of-focus images. These techniques have the advantage of requiring little or no dedicated hardware; imaging cameras, which already exist on the telescope, are used.

3.1.1 Phase retrieval

Estimating the aberrations from a single focal-plane image of a point source is a difficult problem known as phase retrieval [33]. The image of a given object contains information not only about the object, but also about the wavefront. A focal-plane sensor thus requires usually no additional optics. Phase retrieval is an inverse problem. The wavefront cannot be directly calculated from the PSF since the intensities in the image plane is related in a highly non-linear way to the phases in the pupil plane. Therefore, phase retrieval relies on iterative techniques to recover the phase. An initial estimate is made and iterated until the derived PSFs and the measured PSFs are sufficiently close. In phase retrieval, the most important part is the algorithm used to compute the wavefront [28]. Most algorithms are based on [30].

Phase retrieval has two limitations: it only works with a point source and there is generally a sign ambiguity in the recovered phase, i.e., the solution is not unique.

The phase retrieval technique was very successfully applied to measure the wavefront error in the HST from images taken by the onboard cameras. The information was then

used to design corrective optical systems [29].

3.1.2 Phase diversity

The concept of phase diversity goes back to 1979 [35, 34]. The sign ambiguity in phase retrieval is removed by using a second image, in which a known phase difference has been introduced [34], traditionally a defocus, as illustrated in Figure 3.2. (This second image is then used to constrain the estimate of the wavefront error.) It is possible to estimate the unknown phase even when the object is extended and its shape not known. Phase diversity is optically very easy to implement but requires considerable computing power for real-time corrections, as it is most often based on an iterative algorithm. Phase diversity has been studied for the cophasing of segmented telescopes in [51, 18] and has even been tested at the Keck telescopes but the expectations were not fulfilled [47].

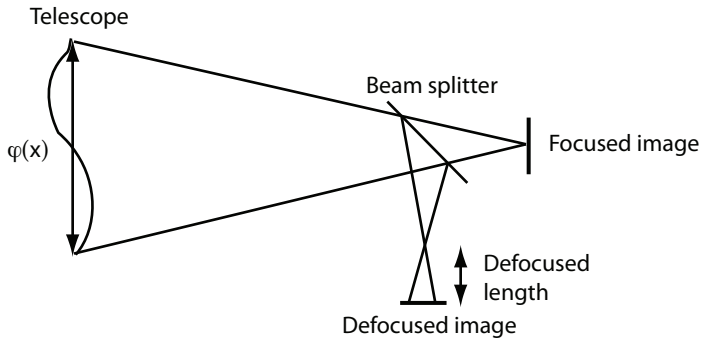

Figure 3.2: Principle of the phase diversity

Phase diversity is very sensitive to the seeing. However, phase diversity has been shown to work well after extreme AO correction [51].

3.2 Intermediate plane techniques

3.2.1 Curvature sensor

The curvature sensor[1] has been proposed and developed by Roddier [68] for atmospheric turbulence measurements in adaptive optics systems.

The principle is presented in Figure 3.3. The light emitted by a celestial object enters the telescope with a focal length f and is focused onto the focal plane. Two detectors are placed in planes at equal distances in front and behind the focal plane. They record the intensity distributions I_i and I_x (intra-focal and extra-focal, respectively). If the incoming wave front is free of aberrations, both detector planes are uniformly illuminated. A local

[1]The term curvature sensing is commonly used for out of focus measurements of piston errors although strictly speaking no curvature is measured.

curvature in the incoming wave front has the effect that the focal plane of the corresponding subaperture no longer coincides with the nominal focal plane, resulting in different intensities I_i and I_x. Therefore, local curvature variations will result in local intensity differences in the two defocused planes (see Figure 3.3). The normalized intensity difference

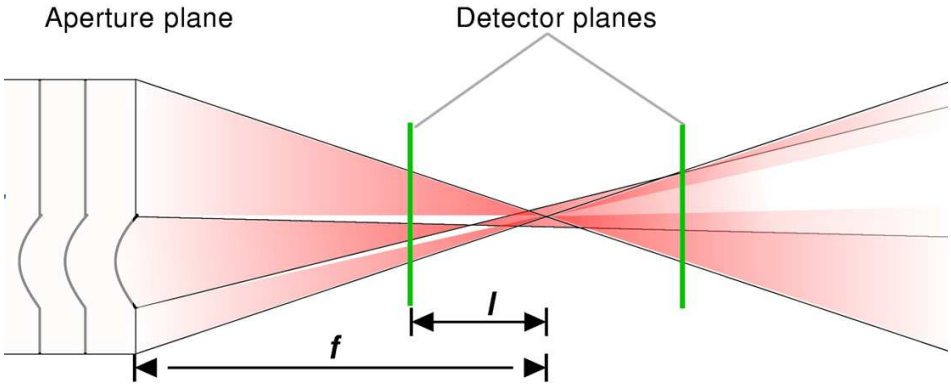

Figure 3.3: Principle of the curvature sensor. Courtesy of A. Schumacher.

$$S(\mathbf{r}) = \frac{I_i(\mathbf{r}) - I_x(-\mathbf{r})}{I_i(\mathbf{r}) + I_x(-\mathbf{r})} \tag{3.3}$$

can therefore be used to retrieve information on wavefront aberrations. However this applies only for a continuous wavefront. The geometrical optics approximation cannot be used in the case of a discontinuous wavefront.

The use of curvature sensing for the measurement of wavefront discontinuities has been first suggested by Rodrigez-Ramos and Fuensalida [70] and has later been studied by Chanan, Troy and Sirko [14] and Cuevas et al. [17]. Schumacher and Devaney [71] have developed a method that allows fast precision measurements of large piston errors even at visible wavelengths.

The analytical expression for the signal due to a single piston step was derived by Rodrigez and Fuensalida [69] using an extension of the classical Fresnel treatment of diffraction at a semi-infinite opaque screen. With the phase step given by Eq. (3.1), the normalized intensity as a function of the coordinate x in a detector plane at a distance z from the pupil plane is given by:

$$\frac{I(x)}{I_0} = 1 + A\sin(\Delta\varphi) + B[1 - \cos(\Delta\varphi)] \tag{3.4}$$

$$A = C(\frac{x}{\rho}) - S(\frac{x}{\rho}), \tag{3.5}$$

$$B = C^2(\frac{x}{\rho}) - S^2(\frac{x}{\rho}) - \frac{1}{2} \tag{3.6}$$

$$\rho = \sqrt{\lambda z/2}, \tag{3.7}$$

where C and S are the Fresnel cosine and sine integrals, respectively, and ρ determines the signal width. The formula is valid for collimated light. In a telescope of focal length f, the effective propagation distance z[2] can be expressed as

$$z = \frac{f(f-l)}{l}, \tag{3.8}$$

where l is the distance from the focal plane (see Figure 3.3) [71].

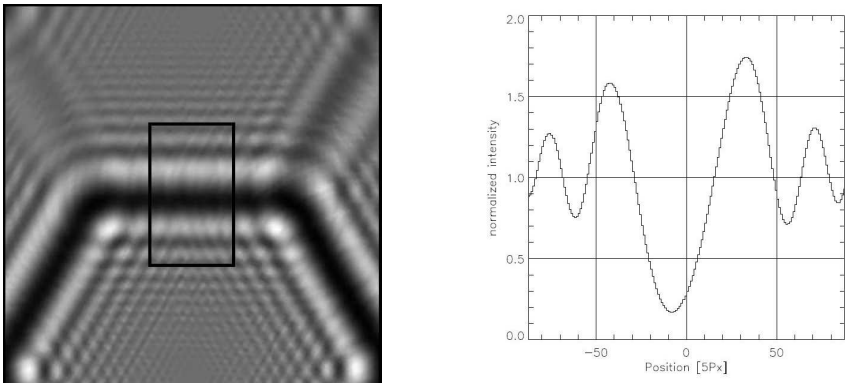

Figure 3.4: Left: Diffraction effect due to a segment step. Right: Projection along an axis perpendicular to the edge gives a one dimensional signal which contains the information on the piston step. Courtesy of A. Schumacher [71].

Figure 3.4 shows the one-dimensional signal which corresponds to equation (3.4) obtained on one defocused image [71]. Schumacher and Devaney [71] show that the piston information can be extracted either from a single image or a pair of defocused images. In the case of a single image (intra or extra focal image), the capture range is doubled compared to the normalized intensity difference.

The width of the signal increases with the propagation distance z. This is illustrated in Figure 3.5, which shows three defocused images simulated with three different propagation distances. An upper limit on the signal width is determined by the signal crosstalk from nearby segment edges and a lower limit by the required signal sampling of the detector. The blur due to seeing shall also be smaller than the width of the signal.

Chanan et al. [7] have developed a method called Phase Discontinuity Sensing (PDS), which has been successfully applied at the Keck telescopes. It is applied at a wavelength of 3.3 μm using an existing infrared instrument. Chanan and Pinto [10] have also further developed a broadband version of phase discontinuity sensing, similar to the broadband technique used with the Shack-Hartmann type phasing sensor [12], in order to extend the capture range from 0.4 μm to 40 μm.

The advantage of curvature sensing is that it requires no special-purpose hardware. It also has the advantage that the spatial sensitivity can be easily adjusted. The greater the

[2]For collimated light, I_1 and I_2 can be considered as defocused pupil images in the conjugate object space. Their distance to the pupil plane is z. According to Newton's formula $(z+f)l = f^2$ [67].

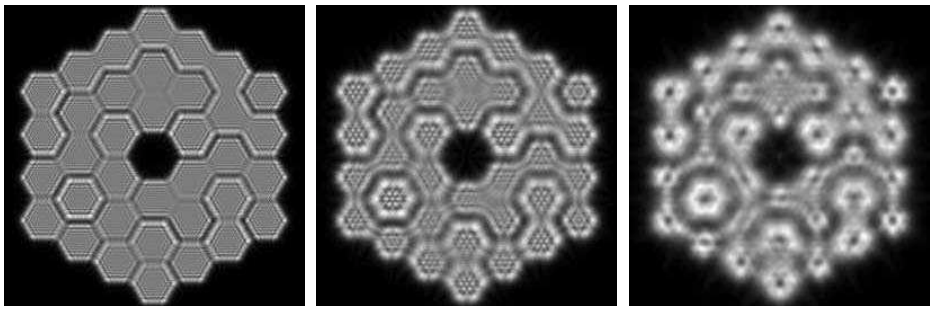

Figure 3.5: Simulated de-focused images of a 36 segment telescope with piston errors. The piston values are uniformly distributed within $\pm\lambda/8$ and the same for each image. $D = 10$ m, $f = 250$ m, $\lambda = 3.3$ μm, $r_0(500\text{nm}) = 0.2$ m. z=(10.2, 31.0, 77.9) km, l = (6; 2; 0.8) m. Courtesy of Achim Schumacher [71].

defocus, the higher is the spatial resolution in the pupil, however, at the price of lower sensitivity to aberrations.

The curvature sensor was part of the Active Phasing Experiment described in Chapter 4 under the acronym DIPSI, the Diffraction Image Phase Sensing Instrument [54].

3.3 Pupil plane techniques

3.3.1 Modified Shack-Hartmann phasing sensor

The Shack-Hartmann method is a technique widely used for active and adaptive optics applications. When applied to the phasing of segmented mirrors, a circular lens is placed across the border between two segments. The information on the phase step is contained in the diffraction pattern of the lens.

This sensor is being used for the phasing of the 36 segments of the Keck telescope, with a prism array and a lens replacing the traditional lenslet array. This prism array is preceded by a mask at the position of the exit pupil. The mask, at a scale of 1/200 of the primary mirror, defines small circular subapertures of 12 cm in diameter projected on the primary mirror and located at the center of each of the 84 intersegment edges shown to scale in the left image of Figure 3.6 [9].

The diffraction pattern as a function of $\Delta\varphi$ at the intersegment border is shown in the right plot of Figure 3.6. For $\Delta\varphi = 0$ we obtain the Airy disk and for $\Delta\varphi = \pi/2$ we obtain a diffraction pattern with two peaks. The algorithm used to reconstruct the wavefront is the following. The 11 theoretical diffraction patterns shown in Figure 3.6 are used as templates in the reconstruction algorithm. The diffraction pattern of the measured edge is cross-correlated pixel by pixel against all 11 templates. $\Delta\varphi$ is estimated from the template that maximizes the correlation coefficients. This method is known as the narrowband phasing algorithm [9].

The other algorithm used at the Keck telescope for measuring the piston error is called

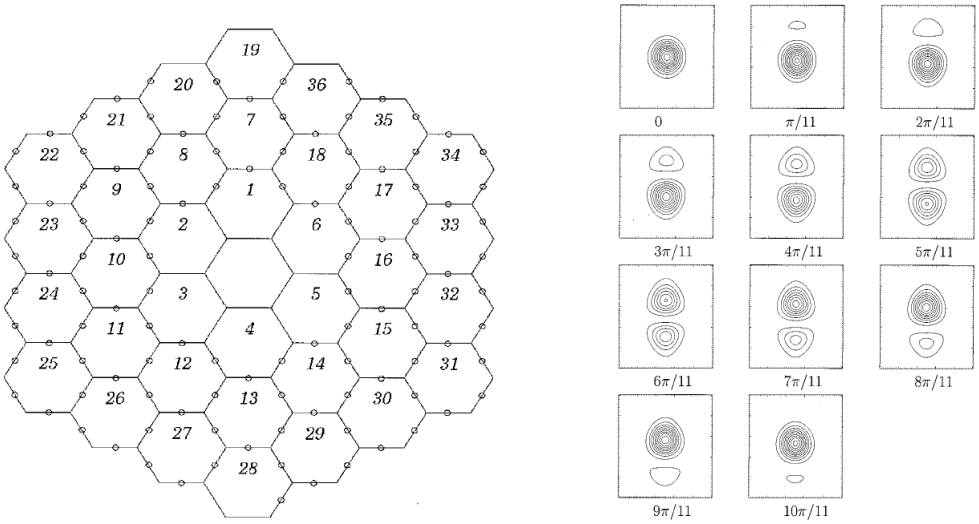

Figure 3.6: Left: Geometry of the primary mirror of the Keck telescopes, showing the 78 circular subapertures that sample the intersegment edges in the phasing procedure. Each segment is 0.9 m on a side. The subapertures are 12 cm in diameter. Right: Theoretical diffraction patterns (monochromatic light) for a split circular subaperture of radius a with a physical step δ between the two halves given by $\Delta\varphi = 0, \pi/11, 2\pi/11, \ldots, 10\pi/11$. Courtesy of G. Chanan [9].

the broadband phasing algorithm [12]. It is based on the coherence length of a broadband filter. The light has a finite bandwidth $\Delta\lambda$. The coherence length l_c of a filter, centered on the wavelength λ, of finite bandwidth $\Delta\lambda$, is given by $l_c = \lambda^2/\Delta\lambda$.

In the framework of the Active Phasing Experiment (APE), described in Section 4, the Shack-Hartmann phasing sensor (SHAPS) [50, 39] has been tested with an array of cylindrical lenslets for the piston measurement and traditional circular lenslets for the tip-tilt and segment shape measurements. With cylindrical lenslets, one can measure the piston signal continually along the border between two segments.

If the length of the lenslet is much larger than its width, the signal can be treated as one-dimensional. If the lenslet is perfectly centered across the border, its normalized intensity distribution can be expressed by

$$p(\xi, \Delta\varphi) = \frac{[\sin(\frac{\pi\xi}{\xi_0} + \Delta\varphi) - \sin(\Delta\varphi)]^2}{(\frac{\pi\xi}{\xi_0})^2}, \tag{3.9}$$

where ξ is the spatial dimension and $\xi_0 = \lambda/a$ is a normalization factor and $a = 150$ μm is the width of the lenslet. The position of the first zero of the diffraction pattern is located at $\xi = \xi_0$.

Results obtained with SHAPS in the framework of the Active Phasing Experiment are presented in [39].

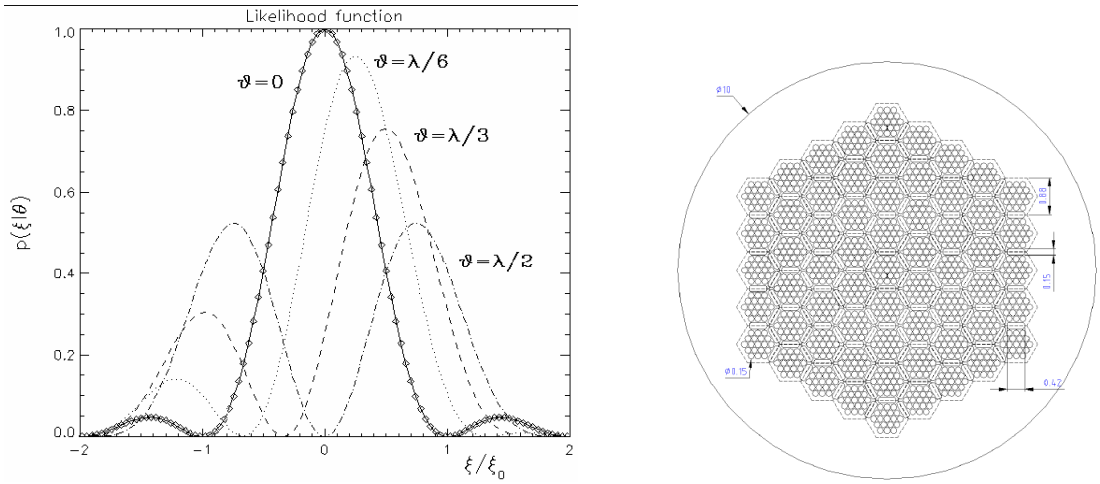

Figure 3.7: Left: Likelihood functions for four differential segment phases θ as a function of the normalized angular coordinate in the focal plane of the Shack-Hartmann lens [60]. Right: Lenslet array used for SHAPS. The cylindrical lenslets are used for the piston measurements, the circular lenslets are used for the tip-tilt and segment shape measurements. Courtesy of R. Mazzoleni [50].

3.3.2 Pyramid sensor

The Pyramid sensor, introduced by Ragazzoni [66] for adaptive optics, is based on the principle of the knife edge test, in the geometrical optics regime. A knife edge, or a sharp blade, is placed in the focal plane close to the focus to block a certain fraction of the rays. In the re-imaged pupil those subapertures corresponding to rays that have been blocked appear dark, whereas those corresponding to rays that could pass appear bright. In this configuration the knife-edge test will give only a bi-valued information on the slopes. By moving the edge up and down, the fraction of the time when the ray passes through the unobstructed half plane and therefore the intensity of the corresponding pixel on the detector in a re-imaged pupil plane depends smoothly on the position where the ray intersects the focal plane and therefore on the slope of the ray in the pupil plane. Figure errors appear on the detector as areas of variable intensity. A uniform movement of the edge therefore linearizes the information on the slopes. The sensor can supply two-dimensional information if the knife edge is replaced by a pyramid and the up and down movement by a circular movement around the focus, as shown in Figure 3.8 [63].

As in the case of the Shack-Hartmann and the curvature sensors, the signal generated by phase discontinuities cannot be derived with geometrical optics approximations. Calculation based on diffraction optics show that for monochromatic light, the amplitude of the signal is a sinusoidal function of the piston step.

The sensor has the capability to measure phase steps between the segments as well as wavefront aberrations inside the segment subapertures simultaneously. The use of the pyramid sensor for co-phasing has been proposed by S. Esposito and N. Devaney [26].

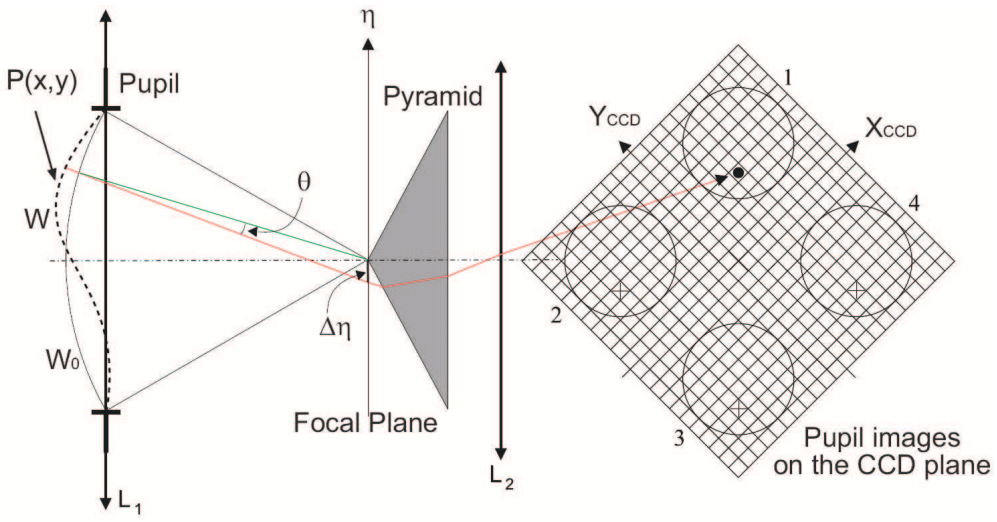

Figure 3.8: Principle of the Pyramid sensor. Courtesy of E. Pinna [63].

3.3.3 The Mach-Zehnder Interferometer

The use of the Mach-Zehnder interferometer for phase step measurements has been proposed by K. Dohlen and studied theoretically by N. Yaitskova [86, 88, 81].

In the classical Mach-Zehnder interferometer, the beam is collimated in the two arms of the interferometer. Angel [2] proposed to place, at an intermediate focus in one of the two arms of the interferometer, a pinhole, which spatially filters the incoming wavefront to use the light from this arm as a reference (Figure. 3.9). The diameter of the pinhole is smaller than the Airy disk, producing a perfectly spherical reference beam. For the phasing of segmented mirrors, the diameter of the pinhole is approximately equal to that of the seeing disk [22].

When the wavefront corresponding to this filtered signal is recombined with the original wavefront from the other arm, two complementary interferograms are produced.

The lower spatial frequency components of the wavefront are near the center of the PSF whereas the higher spatial frequency components are in the wings of the PSF. In the reference arm, the spatial filter removes the high frequency components of the wavefront and transmits the lower spatial frequency ones. When the pinhole diameter a is equal to the full width at half maximum (FWHM) θ_{seeing} of the seeing disk, that is $a \approx \theta_{\text{seeing}}$, most of the aberrations generated by atmospheric turbulence are therefore removed after interference between the two optical beams, leaving only the high spatial frequency components in the output interferograms. With a constant optical path difference (OPD) between the arms equal to $\lambda/4$, the sign of the piston step can be easily deduced on the output interferograms.

The studied pinholes have either an apodized edge with a Gaussian profile or can be represented by the top-hat function. In the case of a round pinhole, the signal is strongly affected by diffraction at the edges of the pinhole.

The mathematical expression for the signal, in the case of pure piston error, is now

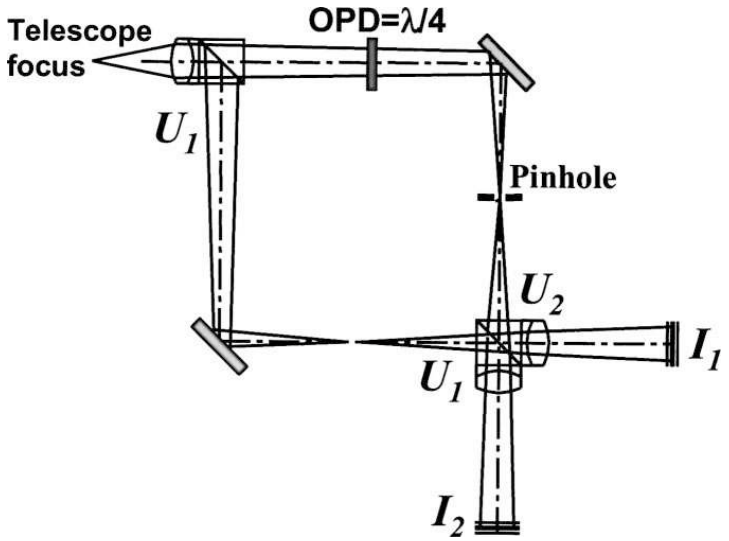

Figure 3.9: Set up of the Mach-Zehnder interferometer. Courtesy of [86].

derived as the phasing sensor which is the main subject of the current thesis, the Zernike Phase Contrast Sensor, is very similar to the Mach-Zehnder interferometer.

In the Fraunhofer diffraction approximation, $U_1(\mathbf{r})$ and $U_2(\mathbf{r})$ denote the complex amplitudes in the pupil planes of the unfiltered and filtered arms of the interferometer, respectively.

The complex amplitude $u_1(\mathbf{w})$ in the focal plane of the unfiltered arm is the Fourier transform of $U_1(\mathbf{r})$.

$$u_1(\mathbf{w}) = \frac{1}{\lambda}\int U_1(\mathbf{r})\exp(-i\frac{2\pi}{\lambda}(\mathbf{r}\cdot\mathbf{w}))d\mathbf{w}^2 \tag{3.10}$$

The complex amplitude $u_2(\mathbf{w})$ is therefore the product of the complex amplitude $u_1(\mathbf{w})$ and the filter $t(\mathbf{w})$:

$$u_2(\mathbf{w}) = u_1(\mathbf{w})\cdot t(\mathbf{w}). \tag{3.11}$$

$t(\mathbf{w})$ is the function defining the pinhole and $T(\mathbf{r})$ its Fourier transform. The **round pinhole** is defined by the top hat function:

$$t(\mathbf{w}) = \begin{cases} 1 & \text{if } |\mathbf{w}| < a/2 \\ 0 & \text{if } |\mathbf{w}| > a/2 \end{cases}$$

and its Fourier transform is given by:

$$T(\mathbf{r}) = \frac{\pi a^2}{4}\frac{2J_1(\pi a\mathbf{r}/\lambda)}{\pi a\mathbf{r}/\lambda} = \frac{b^2\lambda^2}{4\pi}\frac{2J_1(b\mathbf{r})}{b\mathbf{r}}, \tag{3.12}$$

where J_1 represents the Bessel function of the first kind. The **Gaussian pinhole** is represented by the function:

$$t(\mathbf{w}) = \exp\left(-\left[\frac{\mathbf{w}}{a(2\sqrt{\ln 2})^{-1}}\right]\right)^2, \tag{3.13}$$

where a is the full width at half maximum of the Gaussian function. Its Fourier transform is also a Gaussian:

$$T(\mathbf{r}) = \pi \left[\frac{a}{2\sqrt{\ln 2}}\right]^2 \exp\left[-\left(\frac{\pi a}{\lambda(2\sqrt{\ln 2})}\mathbf{r}\right)^2\right] = \frac{b^2\lambda^2}{\pi}\exp(-b^2\mathbf{r}^2). \tag{3.14}$$

The parameter b is related to the pinhole diameter a by

$$b = \pi a/\lambda \quad \text{(round pinhole)} \tag{3.15}$$

$$b = (2\sqrt{\ln 2})^{-1}\pi a/\lambda \quad \text{(Gaussian pinhole)} \tag{3.16}$$

Therefore, the complex amplitude in the pupil plane for the second arm is the convolution of $U_1(\mathbf{r})$ and $T(\mathbf{r})$

$$U_2(\mathbf{r}) = \frac{1}{\lambda^2}\int U_1(\boldsymbol{\xi})T(\mathbf{r}-\boldsymbol{\xi})d\boldsymbol{\xi}^2 \tag{3.17}$$

The interference of the two beams is now calculated under the assumption that the beam splitters are perfect [3]. I_1 and I_2 denote the intensities at the two outputs of the interferogram, respectively:

$$I_1(\mathbf{r}) = 0.5[|U_1(\mathbf{r})|^2 + |U_2(\mathbf{r})|^2 + 2\mathrm{Re}(U_1^*(\mathbf{r})U_2(\mathbf{r})\exp(i\psi_0))], \tag{3.18}$$

$$I_2(\mathbf{r}) = 0.5[|U_1(\mathbf{r})|^2 + |U_2(\mathbf{r})|^2 - 2\mathrm{Re}(U_1^*(\mathbf{r})U_2(\mathbf{r})\exp(i\psi_0))], \tag{3.19}$$

where $\psi_0 = \frac{2\pi}{\lambda}\delta_0$ is a phase offset in one arm of the interferometer, with δ_0 representing the Optical Path Difference (OPD).

The difference between the two interferograms, to which we refer as the signal $S(\mathbf{r})$, contains the information about the phase of the wavefront, or in our case, the wavefront discontinuities generated by the segment misalignments [86].

$$S(\mathbf{r}) = I_1(\mathbf{r}) - I_2(\mathbf{r}) = 2\mathrm{Re}(U_1^*(\mathbf{r})U_2(\mathbf{r})\exp(i\psi_0)) \tag{3.20}$$

In the case of pure piston errors, the phase of the wavefront is given by Eq. (3.1) and the complex amplitude $U_1(\mathbf{r}) = U_1(x) = A\exp(i\varphi(x))$. The filtered wave is also given by $U_2(\mathbf{r}) = U_2(x)$.

Introducing equations (3.12), (3.14) and the expression for $U_1(x)$ into equation (3.17), one obtains the expression for the intensity of the diffracted wave:

$$|U_2(x)|^2 = 0.5\{2 - [1 - \cos(\Delta\varphi)][1 - f^2(b|x|)]\} \tag{3.21}$$

and using equation (3.20) an expression for the signal $S(x)$:

$$S(x) = \{\sin(\Delta\varphi)\mathrm{sign}(x)[1 - f(b|x|)]\}\ \sin(\psi_0) - \{2 - [1 - \cos(\Delta\varphi)][1 - f(b|x|)]\}\ \cos(\psi_0), \tag{3.22}$$

[3] No light absorption and equal transmission and reflection coefficients.

The signal is the sum of two terms: the first term is an anti-symmetric function and the second term is a symmetric function. If one sets the OPD to $\delta_0 = \lambda/4$ ($\psi_0 = \pi/2$) one obtains

$$S(x) = \text{sign}(x)\sin(\Delta\varphi)[1 - f(b|x|)] \tag{3.23}$$

where $f(b|x|)$ is the *error function* in the case of a Gaussian pinhole:

$$f(b|x|) = \Phi(b|x|) = \frac{2b}{\sqrt{\pi}}\int_0^{|x|}\exp(-b^2t^2)dt \tag{3.24}$$

and the *normalized sinc integral* in the case of a round pinhole:

$$f(b|x|) = \frac{2}{\pi}\text{Si}(b|x|) = \frac{2}{\pi}\int_0^{b|x|}\frac{\sin(t)}{t}dt. \tag{3.25}$$

The amplitude of the signal is proportional to the sine of the piston step, $\sin(\Delta\varphi)$. Because of the term $\text{sign}(x)$ in equation (3.23), the signal is discontinuous at $x = 0$. Figure 3.10 shows the expected signals for the two pinholes.

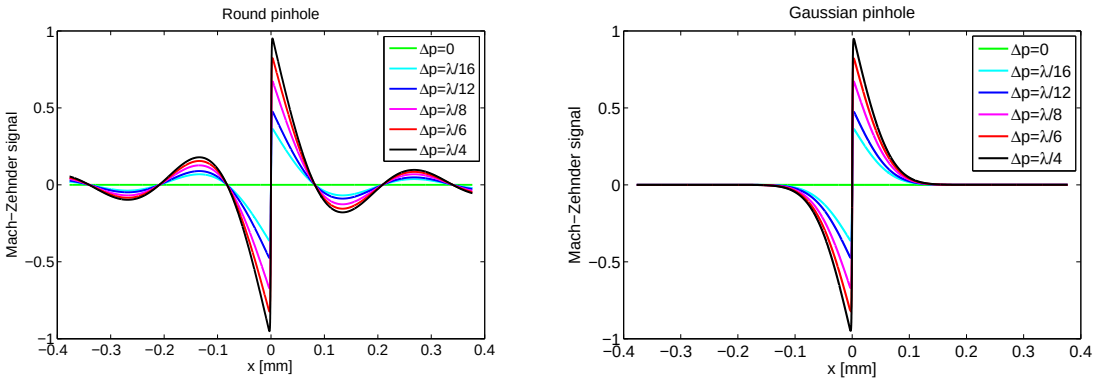

Figure 3.10: Signal profiles for an OPD of $\frac{\pi}{2}$ and for different Δp for the round pinhole and the Gaussian pinhole profiles.

The main advantage of this phasing sensor is that the sign of the piston step can be easily deduced from the shape of the signal. However, the technical difficulty with the Mach-Zehnder interferometer is the need for a precise alignment: the optical path difference between the two arms must be very accurate and shearing effects as well as defocusing must be avoided in the alignment of the two arms. K. Dohlen from LAM has proposed a new concept, called the Zernike Phase Contrast Sensor, which avoids such alignment problems [21]. This sensor is the major topic of this thesis and is treated in Part II.

Chapter 4

Active Phasing Experiment

All the experimental results presented in this thesis were obtained with the Zernike Phase Contrast Sensor (under the acronym ZEUS in APE) in the framework of the Active Phasing Experiment, in which I have been fully involved from the beginning until the end of the experiment.

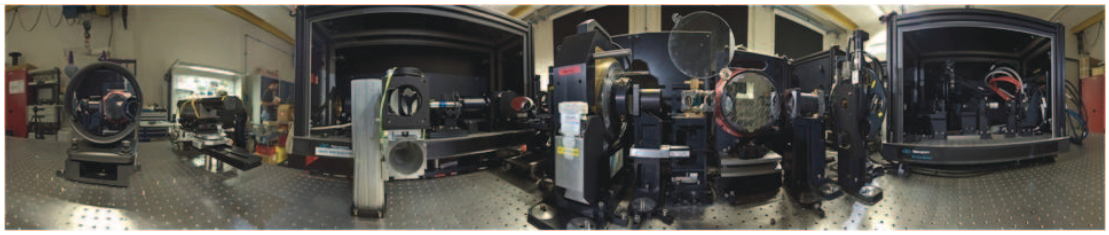

Figure 4.1: Fish eye view of the APE bench and its components.

4.1 Goals and description of the Active Phasing Experiment

The goal of the Active Phasing Experiment [37] has been to demonstrate active wavefront control technologies for a future ELT and to compare four phasing wavefront sensing technologies both in the laboratory (Figure 4.2) and on Melipal, the third Unit Telescope of the ESO Very Large Telescope (VLT) (Figure 4.3)

The phasing camera used at Keck requires a precise alignment of the lenslet array of the Shack-Hartmann detector with respect to the locations of the inter-segment borders in the pupil image. In a rather flexible E-ELT, with potential distortions of the pupil, this accurate alignment is more difficult to achieve than in a more rigid 10 meter telescope.

Phasing sensors, such as the pyramid sensor [65], the curvature sensor [54] and the Zernike Phase Contrast Sensor [21], working directly with pupil images do not suffer from the effects generated by pupil distortions and misalignments.

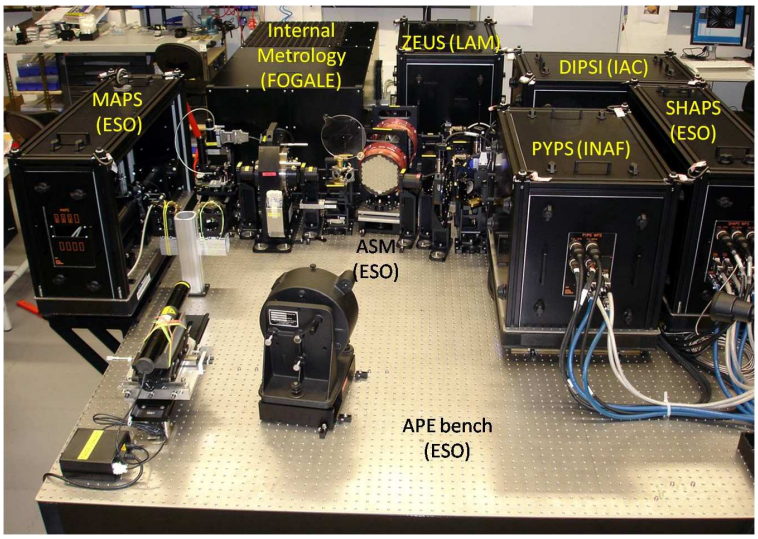

Figure 4.2: The Active Phasing Experiment and all its sub-systems, in the laboratory. From left to right: MAPS, Internal Metrologoy, ASM, ZEUS, PYPS, DIPSI and SHAPS.

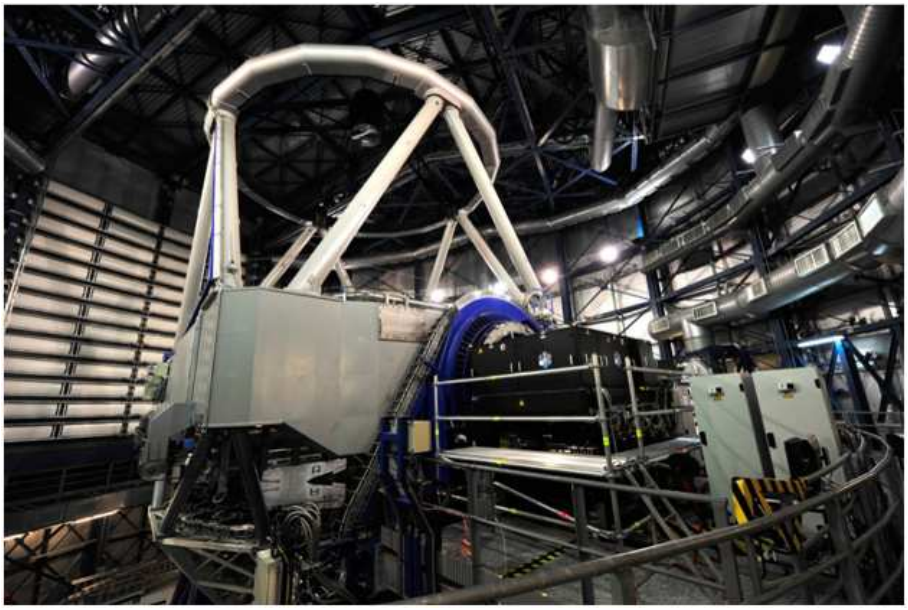

Figure 4.3: The Active Phasing Experiment on the Nasmyth platform of Melipal, the third Unit Telescope of the VLT.

Together with the Shack-Hartmann sensor, these three new phasing camera concepts have been studied in the framework of the *Active Phasing Experiment* (APE) [37].

The principle of these phasing techniques is presented in Chapter 3.

The project started at the end of 2004. It has been carried out by a consortium of three European institutes - Instituto de Astrofisica de Canarias (IAC), Osservatorio Astrofisico

de Arcetri or Instituto Nazionale d'Astrofisica (INAF) and Laboratoire d'Astrophysique de Marseille (LAM) - one industrial company (Fogale Nanotech) and ESO. Four optical phasing sensors have been designed and fabricated, all based on technologies which have been used in active and adaptive optics systems during the last twenty years: a pyramid sensor, called PYPS, developed by INAF, a curvature sensor, called DIPSI for Diffraction Image Phase Sensing Instrument, developed by IAC, and the Zernike Phase Contrast Sensor called ZEUS for Zernike Unit for Segment phasing, developed by LAM and ESO, and finally a Shack-Hartmann phasing sensor, called SHAPS, developed by ESO. The commissioning of the experiment was finished in the laboratory during the spring of 2008 and APE saw first light on sky on the 6th of December 2008. The project ended in June 2009 with its dismounting from the visitor focus on Melipal (UT3). This experiment has been supported by the FP6 research program of the European Union [36].

Figure 4.4: APE team during the First light of the Active Phasing Experiment in December 2008.

It has then been decided to remount the experiment in the laboratory with a new design. An adaptive optics system has been added in the APE optical design in order to study the interaction of phasing and adaptive optics. The new experiment, called Phasing ELT with Adaptive Optics Experiment (PEACE) saw first light in the laboratory with the Adaptive Optics in August 2010.

4.2 APE Sub-systems

This section describes the main subsystems of APE: the Active Segmented Mirror (ASM), the internal metrology (IM), the turbulence generator MAPS, and gives an overview of the four phasing wavefront sensors used in the experiment.

4.2.1 Active Segmented Mirror

A segmentation is created by a scaled-down segmented mirror, called the Active Segmented Mirror (ASM) [38]. At the telescope, the ASM is conjugated to the primary mirror of the VLT to emulate a segmented telescope, as shown in Figure 4.5.

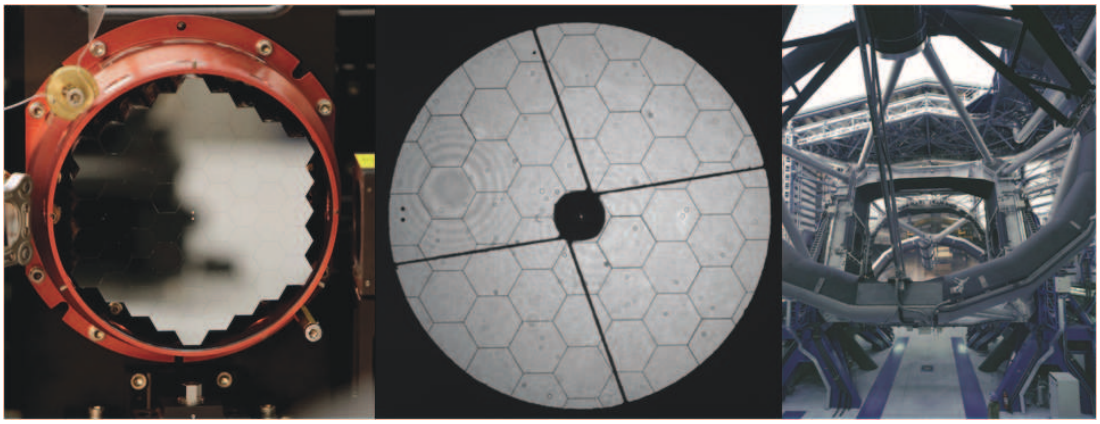

Figure 4.5: Left: ASM on its mount. Middle: Image of the primary mirror of the VLT seen by APE. Right: Melipal

The ASM is a flat segmented mirror composed of 61 hexagonal segments, which can be moved in piston, tip and tilt by three piezo-actuators. The segments are made of Zerodur and are coated with protected aluminum.

Each segment of the ASM has an inner diameter of 17 mm and an optical quality of 15 nm wavefront RMS. The gaps between the segments all lie in the range 70-130 μm. Projected onto the 8.2 meter primary mirror of the VLT, the 61 individual segments appear to have an inner diameter of 1.05 m with gaps of the order of 4 to 8 mm between them. These values are comparable to the ones of future extremely large telescopes, which may have segments with inner diameters of approximately 1.2 meter and gaps of about 4 mm.

Each actuator has a stroke of 30 μm of which 15 μm are dedicated to the alignment and 15 μm dedicated to the experiment. The resolution of the actuators is 0.5 nm. The surface quality of the hexagonal mirrors is better than 15 nm RMS and the edges are sharp (no chamfer and coating without jig-lip). The ASM is shown in Figure A.1.

The segments are controlled in piston, tip and tilt by an Internal Metrology (IM) system.

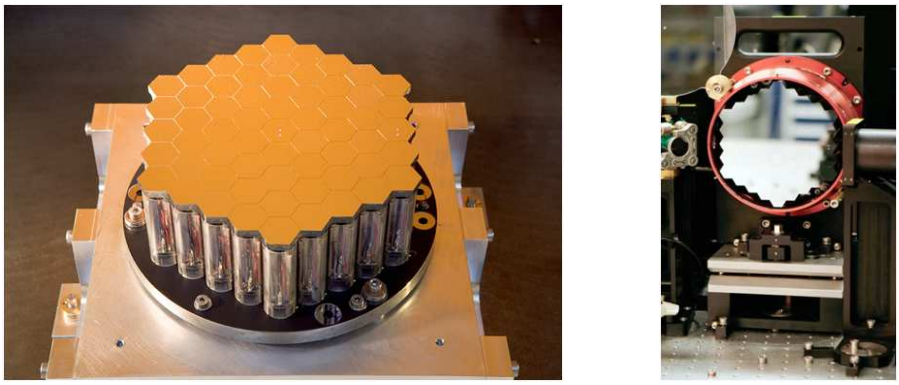

Figure 4.6: Left: ASM on its mount. Right: ASM on the bench.

4.2.2 Internal Metrology

The Internal Metrology (IM) has been developed by Fogale Nanotech [80]. It is a dual wavelength (835 and 860 nm) low-coherence instantaneous phase-shifting interferometer with two optical arms having lengths of 2.5 meter each. The first arm, located inside the IM unit serves as the reference. The second arm is represented in Figure 4.7 as the green beam. The optical beam of the second arm hits the ASM after a reflexion on the off-axis parabola.

The IM measures the position of each segment of the ASM with respect to the central segment at a frequency of 8 Hz with a precision better than 0.3 nm. Like any other interferometer the system is sensitive to environmental disturbances such as vibrations of the bench and air turbulence due to temperature inhomogeneities or wind, all creating noise in the measurement and consequently a loss of resolution in the control loop between the ASM and the IM. In the laboratory the APE bench was placed on a pneumatic support to filter the vibrations coming from the ground. The IM resolution obtained for the positioning of the segments relative to the central one was better than 0.4 nm RMS in the laboratory and better than 5 nm wavefront RMS during night observations at the VLT (90% of the time better than 3 nm RMS). For piston aberrations, the measurement range of the IM is $\pm$ 7.2 μm. With the help of the IM, the system can be brought into any desired aligned or misaligned state within this range.

The internal metrology has different functions in APE [87].

- It supplies independent very high accuracy measurements of the positions of the ASM segments. It is therefore used for the verification of the phasing sensor measurements (with a very high accuracy).

- It stabilizes the relative segment positions during the acquisition of images by the Phasing Wavefront Sensors.

- It plays a role that is similar to the edge sensors in a future ELT.

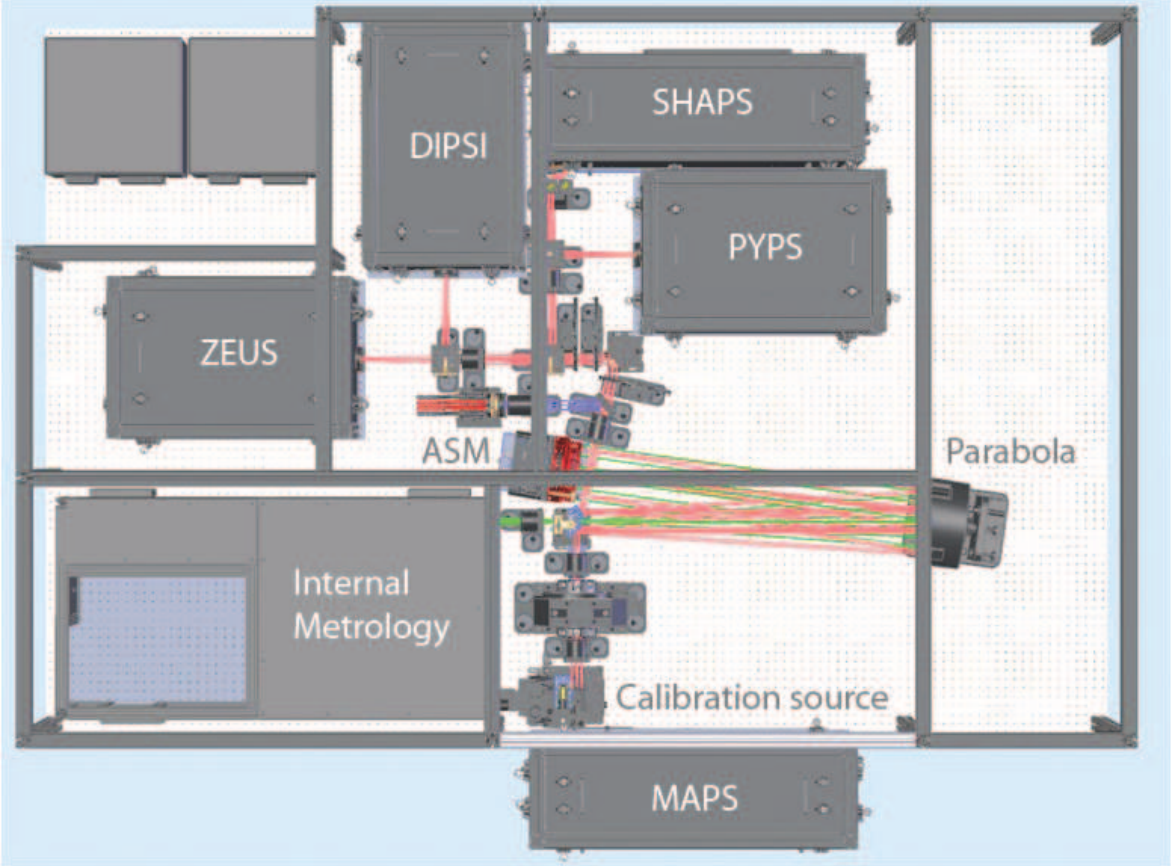

Figure 4.7: Top view of the APE opto-mechanical bench. From bottom to top: MAPS, Calibration Source, Parabola, ASM, ZEUS, DIPSI, SHAPS and PYPS. The green optical beam is the second 2.5 meter arm for the IM measurements, the path is the following: IM - Parabola - ASM - Parabola - IM. The red optical beam starts in MAPS or in the calibration source and feeds the four PWFS. Courtesy of F. Gonté [40].

4.2.3 MAPS

For testing the influence of atmospheric disturbances on the phasing measurements in the laboratory, the APE system is equipped with a turbulence generator called MAPS (Multi Atmospheric Phase screens and Stars) [44], which can be placed at the entrance focus of APE.

The wavefront errors introduced by MAPS are similar to the ones generated by the atmosphere during median seeing conditons. The effects of the atmosphere are reproduced by three transmissive phase screens conjugated to heights of 0, 6 and 8.5 km. The phase screens have different power according to the expected vertical distribution of the turbulence intensities and can rotate at different speeds, to simulate different atmospheric correlation times, which are related to different wind speeds at different altitudes [48].

4.2.4 Phasing wavefront sensors

The following four phasing wavefront sensors were tested on APE.

DIPSI This sensor has been developed by IAC [54]. The concept is based on the principle of curvature sensing as described in Section 3.2.1

PYPS This sensor has been developed by INAF-Arcetri [65]. It is a pyramid sensor as described in Section 3.3.2.

SHAPS This sensor has been developed by ESO [50]. As described in Section 3.3.1, the prism array used for the phasing of the Keck telescope has been replaced by an array of cylindrical lenslets covering subapertures across segment borders. In addition, circular lenslets covering subapertures inside the segments are able to measure the tip and tilt of the segments as well as the segment shapes. Results obtained with SHAPS on sky are presented by Gonté et al. [39].

ZEUS This sensor has been developed by LAM [22], IAC and ESO. It is based on the Zernike Phase Contrast Sensor as mentioned in Section 3.3.3. This sensor is the main topic of the research presented in the Part II of this thesis. Results obtained with ZEUS on sky are presented by Surdej et al. [75].

4.3 Optical path

There are two different optical paths on the APE bench: the first optical path is used for the IM measurements and the second one is used for the four phasing wavefront sensors.

The path for the Internal Metrology is shown in green in Figure 4.7. The beam from the IM enters a beam expander composed of a doublet and of the parabola. The pupil of the IM is then imaged on the ASM and is then sent back to the IM via the parabola and the doublet [40].

The phasing wavefront sensor path is shown in red in Figure 4.7 and is better visible in Figure 4.8. An optical beam having a focal ratio of F/15 and a field of view of 45 arcsecond, coming from the telescope or from MAPS or from the calibration source (as shown in Figure 4.7), passes trough a first group of lenses (LG1) which collimates the diverging beam. A second group of lenses (LG2) refocuses the beam to a shorter focal ratio (F/8). A folding mirror (FM1) directs the beam to an off-axis parabola, which images the pupil of the telescope on the ASM. The beam is then refocused by the off-axis parabola and hits a second folding mirror (FM2). Three wheels containing neutral density filters (NDFW) and color filters (CFW) are positioned on the bench. The optical beam is then split into four identical beams which are refocused at the entrances of each phasing wavefront sensor. Each sensor receives a F/15 beam. The range of the wavelengths used in APE is between 500 nm and 900 nm.

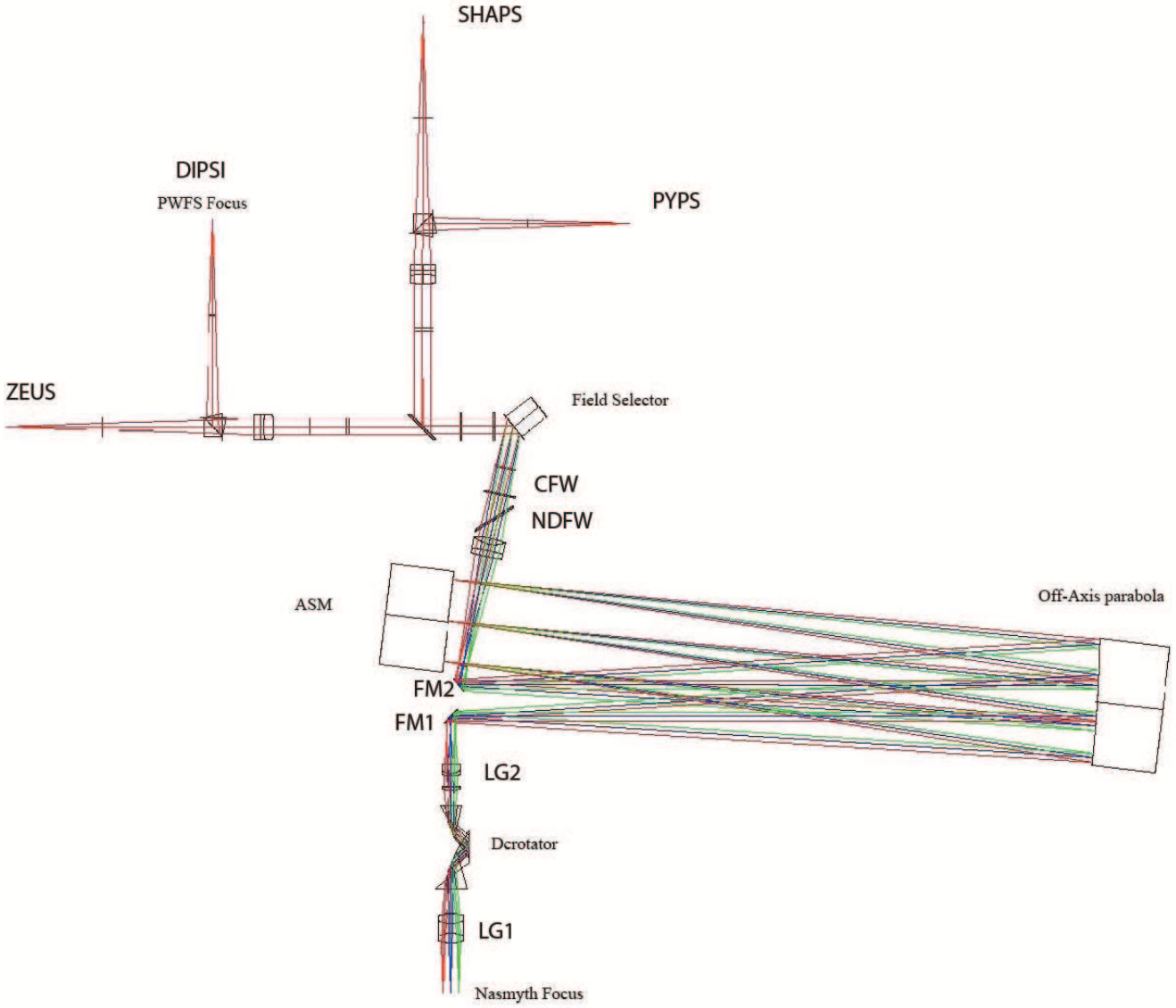

Figure 4.8: APE optical path

4.4 Main questions to be answered with APE

The major topics which should be investigated by APE are based on the facts presented in Section 2.4.

The performance of the phasing wavefront sensors can be described in terms of final accuracy, capture range and limiting star magnitude [87]:

- The final accuracy is the standard deviation of the residual segmentation error, measured by the Internal Metrology.

- If phase sensors use monochromatic light of wavelengths λ, they are insensitive to

phase errors that are multiples of this wavelength. The capture range of the phase sensor is then $\pm\lambda/4$ or $\pm\lambda/2$, depending on the technique used. To resolve these ambiguities and to increase the capture range to several wavelengths, that is typically up to a few microns, different techniques are available. One is based on the use of several wavelengths, and the other one based on the use of a broadband filter of spectral bandwidth $\Delta\lambda$ with a finite coherence length $l_c = \lambda^2/|\Delta\lambda|$. These techniques are explained in Chapter 6.5.

- In the context of this thesis, the limiting star magnitude is defined as the faintest star magnitude with which the phasing sensor is capable of driving the segmented mirror in closed loop to a final accuracy smaller than 30 nm RMS [83]. A phasing sensor, that is capable of phasing a segmented mirror with a small number of photons, typically using the light of stars of magnitude 16, would allow optical phasing measurements to be performed during science operations and therefore to deliver continuous closed loop updates of the reference values of the edge sensors [36].

4.5 Technical description of the ZEUS sensor

The Zernike Phase Contrast Sensor, or the ZEUS sensor, is the main subject of the present Ph.D. thesis. This section gives a technical description of the ZEUS sensor, with which all the results presented in the Chapters 7 and 8 have been obtained.

In the entrance focal plane of the sensor at F/15, different phase masks can be positioned by a translation stage, which can move in the x and y directions [22]. A doublet lens re-images the Active Segmented Mirror onto the CCD detector. The size of the pupil image on the CCD is 6.2 mm which corresponds to 475 pixels of 13 microns [45]. The intensity of the light and the color of the light can be changed by means of a neutral density filter wheel and an optical filter wheel located after the translation stage of the phase mask. The optical filter which has been used for most of the tests is centered on the 650 nm wavelength with a bandwidth of 100 nm. The optical path difference of 175 nm corresponds to a phase shift of $\psi_0 = \lambda/3.7$ for this filter, which is close to the optimum of $\lambda/4$ (see Chapter 5).

The CCD is a 512×512 16 bit E2V chip (CCD 57-10). The noise of the CCD was around 12 counts RMS/sec on sky and 7 counts RMS/sec in the laboratory. The poor quality of the CCD has limited the performance of the Zernike phasing sensor when the tests were performed with long exposure times to average out the turbulence and with a small number of counts.

The Zernike phasing sensor can also be used as a pupil camera when the phase mask is translated such that the beam is not affected by the phase mask.

The following phase masks are available on the ZEUS translation stage.

OPD [nm]	100	100	175	175	175
Phase mask diameter a ["]	1.5	2	1.5	2	1

The choice on the phase mask depends on the seeing and the color of the light. Only the last 3 phase masks with an OPD of 175 nm and mask diameters of 1", 1.5" and 2" to cover seeing conditions ranging from 0.3" to 2" have been used for most of the tests in the laboratory and on sky. These masks have been used since they produce the signals with the maximum signal to noise ratio. The first 2 phase masks would have been useful for shorter wavelengths.

The following optical filters are available in ZEUS:

λ	650	750	880	630	650	550	800	700
$\Delta\lambda$	40	40	20	300	200	20	40	400

Due to the poor optical quality of the ZEUS optical filters, the filters in the APE color filter wheel have been used for most of the tests.

When the filter with the central wavelength $\lambda = 700$ nm and $\Delta\lambda = 400$ nm is in position in the ZEUS color filter wheel, ZEUS can use the following filters available in the APE color filter wheel:

λ	650	650	900	900	700
$\Delta\lambda$	10	100	10	100	400

All the optical components of ZEUS are mounted on a breadboard (600x450x60 mm^3),

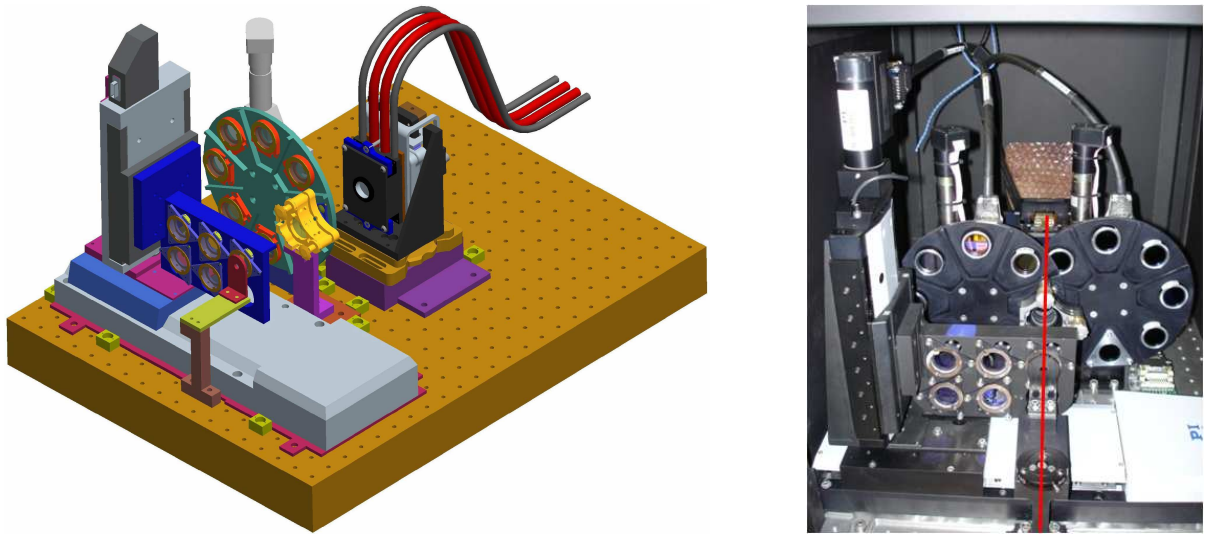

Figure 4.9: Left: CAD view of the ZEUS sensor. Right: Picture of the ZEUS sensor. The red line represents the optical path. Courtesy of K. Dohlen [22].

shown in Figure 4.9. The selection of the phase mask is done with a very high precision x/y translation stage. The color filters and neutral density filters are placed on two rotary wheels. The neutral density filter wheel also contains a lens to produce an image of the mask on the CCD detector. This lens is used during the alignment procedure of the different phase masks.

Part II

Zernike Phase Contrast Sensor

This part of the thesis is dedicated to the Zernike Phase Contrast Sensor.

A general theoretical study of the sensor is given in detail in Chapter 5. After a description of the principle of the phasing sensor in Section 5.1, a mathematical description of the sensor is given in Section 5.2. Smooth aberrations are first studied (Section 5.3). In particular, Section 5.3.3 shows that the sensor behaves as a high pass filter of the phase. The response of the sensor to a piston step is studied in Section 5.4, without and with atmospheric disturbances. The performance of the sensor, in terms of Fisher information in the presence of atmospheric disturbances, is analyzed in Section 5.5.

The Zernike Phase Contrast Sensor was part of the Active Phasing Experiment, under the acronym ZEUS[1]. All the algorithms which have been developed in the framework of APE, for the analysis of the signals delivered by the sensor, are then described in Chapter 6: image normalization (Section 6.1), pupil registration (Section 6.2), signal extraction (Section 6.3), fitting algorithm (Section 6.4), capture range (Section 6.5), tip-tilt analysis (Section 6.6) and singular value decomposition (Section 6.7).

Finally, the results obtained with APE in the laboratory and on sky at the VLT are presented in chapters 7 and 8, respectively. The theoretical predictions are confirmed by the experimental data. A typical image obtained with the Zernike Phase Contrast Sensor, on sky at the VLT, can be seen in Figure 4.10.

Finally, the last Chapter of this thesis (Chapter 9), shows how the theory of diffraction for segmented mirrors can be applied on the images of the Zernike Phase Contrast Sensor, which have been obtained on sky at the VLT.

[1] ZErnike Unit for Segment phasing

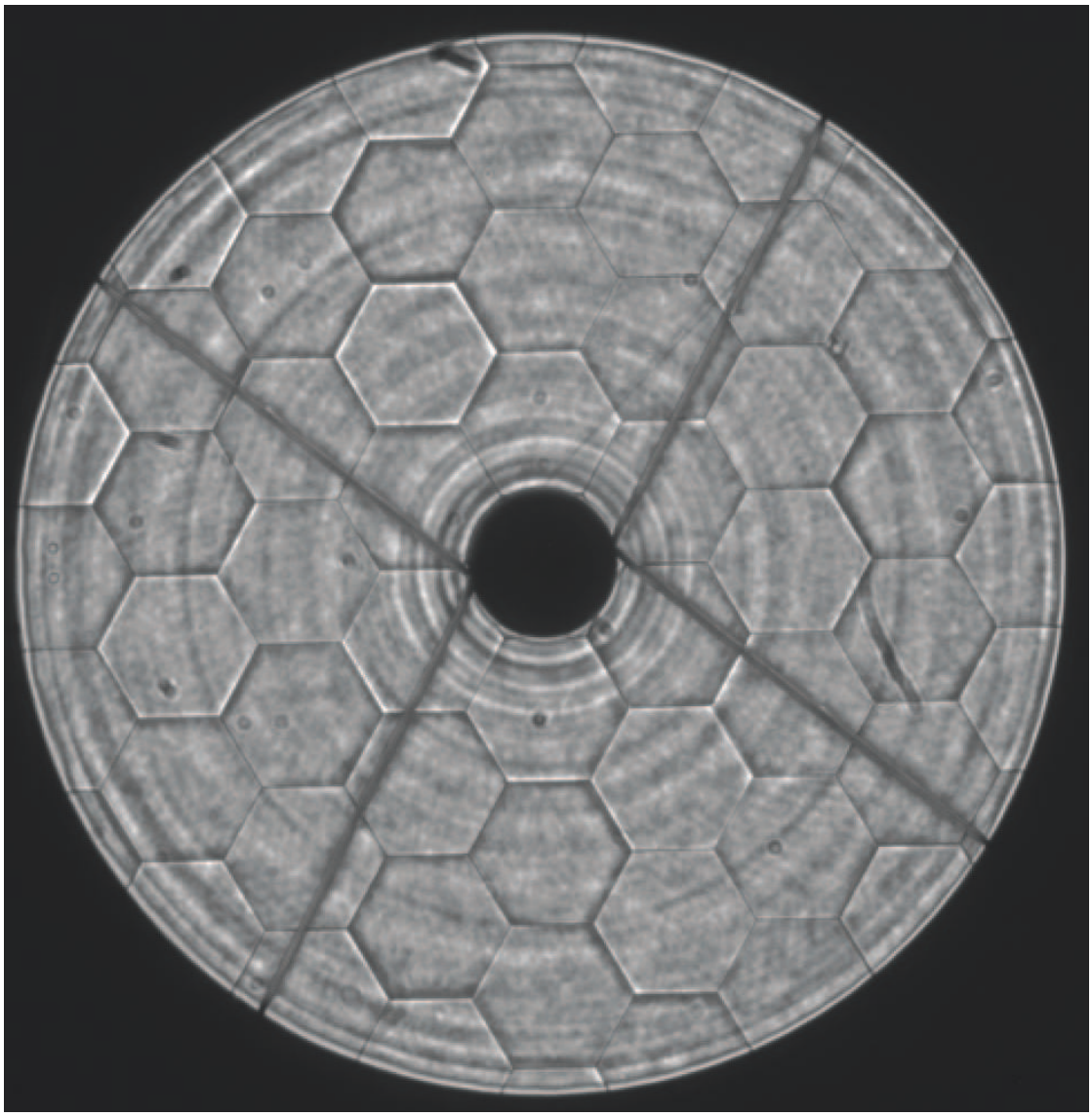

Figure 4.10: Image obtained with the ZEUS sensor on sky.

Chapter 5

Theory

5.1 General principle

The concept of the Zernike Phase Contrast Sensor has its origins in the Mach-Zehnder interferometer, already presented in Section 3.3.3. The delicate alignment between the two arms of the Mach-Zehnder interferometer is overcome in the Zernike Phase Contrast Sensor with the introduction of a simple phase mask in a focal plane [21]. After the phase mask, a lens projects the image of the pupil of the telescope on a CCD detector, as shown in Figure 5.1.

The phase mask consists of a cylindrical pellet etched into a substrate with a diameter of the order of the seeing disk and a depth of the order of a fraction of the wavelength of the light. The phase mask is shown in Figure 5.2. When the focal plane of the telescope is centered on the cylindrical cavity, a phase shift, or equivalently an optical path difference, is introduced between the center of the PSF and the outer rings of the PSF.

When the diameter of the cavity is close to that of the seeing disk, the low frequency components of the wavefront, in particular the aberrations generated by atmospheric disturbances are filtered out by the phase mask whereas the high frequency components of the wavefront, which correspond to the wavefront discontinuities generated by the pupil aberrations, are transmitted and finally appear as intensity variations on the detector.

This principle is similar to the famous Zernike phase contrast method [92, 91] for which Fritz Zernike received the Nobel prize in 1953.

The variations of the intensity in the plane of the exit pupil, which are generated by the misalignments of the segments, represent the signal of the Zernike Phase Contrast Sensor.

The piston information in the signal can be optimized by adjusting the diameter of the cavity, called the pinhole (as for the Mach-Zehnder interferometer) and by adjusting the depth of the cavity, generating an optical path difference (OPD).

The optimum diameter of the pinhole is approximately equal to the diameter of the seeing disc. The highest contrast of the signal is obtained for an OPD of $\lambda/4$ [75] as will be shown theoretically in Section 5.4.

5.2 Mathematical description of the sensor

Let $\mathbf{r}$, with rectangular coordinates (x, y), be the position vector in the pupil plane and let $\boldsymbol{\rho}$, with polar coordinates (ρ, ϑ), be the position vector in the focal plane. The coordinate ρ will be defined as an angular coordinate on the sky.

$U_1(\mathbf{r})$ is defined as the complex amplitude in the plane of the entrance pupil, in front of the phase mask, and $U_2(\mathbf{r})$ as the complex amplitude in a pupil plane after the phase mask as shown in Fig. 5.1.

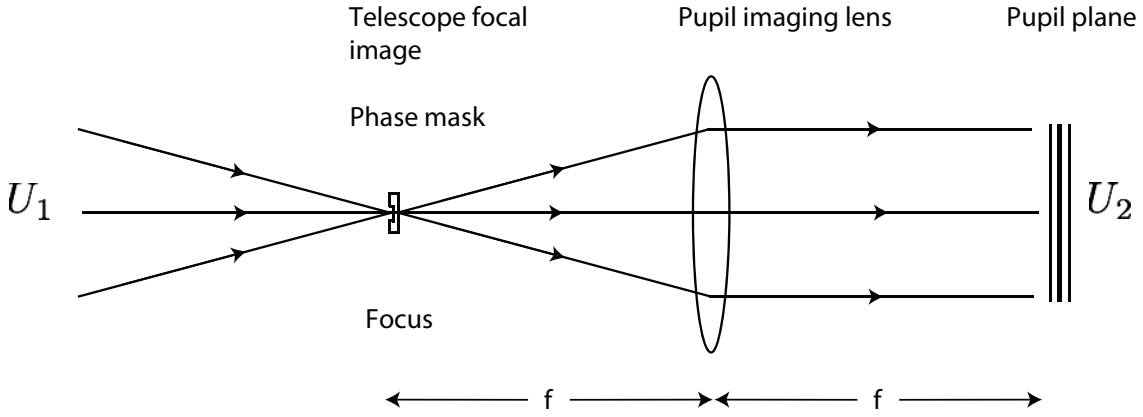

Figure 5.1: Zernike phasing sensor layout: After the filtering of the incoming wavefront U_1 by the phase mask (shown in detail in Fig. 5.2) in the focal plane, the pupil is re-imaged on the detector plane, U_2, by a pupil re-imaging lens of focal length f.

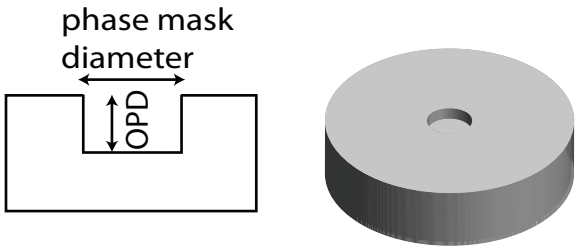

Figure 5.2: The phase mask consists of a cylindrical pellet, etched within a substrate, with a depth corresponding to the OPD and with a diameter noted as phase mask diameter in the figure.

The phase mask, illustrated in Fig. 5.2, can be described mathematically by the following expression

$$b(\boldsymbol{\rho}) = 1 + [\exp(i\psi_0) - 1]\,\Pi(\boldsymbol{\rho}), \tag{5.1}$$

where ψ_0 is the phase shift introduced by the phase mask. If the diameter of the phase

mask is represented by a, $\Pi(\boldsymbol{\rho})$ is given by

$$\Pi(\boldsymbol{\rho}) = \begin{cases} 1 & \text{if } |\boldsymbol{\rho}| \leq \frac{a}{2} \\ 0 & \text{if } |\boldsymbol{\rho}| > \frac{a}{2} \end{cases} . \tag{5.2}$$

We also refer to this type of mask as the sharp edge pinhole.

As for the Mach-Zehnder interferometer studied in [86], the case of a phase mask with apodized edges with a Gaussian function is also studied[1]:

$$\Pi(\boldsymbol{\rho}) = \exp\left[-(\frac{\boldsymbol{\rho}}{(2\sqrt{\ln 2})^{-1}a})^2\right]. \tag{5.3}$$

In this case the pinhole size a is defined by the full width at half maximum of the Gaussian function (Eq. (5.3)).We also refer to this type of mask as the Gaussian pinhole.

The complex amplitude in the plane of the exit pupil can be expressed as the convolution of the complex amplitude in the plane of the entrance pupil and the Fourier transform $T(\mathbf{r})$ of the transmission function of the phase mask $\Pi(\boldsymbol{\rho})$:

$$U_2(\mathbf{r}) = U_1(\mathbf{r}) + (\exp(i\psi_0) - 1)\frac{1}{\lambda^2}\int U_1(\mathbf{r}')T(\mathbf{r} - \mathbf{r}')\mathrm{d}\mathbf{r}' \tag{5.4}$$

where for the sharp edge pinhole

$$T(\mathbf{r}) = \int \Pi(\boldsymbol{\rho})\exp(-i\frac{2\pi}{\lambda}\boldsymbol{\rho}\cdot\mathbf{r})\mathrm{d}\boldsymbol{\rho} \tag{5.5}$$

$$= \frac{b^2\lambda^2}{4\pi}\frac{2J_1(b\mathbf{r})}{(b\mathbf{r})}, \tag{5.6}$$

$b = \dfrac{\pi a}{\lambda}$.

For the apodized pinhole

$$T(\mathbf{r}) = \frac{b^2\lambda^2}{\pi}\exp\left[-(b\mathbf{r})^2\right] \tag{5.7}$$

and $b = \dfrac{0.6\pi a}{\lambda}$.

The intensity in the plane of the exit pupil, that is the *signal* of the Zernike Phase Contrast Sensor, is given by

$$S(\mathbf{r}) = |U_2(\mathbf{r})|^2. \tag{5.8}$$

Before we study the signal of the Zernike Phase Contrast Sensor using diffraction theory in the case of piston errors, we shall first understand the properties of the signal, its relation to the complex amplitude $U_1(\mathbf{r})$ (see Section 5.3.1) and its relation to the phase $\varphi(\mathbf{r})$ (see Section 5.3.2). In Section 5.3.3 we show that the sensor behaves as a high pass filter of the phase [89].

[1]We will see in Section 5.4.5 that this phase mask can also be used to model the effects generated by the atmosphere.

5.3 Theoretical signal for smooth aberrations

The results presented in this section were obtained in close collaboration with N. Yaitskova and are based on an ESO technical report [89].

5.3.1 Variations of the complex amplitude

In this section, the relation between the complex amplitude $U_1(\mathbf{r})$ and the signal $|U_2(\mathbf{r})|^2$ of the sensor is studied.

The Fourier transform $T(\mathbf{r})$ of the symmetric functions $\Pi(\boldsymbol{\rho})$, expressed in Eqs. (5.2) and (5.3), respectively, is also a symmetric function with a characteristic size l, which is inversely proportional to the pinhole size a, that is $l \approx a^{-1}$. For the apodized pinhole, the characteristic size is $l = \lambda/((2\sqrt{\ln 2})^{-1}\pi a)$.

If the diameter of the pinhole is larger than the Airy disk corresponding to a diameter D of the pupil, that is $a \gg \frac{\lambda}{D}$ or $l < D$, and the complex amplitude $U_1(\mathbf{r})$ is produced by wavefront errors with a correlation length larger than l (such as residual polishing errors, atmospheric turbulence), the integration in Eq. (5.4) is performed within a limited domain l, where the function $U_1(\mathbf{r})$ can be expanded in a Taylor series:

$$U_1(\mathbf{r}') = U_1(\mathbf{r}) + \sum_{n=1}^{\infty} \frac{1}{n!} \frac{\mathrm{d}^n U_1(\mathbf{r})}{\mathrm{d}\mathbf{r}^n} (\mathbf{r}' - \mathbf{r})^n. \tag{5.9}$$

For the calculation of $U_2(\mathbf{r})$ in Eq. (5.4), the terms with odd n cancel out due to the convolution with the symmetric function $T(\mathbf{r})$. If we keep only the first quadratic term, Eq. (5.4) becomes:

$$U_2(\mathbf{r}) = \exp(i\psi_0) U_1(\mathbf{r}) + \frac{1}{2}(\exp(i\psi_0) - 1) \Delta U_1(\mathbf{r}) \frac{1}{\lambda^2} \int \mathbf{r}'^2 T(\mathbf{r}')^2 \mathrm{d}^2\mathbf{r}' \tag{5.10}$$

where Δ is the Laplace operator.
The integral in Eq. (5.10) is given by

$$\int \mathbf{r}'^2 T(\mathbf{r}')^2 \mathrm{d}^2 r' = \frac{2\lambda^2}{\alpha b^2} \tag{5.11}$$

where $\alpha = 0.68$ for the sharp edge mask[2] and $\alpha \approx 4$ for the apodized mask[3]. Therefore,

$$U_2(\mathbf{r}) = \exp(i\psi_0) U_1(\mathbf{r}) + (\exp(i\psi_0) - 1) \frac{1}{\alpha b^2} \Delta U_1(\mathbf{r}). \tag{5.12}$$

The intensity in the plane of the output pupil is given by:

$$|U_2(\mathbf{r})|^2 = |U_1(\mathbf{r})|^2 + \frac{2}{\alpha b^2} \mathrm{Re}\{[1 - \exp(-i\psi_0)] U_1^*(\mathbf{r}) \Delta U_1(\mathbf{r})\}. \tag{5.13}$$

The first term is the intensity in the plane of the entrance pupil and the second term is proportional to the Laplacian and to the complex conjugate of the complex amplitude in the plane of the entrance pupil. The terms in ΔU^2 have been neglected.

[2] analytical integration
[3] numerical integration

5.3.2 Variations of the phase

In this section, the relation between the phase in the plane of the entrance pupil and the signal is studied. The modulus of the complex amplitude is assumed to be constant and the wavefront $\varphi(\mathbf{r})$ is considered to be a smooth, differentiable function such that

$$U_1(\mathbf{r}) = A\exp[i\varphi(\mathbf{r})], \tag{5.14}$$

where A is the constant intensity of the complex amplitude in the plane of the entrance pupil.
It is easy to show that

$$\Delta U_1(\mathbf{r}) = U_1(\mathbf{r})[i\Delta\varphi(\mathbf{r}) - |\nabla\varphi(\mathbf{r})|^2]. \tag{5.15}$$

Substituting Eq. (5.15) into Eq. (5.13) gives

$$|U_2(\mathbf{r})|^2 = A^2\left[1 + \frac{2}{\alpha b^2}\left([1-\cos(\psi_0)]|\nabla\varphi(\mathbf{r})|^2 - \sin(\psi_0)\Delta\varphi(\mathbf{r})\right)\right]. \tag{5.16}$$

The signal of the Zernike Phase Contrast Sensor is a linear combination of the Laplacian of the phase and the square modulus of the gradient of the phase. The coefficients of these two terms depend on the OPD of the phase mask. If the OPD equals $\lambda/4$ ($\psi_0 = \pi/2$) and if the intensity in the plane of the entrance pupil is normalized such that $A = 1$, the intensity $|U_2(\mathbf{r})|^2$ can be expressed as

$$|U_2(\mathbf{r})|^2 = 1 + \frac{2}{\alpha b^2}\left[|\nabla\varphi(\mathbf{r})|^2 - \Delta\varphi(\mathbf{r})\right]. \tag{5.17}$$

5.3.3 Spatial filter of the phase

The general principle of the phase filtering sensor is that the phase mask acts as a high-pass filter on the phase, suppressing the low frequency components of the wavefront. With a simple mathematical development, we find an expression for the filter. This result will also be used in Chapter 9.

If $F(\mathbf{r})$ is a signal constructed from $|U_2(\mathbf{r})|^2$ such that $|U_2(\mathbf{r})|^2 = 1 + F(\mathbf{r})$, with $U_2(\mathbf{r})$ given by Eq. (5.17), the signal is given by the following expression:

$$F(\mathbf{r}) = \frac{2}{\alpha b^2}\left[|\nabla\varphi(\mathbf{r})|^2 - \Delta\varphi(\mathbf{r})\right]. \tag{5.18}$$

The two-dimensional Fourier transform of Eq. (5.18), $\widehat{F}(\mathbf{w})$, leads to the following expression:

$$\begin{aligned}\widehat{F}(\mathbf{w}) &= \int F(\mathbf{r})\exp(-i\frac{2\pi}{\lambda}\mathbf{w}\cdot\mathbf{r})\mathrm{d}\mathbf{r} \\ &= \int \frac{2}{\alpha b^2}\left[|\nabla\varphi(\mathbf{r})|^2 - \Delta\varphi(\mathbf{r})\right]\exp(-i\frac{2\pi}{\lambda}\mathbf{w}\cdot\mathbf{r})\mathrm{d}\mathbf{r}.\end{aligned} \tag{5.19}$$

Assuming that at the limits of the integration the phase and its derivatives are zero, Eq. (5.19) becomes:

$$\widehat{F}(\mathbf{w}) = \frac{2}{\alpha b^2}\left(\frac{2\pi}{\lambda}\right)^2 |\mathbf{w}|^2 \left[|\widehat{\varphi}(\mathbf{w})|^2 + \widehat{\varphi}(\mathbf{w})\right]. \tag{5.20}$$

The Power Spectral Density (PSD) $\Phi_{\text{signal}}(\mathbf{w})$ of the signal $F(\mathbf{r})$ is defined as the square of the modulus of the Fourier transform. Since the higher power terms can be neglected for small phase errors, $\Phi_{\text{signal}}(\mathbf{w})$ is given by

$$\Phi_{\text{signal}}(\mathbf{w}) = |\widehat{F}(\mathbf{w})|^2 = \frac{4}{\alpha^2}\left(\frac{2\pi}{\lambda b}\right)^4 |\mathbf{w}|^4 \Phi_{\text{phase}}(\mathbf{w}) \tag{5.21}$$

where $\Phi_{\text{phase}}(\mathbf{w}) = |\widehat{\varphi}(\mathbf{w})|^2$ is the PSD of the phase.

The Zernike Phase Contrast Sensor behaves as a high-pass filter on the phase. The filter, noted as $H(\mathbf{w})$, is given by the following expression:

$$H(\mathbf{w}) = (1/\kappa a)^4 |\mathbf{w}|^4, \begin{cases} \kappa = 0.28 & \text{for the sharp edge phase mask ,} \\ \kappa = 0.42 & \text{for the gaussian profile phase mask ,} \end{cases} \tag{5.22}$$

and

$$\Phi_{\text{signal}}(\mathbf{w}) = H(\mathbf{w})\Phi_{\text{phase}}(\mathbf{w}). \tag{5.23}$$

5.4 Theoretical signal for piston steps

In this section the analytical expression for the signal produced by the Zernike phasing sensor in the presence of pure piston errors is derived using Fourier optics. The light is considered to be monochromatic.

The approach used in Section 5.3 where all aberrations were assumed to be smooth, cannot be applied when the wavefront is discontinuous. Therefore an analysis based on the theory of diffraction is used to calculate the signal, that is the intensity $|U_2(\mathbf{r})|^2$ in the plane of the exit pupil of the Zernike Phase Contrast Sensor in the presence of a piston error.

5.4.1 Definition of the wavefront error

With a local coordinate system centered on the border between two segments (the x-axis being perpendicular to the edge as shown in Figure 5.3), and with φ_1 and φ_2 being the piston phase values of two segments, the complex amplitude in the plane of the entrance pupil depends only on the x-coordinate and can be expressed as

$$U_1(\mathbf{r}) = U_1(x) = \begin{cases} \exp(i\varphi_1) = \exp(i\ k\ p_1) & \text{if } x < 0 \\ \exp(i\varphi_2) = \exp(i\ k\ p_2) & \text{if } x > 0 \end{cases} \tag{5.24}$$

where p_1 and p_2 are the piston values[4] of the two segments, λ is the wavelength of the light and $k = 2\pi/\lambda$ is the wavenumber.

$\Delta\varphi$ is defined as the phase jump generated by the phase difference $\varphi_2 - \varphi_1$ and Δp as the piston step generated by the piston difference $p_2 - p_1$, therefore $\Delta\varphi = k\Delta p$. Δp is the piston step measured on the wavefront, which is twice the value of the piston step measured on the surface of the mirror.

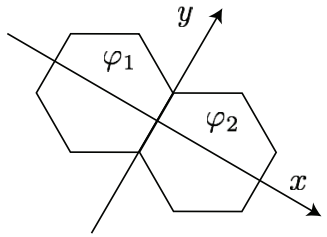

Figure 5.3: Cartesian coordinate system at the boundary between two segments and the phases φ_1 and φ_2 due to piston in each segment.

$U_1(x)$ will always be normalized such that the intensity in the plane of the entrance pupil is equal to 1:

$$\int \mathrm{d}x \; U_1^*(x) \; U_1(x) = 1. \tag{5.25}$$

5.4.2 Piston error without atmospheric disturbances

The results presented in this Section have been published by Surdej et al. [75].

From Eq. (5.4), the intensity on the detector is given by

$$\begin{aligned} S(x) &= |U_2(x)|^2 \\ &= |U_1(x)|^2 + 2[1 - \cos(\psi_0)]U_\mathrm{c}^*(x)U_\mathrm{c}(x) \\ &\quad +2\mathrm{Re}\{U_1^*(x)U_\mathrm{c}(x)(\exp(i\psi_0) - 1)\} \end{aligned} \tag{5.26}$$

where $U_\mathrm{c}(x)$ is the convolution of $U_1(x)$ and the Fourier transform of the transmission function $T(x)$ of the phase mask:

$$U_\mathrm{c}(x) = \frac{1}{\lambda}\int U_1(x')T(x - x')\mathrm{d}x'. \tag{5.27}$$

A normalization of the intensity in the plane of the entrance pupil, such that $|U_1(x)|^2 = 1$, leads to the following expression for the intensity in the plane of the exit pupil:

$$S(x) = 1 + F(x) \tag{5.28}$$

and the signal $F(x)$ is given by

$$F(x) = 2[1 - \cos(\psi_0)]U_\mathrm{c}^*(x)U_\mathrm{c}(x) + 2\mathrm{Re}\{U_1^*(x)U_\mathrm{c}(x)(\exp(i\psi_0) - 1)\}. \tag{5.29}$$

[4]Throughout this dissertation, all the piston values are measured on the wavefront.

Introducing Eqs. (5.24) and (5.27) into Eq. (5.29) leads to:

$$\begin{aligned} F(x) &= [1 - f(b|x|)]\text{sign}(x)\sin(\Delta\varphi)\sin(\psi_0) \\ &\quad -[1 - f(b|x|)]\ f(b|x|)[1 - \cos(\Delta\varphi)]\ [1 - \cos(\psi_0)]. \end{aligned} \tag{5.30}$$

The expressions for $f(b|x|)$ for the sharp edge and the Gaussian pinhole are given by the equations (3.25) and (3.24), respectively. Eq. (5.30) represents the signal profile of the Zernike Phase Contrast Sensor as a function of the phase jump $\Delta\varphi$ in the absence of atmospheric turbulence.

Note that the structure of the signal of the Zernike Phase Contrast Sensor is the same as for the curvature signal, expressed by Eq. (3.4).

The signal is a periodic function of $\Delta\varphi$, and the range of the measurable steps Δp, expressed in wavefront, is therefore limited to the range $[-\lambda/2, \lambda/2]$.

Except for $\psi_0 = 0$, the signal of the Zernike Phase Contrast Sensor is always the sum of two terms, an anti-symmetric and a symmetric one, shown in Figure 5.4.

The anti-symmetric term is given by:

$$F_{as}(x) = [1 - f(b|x|)][\text{sign}(x)\sin(\psi_0)\sin(\Delta\varphi)], \tag{5.31}$$

and the symmetric term by:

$$F_s(x) = -[1 - f(b|x|)]\ \{f(b|x|)[1 - \cos(\psi_0)][1 - \cos(\Delta\varphi)]\}. \tag{5.32}$$

The lobes, which are present in the signal with the sharp-edge mask, disappear with the apodized one.

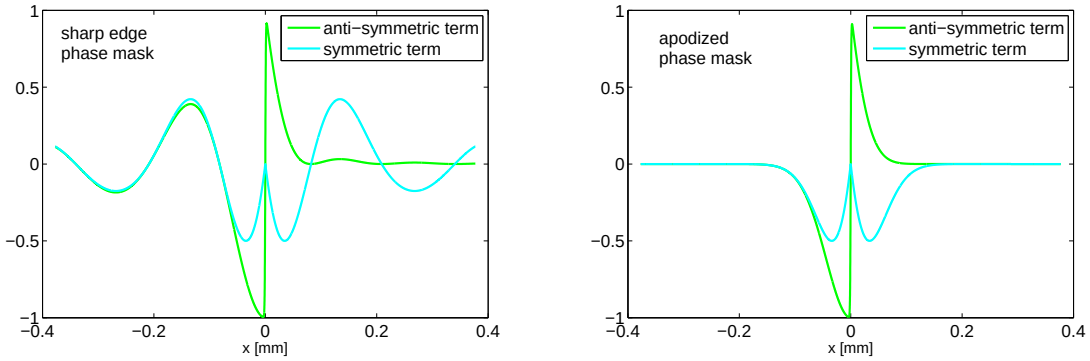

Figure 5.4: Symmetric and anti-symmetric parts of the signal for (left) the sharp edge phase mask and (right) the phase mask with the apodized profile.

The anti-symmetric term of the Zernike Phase Contrast Sensor is the same as the signal obtained with the Mach-Zehnder interferometer for an optical path difference of $\delta_0 = \lambda/4$ [86].

The weights of both terms depend on the values of $\Delta\varphi$ and ψ_0. They are plotted in Figure 5.5. The highest sensitivity to phase steps is, for the symmetric as well as for the anti-symmetric term, obtained if $\psi_0 = \pi/2$.

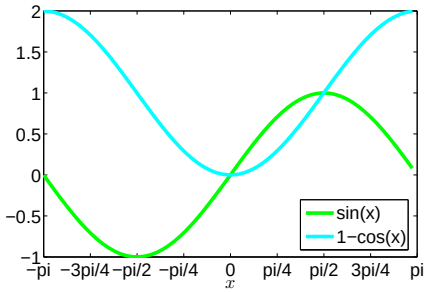

Figure 5.5: Weights of the symmetric and anti-symmetric term.

When the phase step is in the range $\Delta\varphi \in [0 \ldots \pi/2[$ (Fig. 5.6), the anti-symmetric part of the signal dominates, whereas in the range $\Delta\varphi \in [\pi/2 \ldots \pi[$, the symmetric part dominates. The same applies to the phase of the optical path difference ψ_0.

The phase mask used in the experiment is always the one with sharp edges. When the terms "sharp edge phase mask" or "gaussian phase mask" are used, they refer to the analytical expressions of functions (3.25) or (3.24) used inside the signal equation (5.30).

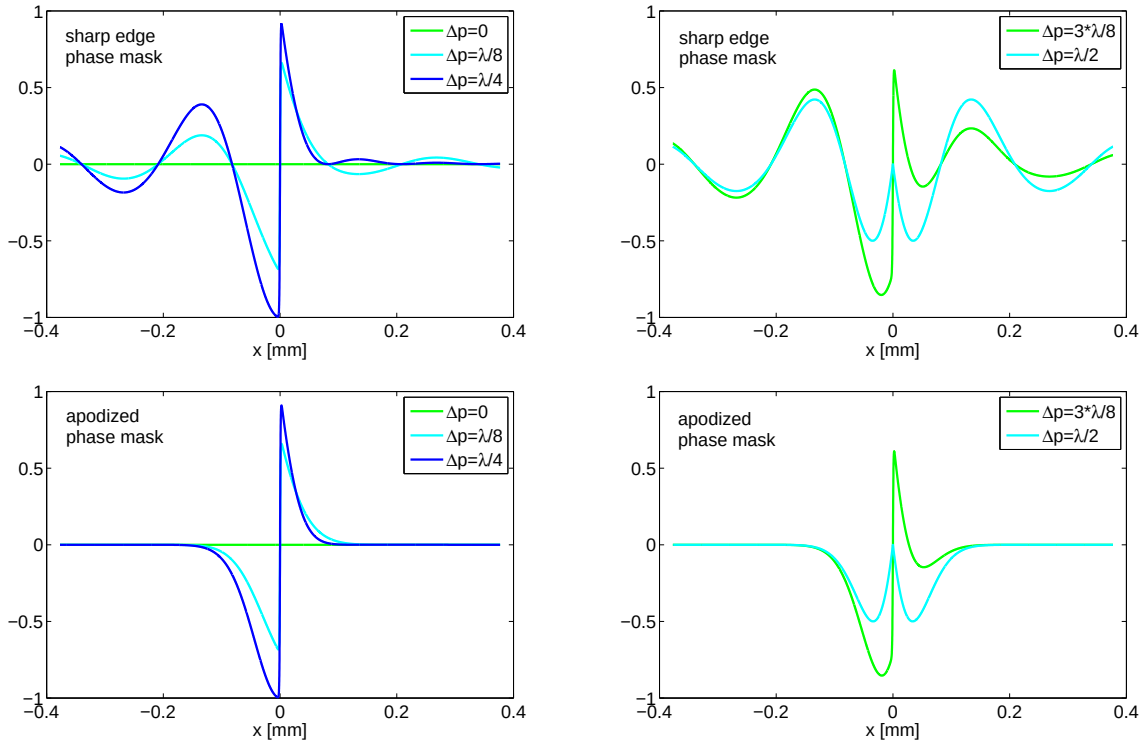

Figure 5.6: Theoretical signal profiles for different piston steps Δp and phase masks. (top) $\Delta p = 0$, $\Delta p = \lambda/8$, $\Delta p = \lambda/4$. (bottom) $\Delta p = 3\lambda/8$, $\Delta p = \lambda/2$. Both mask shapes are represented: the side lobes of the signal are a signature of the sharp edge phase mask.

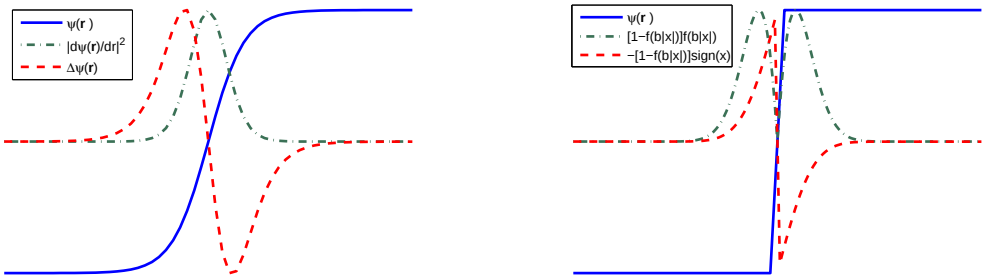

Figure 5.7: Left: Smooth function, its square of the module of its derivative and Laplacian. Right: Step function, $[1 - f(b|x|)]\ f(b|x|)$ and $[1 - f(b|x|)]\text{sign}(x)$.

A comparison of the exact signal due to a discontinuous step, described by Eq. (5.30), with the signal for a smooth aberration, described by Eq. (5.17), shows

$$\frac{2}{\alpha b^2}|\nabla\varphi(\mathbf{r})|^2 \propto [1 - f(b|x|)]\ \{f(b|x|)[1 - \cos(\Delta\varphi)]\} = F_1(b|x|), \tag{5.33}$$

$$\frac{2}{\alpha b^2}\Delta\varphi(\mathbf{r}) \propto [1 - f(b|x|)]\ \text{sign}(x)[\sin(\Delta\varphi)]\} = F_2(b|x|). \tag{5.34}$$

The symmetrical part $F_1(b|x|)$ of the signal is proportional to the modulus square of the gradient of the phase and $F_2(b|x|)$, or the anti-symmetrical part of the signal, is proportional to the Laplacian of the phase function. This comparison is illustrated in Figure 5.7. The plot on the left shows the phase as a step function approximated by a smooth function, the square of the module of its derivative and its Laplacian. The plot on the right shows the discontinuous phase, and the terms $F_1(b|x|)$ and $F_2(b|x|)$ of the signal, calculated with Fourier transformations. The anti-symmetrical part has a similar shape in both plots, which means that the approximation of the discontinuous step by a smoothed step is justified. This is, however, not the case for the symmetrical part, where the simple peak in the approximated signal is replaced by two peaks in the exact signal.

It is interesting to note that the signal of the Mach-Zehnder interferometer for the choice $\delta_0 = \lambda/4$ can be retrieved with a proper combination of two images of the Zernike Phase Contrast Sensor, acquired with different optical path differences:

$$F(x)|_{\psi_0=\pi/2} - F(x)|_{\psi_0=-\pi/2} = 2 \times S(x)|_{\text{MZ}} = 2 \times [1 - f(b|x|)][\text{sign}(x)\sin(\Delta\varphi)] \tag{5.35}$$

Signal width

The parameter b appearing in Eq. (5.30) is proportional to the pinhole diameter a, and inversely proportional to the wavelength λ:

$$b = \frac{\pi a}{\lambda}. \tag{5.36}$$

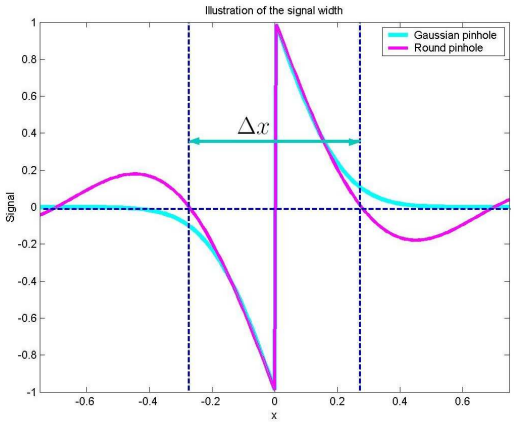

Figure 5.8: Illustration of the definition of the signal width for the sharp edge phase mask and gaussian profile phase mask.

This parameter determines the width of the signal, Δx, illustrated in Fig. 5.8. As for the signal obtained with the Mach-Zehnder interferometer, the width Δx of the signal is defined for the gaussian phase mask as the distance between two points where the intensity of the signal has dropped to 10% of its maximum value and for the sharp edge phase mask as the distance between the two first zeroes of the curve. It can be expressed in mm as [86]:

$$\Delta x \text{ [mm]} = \frac{253.5\lambda}{\text{c } a} \tag{5.37}$$

where c=$(2\sqrt{\ln 2})^{-1}$ for a gaussian type mask and c=1 for a sharp edge mask. The signal width is proportional to the wavelength and is inversely proportional to the pinhole size. The signal width is an important parameter to optimize because this is where the information on the phase discontinuity is contained (see Section 5.5).

5.4.3 Piston error in the presence of atmospheric disturbances

In the presence of atmospheric turbulence, the calculations which lead to the analytical expression for the signal given by Eq. (5.30) cannot be simplified. Therefore, we evaluate the expression for the signal by numerical integration.

The effects of the atmosphere can be taken into account by multiplying the complex amplitude in the plane of the entrance pupil, $U_1(x)$, given by Eq. (5.24), with a stochastic function $U_{\text{atm}}(x) = \exp[i\phi(x)]$ where $\phi(x)$ is the distortion of the wavefront due to the atmosphere.
In the one-dimensional case the complex amplitude $U_1^{\text{a}}(x)$ in the plane of the entrance pupil is given by:

$$U_1^{\text{a}}(x) = U_1(x)U_{\text{atm}}(x) \tag{5.38}$$

and the one-dimensional signal $S(x)$ becomes, in the presence of atmospheric turbulence:

$$\begin{aligned} S(x) &= |U_2(x)|^2 \\ &= |U_1^a(x)|^2 + 2\left[1-\cos(\psi_0)\right] U_{\rm c}^{a*}(x) U_{\rm c}^a(x) \\ &\quad + 2\ \mathrm{Re}\{U_1^{a*}(x) U_{\rm c}^a(x)\left[\exp(i\psi_0)-1\right]\}. \end{aligned} \tag{5.39}$$

As in the previous section, $U_{\rm c}^a(x)$ is the convolution of $U_1^a(x)$ and the Fourier transform of the transmission function $T(x)$ of the phase mask:

$$U_{\rm c}^a(x) = \frac{1}{\lambda}\int U_1^a(x+x^{'})T(x^{'})\mathrm{d}x^{'} \tag{5.40}$$

$$= \frac{1}{\lambda}\left[\exp(i\varphi_1)\int_{-\infty}^{-x} U_{\rm atm}(x+x')T(x^{'})\mathrm{d}x^{'} + \exp(i\varphi_2)\int_{-x}^{+\infty} U_{\rm atm}(x+x')T(x^{'})\mathrm{d}x^{'}\right] \tag{5.41}$$

and $U_{\rm c}^{a*}(x)$ is the complex conjugate of $U_{\rm c}^a(x)$.
After a normalization in the plane of the entrance pupil, such that $|U_1^a(x)|^2 = 1$, the intensity in the plane of the exit pupil can be expressed in the form $S(x) = 1 + F(x)$, with

$$\begin{aligned} F(x) &= 2\left[1-\cos(\psi_0)\right] < U_{\rm c}^{a*}(x) U_{\rm c}^a(x) > + 2\ \mathrm{Re}\{< U_1^{a*}(x) U_{\rm c}^a(x) > \left[\exp(i\psi_0)-1\right]\} \\ &= t_1(x) + t_2(x) \end{aligned} \tag{5.42}$$

where the angular type brackets symbolize the statistical averaging due to long exposures. The first term can be expressed as

$$\begin{aligned} t_1(x) &= 2\left[1-\cos(\psi_0)\right] < U_{\rm c}^{a*}(x) U_{\rm c}^a(x) > \\ &= 2\left[1-\cos(\psi_0)\right]\frac{1}{\lambda^2}\int \mathrm{d}x^{'}\int \mathrm{d}x^{''} U_1^*(x+x^{'}) U_1(x+x^{''}) T(x^{'}) T(x^{''}) \\ &\quad < U_{\rm atm}^*(x+x^{'}) U_{\rm atm}(x+x^{''}) > . \end{aligned} \tag{5.43}$$

For Kolmogorov turbulence statistics, the expression in the brackets is the optical transfer function (OTF) Ω of the atmosphere:

$$\Omega(x^{''}-x^{'}) =< U_{\rm atm}^*(x+x^{'}) U_{\rm atm}(x+x^{''}) >= \exp\left[-3.44\left(\frac{x^{''}-x^{'}}{r_0}\right)^{5/3}\right] \tag{5.44}$$

and r_0 is the atmospheric coherence length. We omit the details of the calculations. Finally Eq. (5.43) is given by:

$$\begin{aligned} t_1(x) &= 2\left[1-\cos(\psi_0)\right]\frac{1}{\lambda^2}\left(\int_{-\infty}^{-x}\mathrm{d}x'\exp(i\varphi_1)\left[\exp(-i\varphi_1)g_1(x^{'}) + \exp(-i\varphi_2)g_2(x^{'})\right]\right. \\ &\quad \left. + \int_{-x}^{+\infty}\mathrm{d}x'\exp(i\varphi_2)\left[\exp(i\varphi_1)g_1(x^{'}) + \exp(-i\varphi_1)g_2(x^{'})\right]\right), \end{aligned} \tag{5.45}$$

where

$$g_1(x') = \int_{-\infty}^{-x} \mathrm{d}x'' T(x') T(x'') \Omega(x'' - x') \tag{5.46}$$

$$g_2(x') = \int_{-x}^{+\infty} \mathrm{d}x'' T(x') T(x'') \Omega(x'' - x'). \tag{5.47}$$

With

$$g_{11}(x) = \int_{-\infty}^{-x} \mathrm{d}x' g_1(x') \tag{5.48}$$

$$g_{12}(x) = \int_{-\infty}^{-x} \mathrm{d}x' g_2(x') \tag{5.49}$$

$$g_{21}(x) = \int_{-x}^{+\infty} \mathrm{d}x' g_1(x') \tag{5.50}$$

$$g_{22}(x) = \int_{-x}^{+\infty} \mathrm{d}x' g_2(x') \tag{5.51}$$

Eq. (5.45) can be simplified to:

$$t_1(x) = 2\,[1 - \cos(\psi_0)]\,\frac{1}{\lambda^2}\{g_{11}(x) + \cos(\Delta\varphi)[g_{12}(x) + g_{21}(x)] + g_{22}(x)\}. \tag{5.52}$$

Note that $g_{12}(x) = g_{21}(x)$.

The second term of Eq. (5.42), $2\mathrm{Re}\{< U_1^{a*}(x) U_c^a(x) > [\exp(i\psi_0) - 1]\}$, becomes:

$$\begin{aligned} t_2(x) &= \frac{2}{\lambda}\,\mathrm{Re}\,\{U_1^*(x) \int \mathrm{d}x' U_1(x + x') \Omega(x') T(x') [\exp(i\psi_0) - 1]\} \\ &= \frac{2}{\lambda}\,\mathrm{Re}\,\{U_1^*(x)\,\{\exp(i\varphi_1) F_1(x) + \exp(i\varphi_2) F_2(x)\}\,\,[\exp(i\psi_0) - 1]\} \end{aligned} \tag{5.53}$$

$$t_2(x) = \begin{cases} \frac{2}{\lambda}\,\mathrm{Re}\,\{\exp(-i\varphi_1)\,\{\exp(i\varphi_1) F_1(x) + \exp(i\varphi_2) F_2(x)\}\,\,[\exp(i\psi_0) - 1]\} & \text{for } x < 0 \\ \frac{2}{\lambda}\,\mathrm{Re}\,\{\exp(-i\varphi_2)\,\{\exp(i\varphi_1) F_1(x) + \exp(i\varphi_2) F_2(x)\}\,\,[\exp(i\psi_0) - 1]\} & \text{for } x > 0, \end{cases} \tag{5.54}$$

where

$$F_1(x) = \int_{-\infty}^{-x} \mathrm{d}x' T(x') \Omega(x') \tag{5.55}$$

$$F_2(x) = \int_{-x}^{+\infty} \mathrm{d}x' T(x') \Omega(x'). \tag{5.56}$$

With

$$F_{12}(x) = \begin{cases} F_1(x) & \text{for } x < 0 \\ F_2(x) & \text{for } x > 0 \end{cases} \tag{5.57}$$

and

$$F_{21}(x) = \begin{cases} F_2(x) & \text{for } x < 0 \\ F_1(x) & \text{for } x > 0 \end{cases} \tag{5.58}$$

Eq. (5.53) is given by:

$$\begin{aligned} t_2(x) &= \frac{2}{\lambda} \left[F_{12}(x) \left[\cos(\psi_0) - 1\right] + F_{21}(x) \left\{\cos(\Delta\varphi) \left[\cos(\psi_0) - 1\right]\right.\right. \\ &\quad \left.\left. + \operatorname{sign}(x) \sin(\Delta\varphi) \sin(\psi_0)\right\}\right]. \end{aligned} \tag{5.59}$$

Finally, the signal in the presence of atmospheric turbulence is given by:

$$\begin{aligned} F(x) &= [1 - \cos(\psi_0)][\frac{2}{\lambda^2}\{g_{11}(x) + \cos(\Delta\varphi)(g_{12}(x) + g_{21}(x)) + g_{22}(x)\} \\ &\quad -\frac{2}{\lambda}\{F_{12}(x) + F_{21}(x)\cos(\Delta\varphi)\}] \\ &\quad +\frac{2}{\lambda}\operatorname{sign}(x)\sin(\Delta\varphi)\sin(\psi_0)F_{21}(x). \end{aligned} \tag{5.60}$$

The symmetric and anti-symmetric terms of the signal are now given by:

- Symmetric term:

$$\frac{2}{\lambda^2}(g_{11}(x) + \cos(\Delta\varphi)(g_{12}(x) + g_{21}(x)) + g_{22}(x)) - \frac{2}{\lambda}\{F_{12}(x) + F_{21}(x)\cos(\Delta\varphi)\} \tag{5.61}$$

- Anti-symmetric term:

$$\frac{2}{\lambda}\operatorname{sign}(x)\sin(\Delta\varphi)F_{21}(x). \tag{5.62}$$

Figure 5.9 shows the shape of the signal in the presence of different seeing conditions, characterized by the seeing disk, for a piston step of $\lambda/4$ and $\lambda/2$, respectively, and for a pinhole with a diameter of 1 arcsec. The signals shown in the plots were obtained after numerical integration of Eq. (5.60). It is obvious that the signal becomes less significant in deteriorating seeing conditions.

5.4.4 Dependence of the signal on the properties of the atmosphere and the phase mask

Figure 5.10 shows the signal profile for a piston step of $\lambda/4$, and the symmetrical and anti-symmetrical terms for four different sizes of the pinhole diameter and different values of the seeing. The phase shift introduced by the OPD is, as always, $\psi_0 = \pi/2$.

As shown in Section 5.4.2, the width of the signal decreases with an increase of the size of the pinhole (Eq. (5.37)).

The large oscillations produced by the sharp edge pinhole in the diffraction limited case seem to disappear in the presence of atmospheric turbulence, leading to a signal similar to the one obtained with the phase mask with a Gaussian profile.

It is interesting to analyze the effects due to atmospheric turbulence on the symmetric and anti-symmetric terms separately.

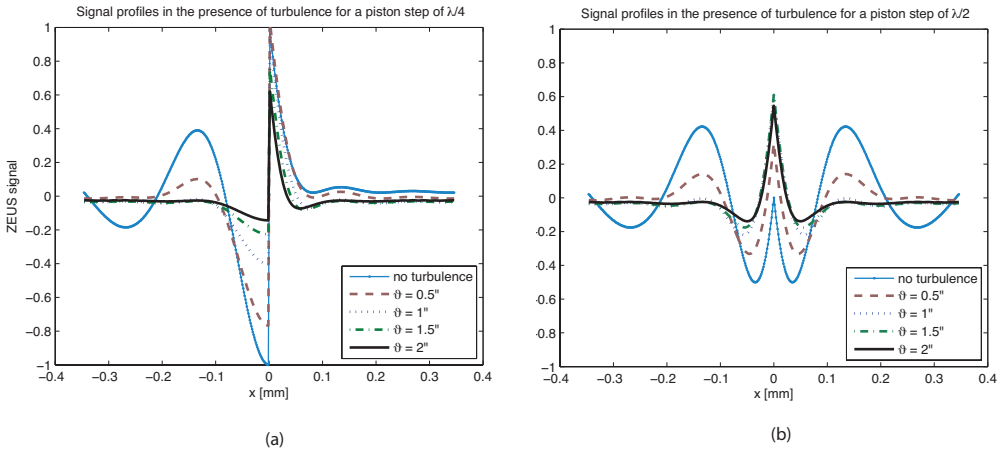

Figure 5.9: Signal profiles for different seeing conditions characterized by the seeing disk θ_{seeing} in the case of a round pinhole and piston step of (a) $\Delta p = \frac{\lambda}{4}$ and (b) $\Delta p = \frac{\lambda}{2}$.

Anti-symmetric term

Without the aberrations introduced by the atmosphere, the analytical expression for the anti-symmetric signal is identical to the signal obtained with the Mach-Zehnder interferometer with an optical path difference $\delta_0 = \lambda/4$. A comparison of the signals in Figure 5.10 shows that the influence of atmospheric turbulence on the anti-symmetric signal of the Zernike Phase Contrast Sensor is the same as on the anti-symmetric signal of the Mach-Zehnder interferometer, which can be found in [86].

As for the Mach-Zehnder interferometer, the anti-symmetric signal under the influence of atmospheric turbulence is given by

$$< S(x) >_{\text{Mach-Zehnder}} \approx \text{sign}(x)\sin(\Delta\varphi)p_{\text{seeing}}^{-1}[1 - f(\sqrt{p_{\text{seeing}}}/b|x|)]. \tag{5.63}$$

The parameter p_{seeing} can be expressed by the ratio of the seeing disk to the diameter of the pinhole

$$p_{\text{seeing}} = 1 + 1.24\left(\frac{\theta_{\text{seeing}}}{a}\right)^2. \tag{5.64}$$

From Eq. (5.63), both the amplitude and the width of the signal are modified in the presence of atmospheric turbulence.

As for the Mach-Zehnder interferometer, the width of the signal Δx given in Eq. (5.37), is, in the presence of atmospheric turbulence, modified to:

$$w_{\text{seeing}} = \frac{\Delta x}{\sqrt{p_{\text{seeing}}}} = \frac{253.5\ \lambda}{\text{c}\ a\ [1 + 1.24(\theta_{\text{seeing}}/a)^2]^{1/2}} \tag{5.65}$$

where c=$(2\sqrt{\ln 2})^{-1}$ for a gaussian type mask and c=1 for a sharp edge mask. The signal width is expressed in mm when λ is measured in μm and a in arcseconds. It is proportional

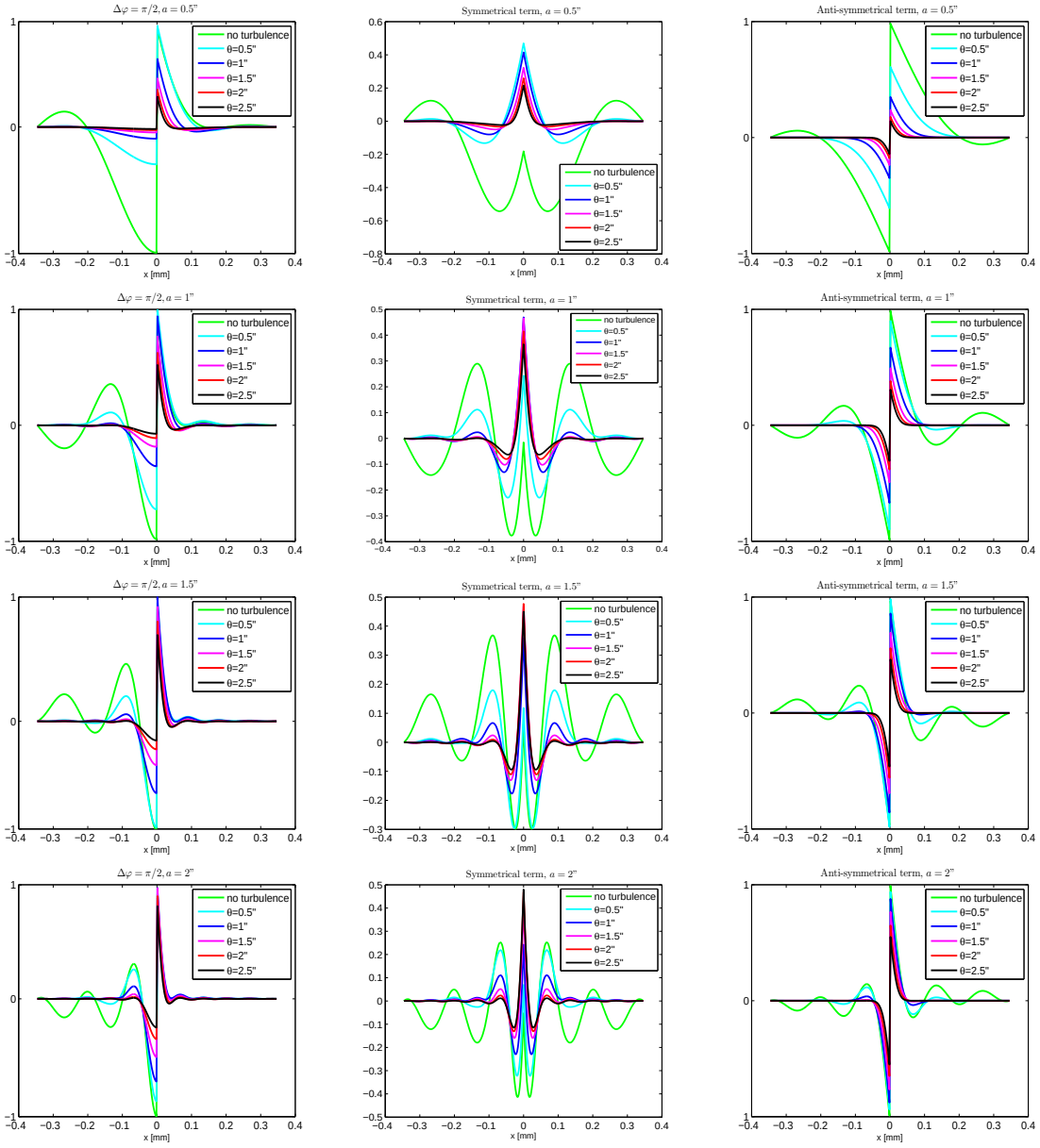

Figure 5.10: Signal profile for a step of $\lambda/4$ (column on the left), symmetrical (central column) and anti-symmetrical (column on the right) terms for different diameters of pinhole $a = 0.5$", $a = 1$", $a = 1.5$", $a = 2$" and for different seeing conditions.

to the wavelength and inversely proportional to the seeing and the size of the mask. A plot of Eq. (5.65) is shown in Figure 5.11 for different sizes of the pinhole.

Figure 5.12 shows the behavior of the signal width of the anti-symmetric term of the Zernike Phase Contrast Sensor as a function of the seeing for different sizes of pinhole.

The dependence of the width of the signal on the seeing is almost the same for the anti-symmetric term of the Zernike Phase Contrast Sensor and for the Mach-Zehnder

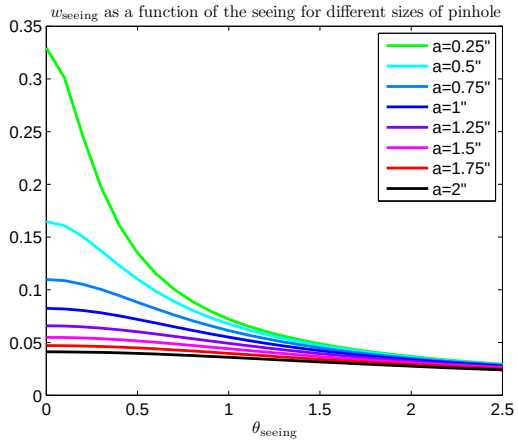

Figure 5.11: Width of the signal modified by the amplitude of θ_{seeing} for different sizes of pinhole.

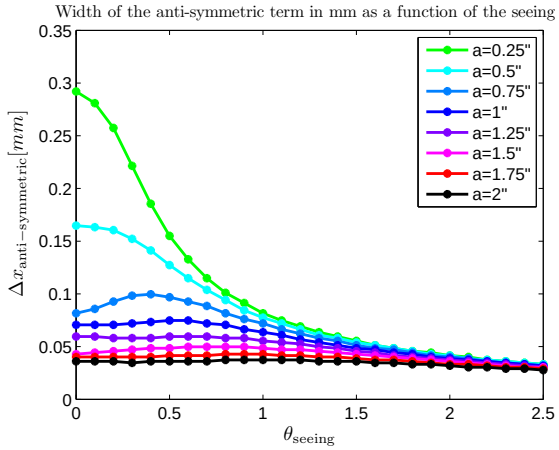

Figure 5.12: $\Delta x_{\text{anti-sym}}$ as a function of the seeing disk for different sizes of the pinhole diameter.

interferometer.

Symmetric term

The plots in Figure 5.10 show that the behavior of the symmetric term in the presence of atmospheric turbulence is different from the anti-symmetric one:

- the width of the signal is almost not modified by the seeing
- the amplitude of the side lobes is reduced
- a new peak appears at $x = 0$ with the amplitude of the peak depending on the combination of the seeing and the pinhole diameter.

Figure 5.13 shows the definition of the signal width for the symmetric term while Figure 5.14 shows its dependence on the seeing for different sizes of the pinhole diameter. The

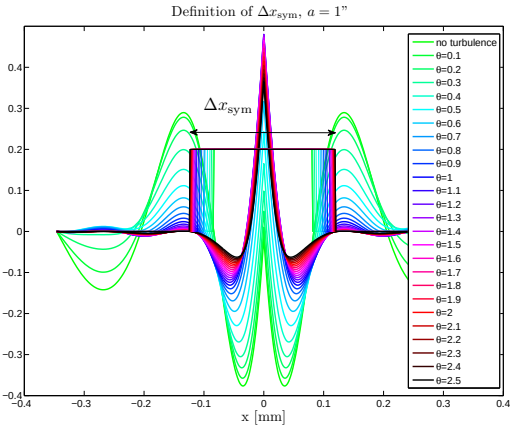

Figure 5.13: Definition of the width of the symmetric term, Δx_{sym}.

seeing almost does not affect the width of the symmetric term. However, a new peak

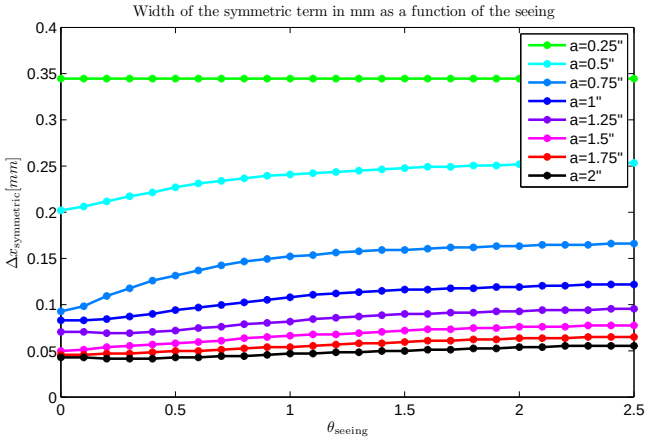

Figure 5.14: Δx_{sym} as a function of the seeing disk for different sizes of the pinhole diameter.

appears at the location of the phase discontinuity. The amplitude of the peak is plotted as a function of θ_{seeing} for different sizes of pinhole in Figure 5.15. When $a \approx \theta_{\mathrm{seeing}}$ the amplitude of the peak attains its maximum.

5.4.5 Simplified model of the signal in the presence of atmospheric turbulence

The final mathematical expression describing the signal is too complex to be used for the signal analysis algorithm. However, it has been shown in Section 5.4.4 that the signal can be well approximated by the signal obtained with the apodized mask.

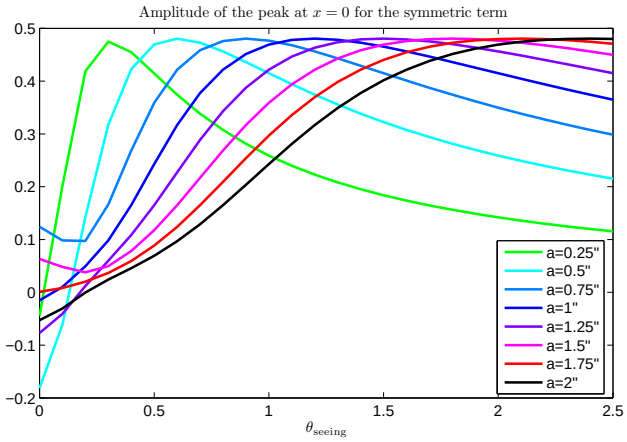

Figure 5.15: Amplitude of the peak at $x = 0$ of the symmetric term as a function of the seeing disk for different sizes of the pinhole diameter.

The influence of atmospheric turbulence on long exposure images is therefore modeled with the apodization of the mask, $\Pi(\boldsymbol{\rho})$, with the Gaussian function

$$\Pi(\boldsymbol{\rho}) = \exp\left[-\left(\frac{\boldsymbol{\rho}}{(2\sqrt{\ln 2})^{-1}a}\right)^2\right]. \tag{5.66}$$

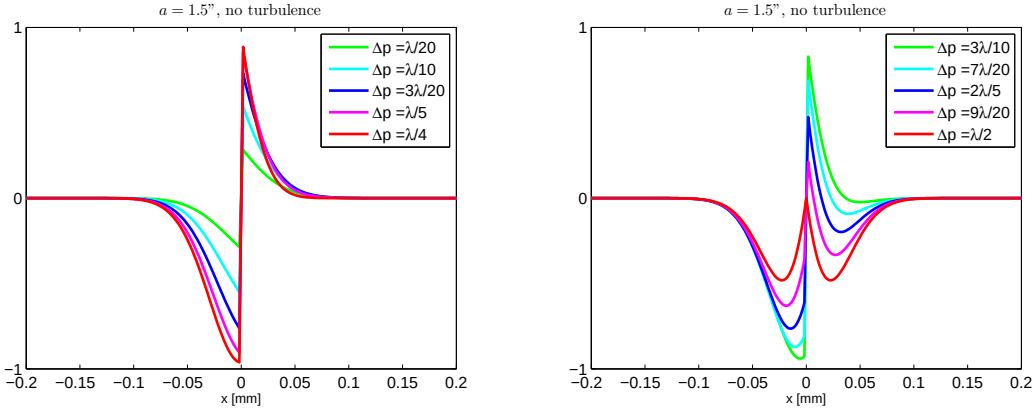

Figure 5.16: Signal profiles. (left: phase steps up to $\Delta p = \lambda/4$ and right: phase steps between $\Delta p = \lambda/4$ and $\Delta p = \lambda/2$) obtained with the gaussian phase mask ($a = 1.5$") and no turbulence.

Figure 5.16 shows the shape of the signal for different step sizes in the range $[\lambda/20, \lambda/2]$, with a gaussian phase mask and with a pinhole with a diameter of 1.5" and no turbulence.

Figure 5.17 shows the same signals with a sharp edge phase mask and three different seeing conditions: no turbulence, $\theta_{\text{seeing}} = 1$" and $\theta_{\text{seeing}} = 2$".

A comparison of Figure 5.16 with 5.17 shows that the effect of the atmosphere is a reduction of the amplitude of the side lobes of the signal generated by the diffraction of the light on the sharp edges of the mask.

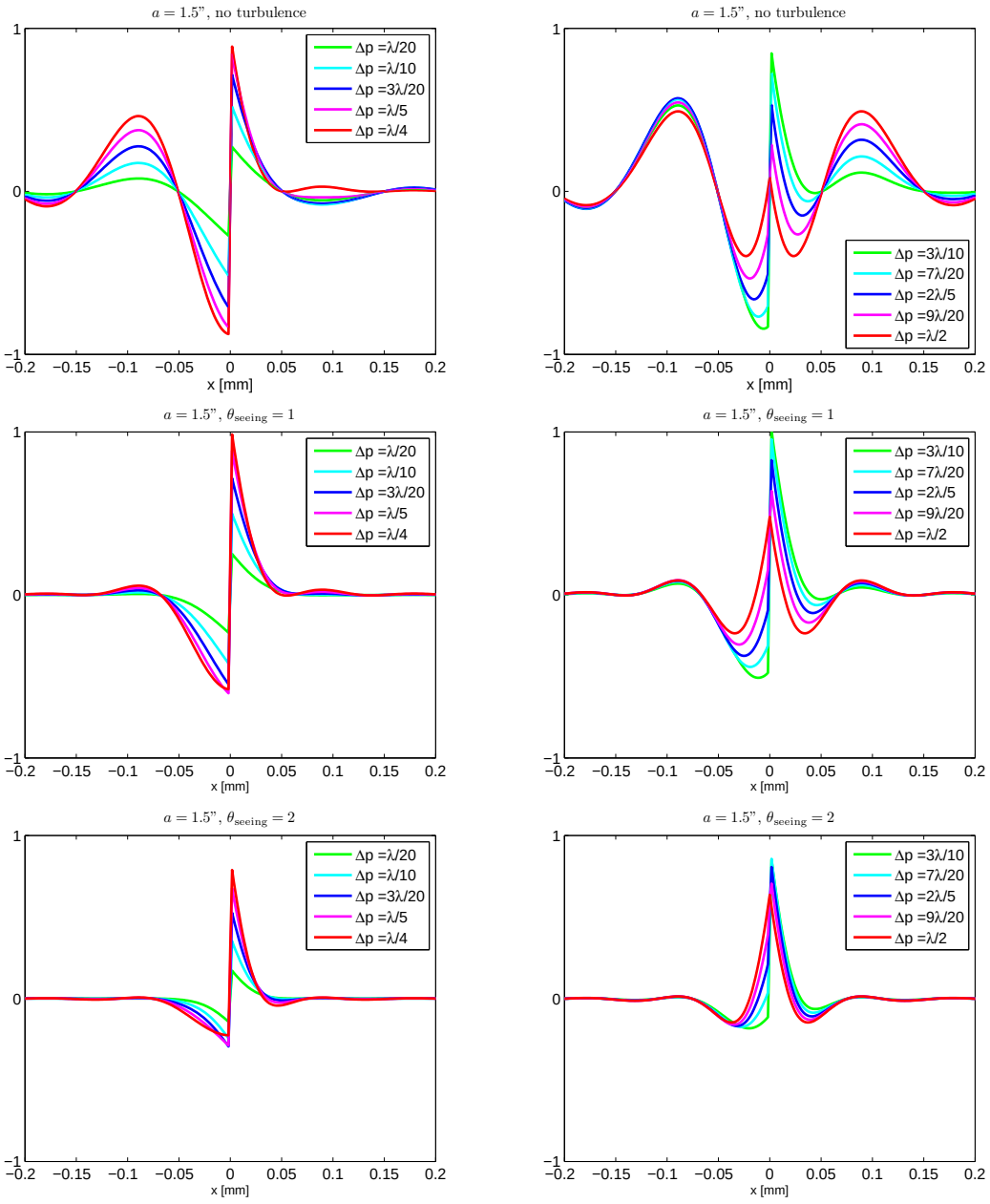

Figure 5.17: Signal profiles. (left: phase steps up to $\Delta p = \lambda/4$ and right: phase steps between $\Delta p = \lambda/4$ and $\Delta p = \lambda/2$) obtained with the gaussian phase mask ($a = 1.5$") and θ_{seeing} ranging from 0.5" to 2.5".

For piston steps Δp between 0 and $\lambda/4$, the gaussian mask is a good approximation. However, it fails for $\Delta p \to \lambda/2$ because of the new central peak in the symmetric term.

Adjusted signal width

For small signals and neglecting the symmetric term, the signal width w_{seeing} can be evaluated with the same approximation for the signal as the one given by Eq. (5.65).

In the next section we will see how the performance of the sensor can be predicted, using the Fisher information, for different combinations of the pinhole diameter and the seeing.

5.5 Performance and Fisher information

5.5.1 Definition of the Fisher information

The fundamental precision limits of all four phasing sensors studied in APE, including the Mach-Zehnder interferometer, have been calculated by L. Noethe and H. M. Adorf [60]. They are a basis for the understanding of the performances achieved on sky. The limit for the precision with which the height of the steps can be estimated with a given number of photons is evaluated for all sensors, however this study only includes the effect of the atmosphere for the Shack-Hartmann sensor. It shows that without atmospheric disturbances the Shack-Hartmann and the Pyramid sensor require twenty and ten times, respectively, fewer photons than the Mach-Zehnder interferometer to reach the same precision. However, during night observations and in the presence of atmosphere, the Zernike Phase Contrast Sensor and the Shack-Hartmann sensor have achieved very similar performances.

To understand the performance obtained in the laboratory and on sky with the Zernike Phase Contrast Sensor, we have applied the same methodology to obtain the Fisher information for the Zernike Phase Contrast Sensor also in the presence of noise such as the one generated by the atmosphere. In particular, the aim of these calculations is to find the optimal diameter of the phase mask for a given value of the seeing disk.

We first recall the definition of the Fisher information as explained in [60].

The likelihood function $p\,(x|\Delta\varphi)$ describes the "likelihood" to register a photon on the detector as a function of the spatial variable x on the detector, given a certain value of a parameter, the segment phase step $\Delta\varphi$. It corresponds to the signal of the sensor, as described by Eq. (5.30) without seeing and Eq. (5.60) with seeing.

The Fisher information is defined as:

$$I_F = 4 \int_{-\infty}^{\infty} \mathrm{d}x \; p(x|\Delta\varphi) \left(\frac{\partial \ln p(x|\Delta\varphi)}{\partial \Delta\varphi} \right)^2 . \tag{5.67}$$

The integrand in equation (5.67), the *Fisher information density* $i_F(x|\Delta\varphi)$, can be written as

$$\begin{aligned} i_F(x, \Delta\varphi) &= 4 \left(\frac{\partial q(x|\Delta\varphi)}{\partial \Delta\varphi} \right)^2 \\ &= \frac{1}{p(x|\Delta\varphi)} \left(\frac{\partial p(x|\Delta\varphi)}{\partial \Delta\varphi} \right)^2 . \end{aligned} \tag{5.68}$$

where $q\left(x|\Delta\varphi\right)$ denotes the real-valued likelihood amplitude, defined by

$$q\left(x|\Delta\varphi\right) = \sqrt{p\left(x|\Delta\varphi\right)}. \tag{5.69}$$

The Fisher information I_F can then be computed as:

$$I_F = 4\int_{-\infty}^{\infty} \mathrm{d}x \left(\frac{\partial q(x|\Delta\varphi)}{\partial\Delta\varphi}\right)^2. \tag{5.70}$$

5.5.2 Measurement of a piston step

The Fisher information density and the Fisher information are now calculated in the presence of Kolmogorov turbulence for the Zernike Phase Contrast Sensor.

The likelihood function $p\left(x|\Delta\varphi\right)$ to be introduced into the expressions (5.68) and (5.70) is given by

$$p(x|\Delta\varphi) = 1 + F(x) \tag{5.71}$$

where $F(x)$ is given by Eq. (5.30) for the case without atmospheric disturbances and by Eq. (5.60) for the case with atmospheric disturbances.

The Fisher information $i_F(x)$ is calculated for two values of the parameter $\Delta\varphi$, always with an Optical Path Difference $\delta_0 = \lambda/4$ or, equivalently, $\psi_0 = \pi/2$. The wavelength of the light used in the calculations is $\lambda = 650$ nm.

1. Limit values for small steps: $\Delta\varphi \to 0$

$$i_F(x, \Delta\varphi \to 0) = \left(\frac{2}{\lambda}\frac{F_{21}(x)\mathrm{sign}(x)}{\sqrt{p(x|\Delta\varphi \to 0)}}\right)^2 = \frac{4}{\lambda^2}F_{21}^2(x) \tag{5.72}$$

   In this limit, the Fisher information density is proportional to the square of the anti-symmetrical term of the signal. Since the signal is zero for $\Delta\varphi = 0$, the denominator is 1.

   Figure 5.18 shows the Fisher information density for different seeing conditions and different diameters of the pinhole.

   All the information on the phase step is concentrated near the phase discontinuity and the width of the Fisher information density corresponds to the width of the anti-symmetric signal, given by Eq. (5.65), since $i_F(x, \Delta\varphi \to 0) \sim (F_{21}(x))^2$.

   The Fisher information is now obtained with an integration of the Fisher information density from $x = -\infty$ to $x = +\infty$.

   The dependence of the Fisher information as a function of the seeing disk for different sizes of pinholes is shown in Figure 5.19. The maximum of the Fisher information depends on the combination of pinhole diameter a and seeing disk θ_{seeing}. The maximum is attained when

$$a = 1.5 \times \theta_{seeing}. \tag{5.73}$$

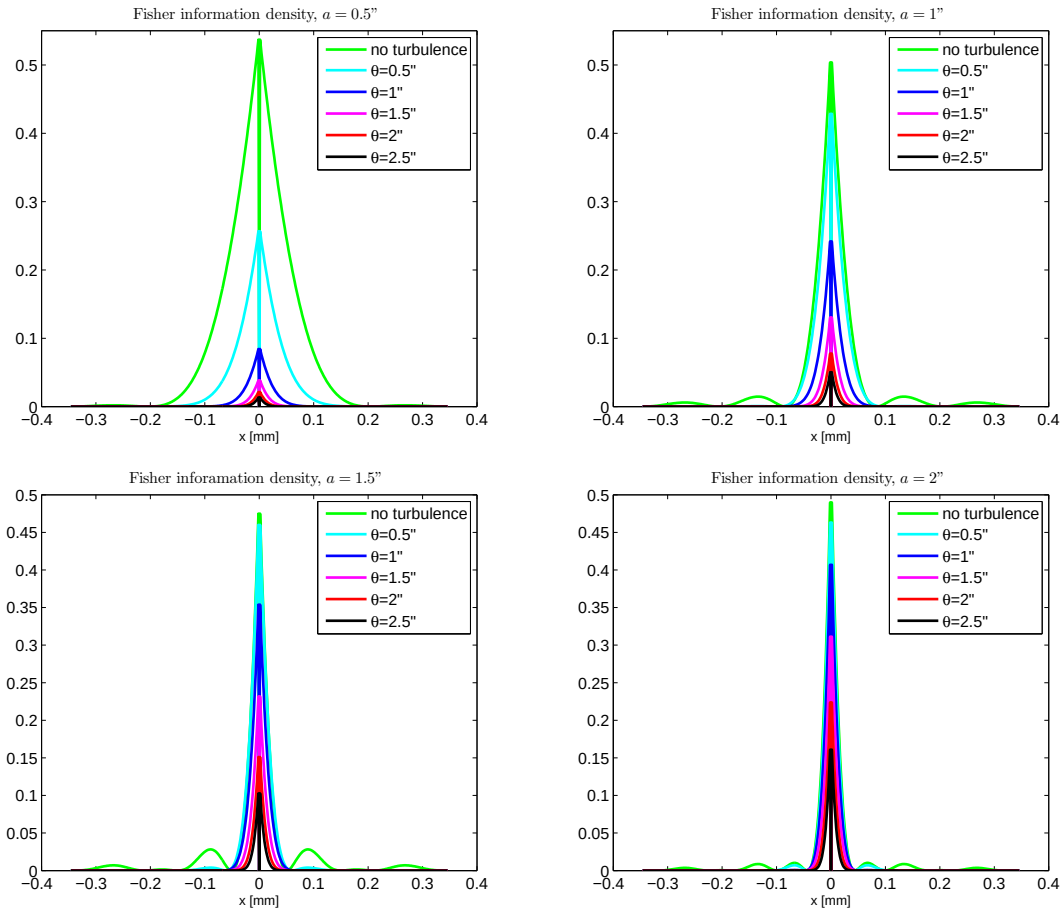

Figure 5.18: Fisher information density for $\Delta\varphi \to 0$ and for phase masks with different pinhole diameters a: $a = 0.5$", $a = 1$", $a = 1.5$", $a = 2$" and different seeing conditions.

This result can be compared to the optimal pinhole size found with the Mach-Zehnder interferometer, for different values of the gaps [86].

The Fisher information is by definition the integral of the Fisher information density and can therefore be approximated by the area under the curve of the Fisher information density. This area can be approximated by the area of a triangle, whose base is the width of the signal, given by w_{seeing} (Eq. (5.65)), and whose height is the amplitude of the signal, given by the term p_{seeing}^{-1}, which has been introduced in Eq. (5.63).

The area $(0.5 \cdot p_{\text{seeing}}^{-1} \cdot w_{\text{seeing}})$ is plotted as a function of the seeing for different diameters of pinhole in Fig. 5.20. The plots shown in the Figures 5.19 and 5.20 are very similar. The slight discrepancy between the values of the two plots around the origin can be explained by the side lobes of the signal (or of the Fisher information density), which are not taken into account in the calculation of the area of the triangle.

The similarity of the Fisher information with the parameter $(0.5 \cdot p_{\text{seeing}}^{-1} \cdot w_{\text{seeing}})$

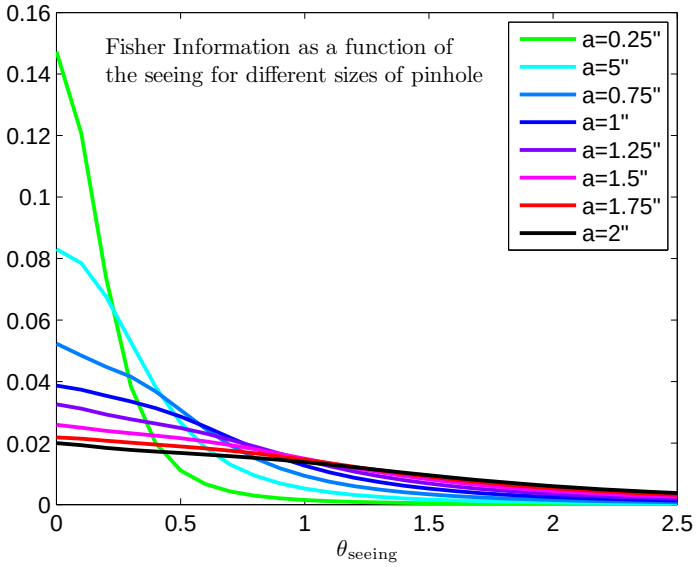

Figure 5.19: Fisher information for $\Delta\varphi \to 0$ and for phase masks with different pinhole diameters a and different seeing conditions ranging from $\theta_{\text{seeing}} = 0$" to $\theta_{\text{seeing}} = 2.5$".

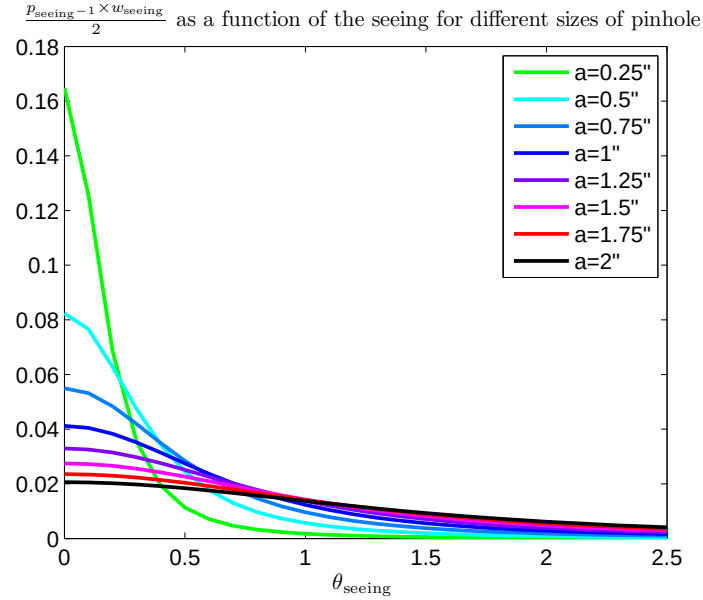

Figure 5.20: $\frac{p_{\text{seeing}}^{-1} \cdot w_{\text{seeing}}}{2}$ for phase masks with different pinhole diameters a and different seeing conditions ranging from $\theta_{\text{seeing}} = 0$" to $\theta_{\text{seeing}} = 2.5$".

justifies the use of this parameter for the estimate of the piston step from Mach-Zehnder data in [86].

2. Limit values for large phase steps: $\Delta\varphi \to \pi$

$$i_F(x, \Delta\varphi \to \pi) = \left(-\frac{2}{\lambda} \frac{F_{21}(x)\text{sign}(x)}{\sqrt{p(x|\Delta\varphi \to \pi)}} \right)^2 \tag{5.74}$$

The Fisher information density for $\Delta\varphi \to \pi$ is the same as for $\Delta\varphi \to 0$, except for the denominator, which corresponds now to $F(x)|_{\Delta\varphi\to\pi}$. Unlike the previous case ($\Delta\varphi \to 0$), it is not a constant but similar to curves in the middle column of Figure 5.10.

Nevertheless, the Fisher information is very similar to the previous case. However, the amplitude is approximately 30% smaller. All the information on the phase step is concentrated near the phase discontinuity, and, therefore, also in the new peak generated by the atmospheric disturbances.

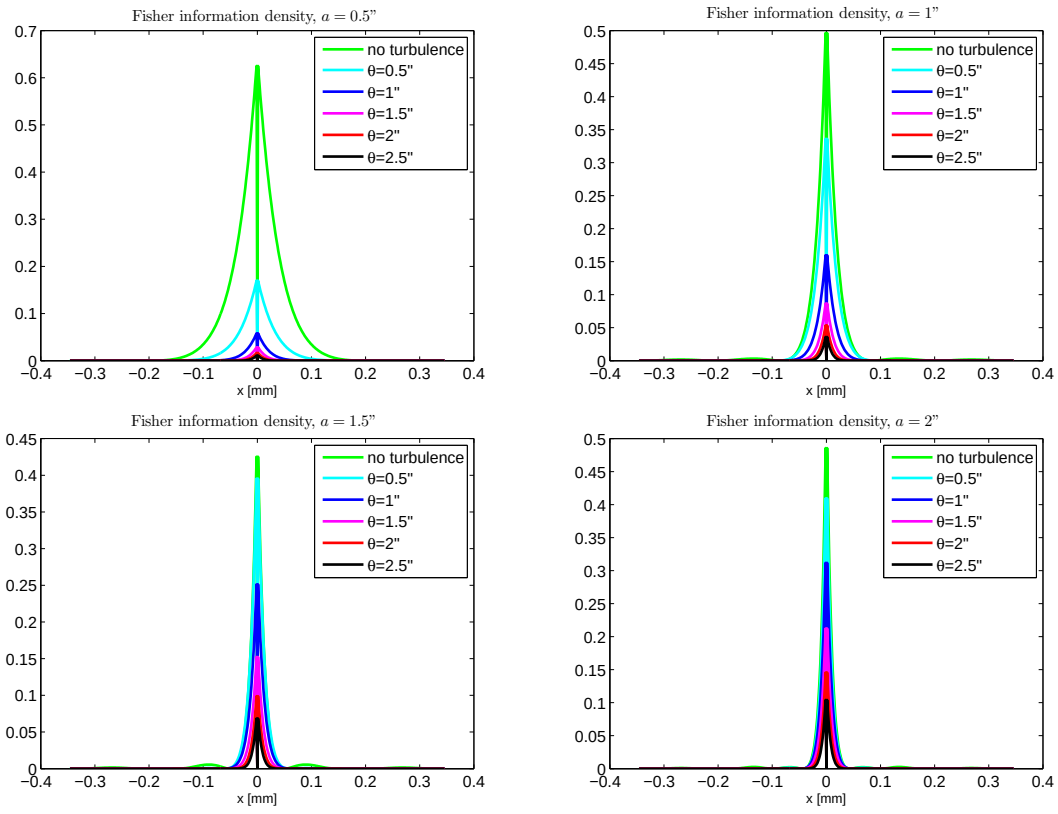

Figure 5.21: Fisher information density for $\Delta\varphi \to \pi$ and for phase masks with different pinhole diameters a: $a = 0.5$", $a = 1$", $a = 1.5$", $a = 2$" and different seeing conditions.

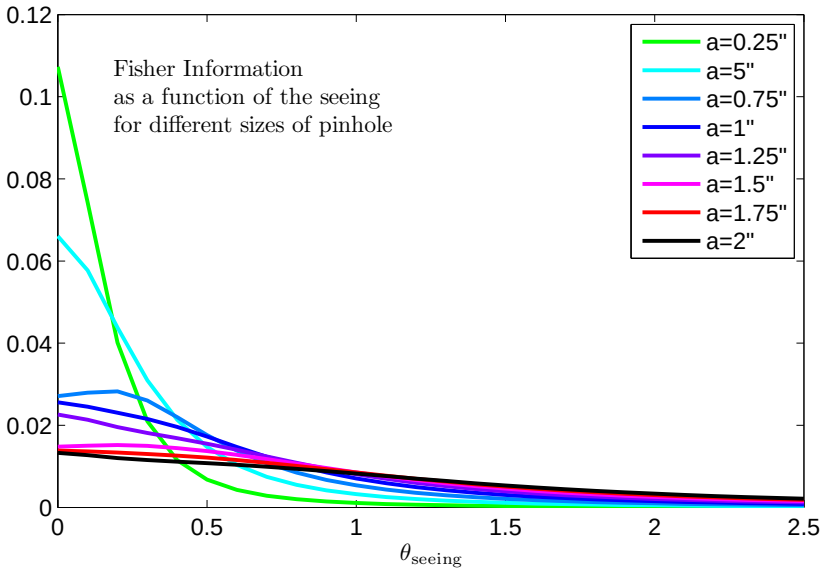

Figure 5.22: Fisher information for $\Delta\varphi \to \pi$ and for phase masks with different pinhole diameters a and different seeing conditions ranging from $\theta_{\text{seeing}} = 0$" to $\theta_{\text{seeing}} = 2.5$".

5.5.3 Measurement of a differential tilt

Assume that the complex amplitude over an interval $[-d, +d]$ is given by

$$U_1(x|\theta) = \frac{1}{\sqrt{2d}} e^{ik\varphi(x)} = \frac{1}{\sqrt{2d}} e^{ik\theta f(x)} \tag{5.75}$$

where $f(x)$ is an arbitrary real-valued function across the interval and θ is the coefficient, which has to be measured. Under the assumption that the average of $\varphi(x)$ across the interval is zero, the quantum statistical Fisher information is given by

$$I_{\text{F}} = 4k^2 \int_{-d}^{+d} \mathrm{d}x \frac{\partial}{\partial\theta} U_1^*(x|\theta) \mathrm{d}x \frac{\partial}{\partial\theta} U_1(x|\theta). \tag{5.76}$$

Introducing Eq. (5.75) into Eq. (5.76) gives the expression for the Fisher information

$$I_{\text{F}} = 4k^2 \frac{1}{2d} \int_{-d}^{+d} \mathrm{d}x f^2(x) = 4k^2 \sigma_f^2, \tag{5.77}$$

where σ_f is the RMS of $f(x)$ across the integration interval. The corresponding Cramér-Rao bound is then given by

$$\sigma_{\text{CRB}} = \frac{1}{I_{\text{F}}} = \frac{1}{2k\sigma_f} = \frac{\lambda}{4\pi\sigma_f}. \tag{5.78}$$

For a piston step of θ one has $\sigma_f = 1/2$ and therefore for the Cramér-Rao bound $\sigma_{\mathrm{CRB,piston}}$ as in [60]

$$\sigma_{\mathrm{CRB,piston}} = \frac{\lambda}{2\pi}. \tag{5.79}$$

For optical wavelengths of $\lambda \approx 600$ nm the fundamental precision limit for the measurement of a piston step with a single photon is therefore of the order of 100 nm. For the tilt

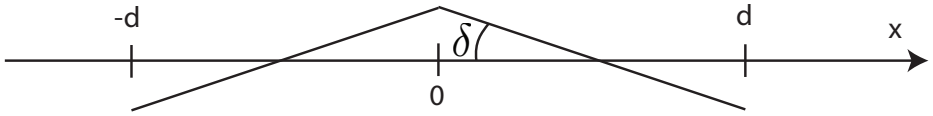

Figure 5.23: Differential tilt δ between two segments of length d.

shown in Fig. 5.23 with the unknown parameter $\theta = \delta$ representing the slope one obtains $\sigma_f = d/(2\sqrt{3})$ and therefore the Cramér-Rao bound $\sigma_{\mathrm{CRB,tilt}}$

$$\sigma_{\mathrm{CRB,tilt}} = \frac{\sqrt{3}}{2\pi}\frac{\lambda}{d}. \tag{5.80}$$

For a subaperture with a diameter of $2d = 120$ mm on the primary mirror, which is typically used for Shack-Hartmann measurements of piston steps, the precision limit for the measurement of relative tilts is then given by

$$\sigma_{\mathrm{CRB,tilt}} = \frac{\lambda}{2\pi}\frac{600\mathrm{nm}}{60\mathrm{mm}} \approx 2.8 \cdot 10^{-6} \equiv 0.58”. \tag{5.81}$$

Across a segment with a diameter of 1.5 m such a tilt of 0.58” around an axis through the center of the segment would be equivalent to piston steps at the border to adjacent non-tilted segments of approximately 2 μm. Fundamentally, slope errors can, with the chosen diameter of the subaperture, only be measured with a precision that is approximately 20 times smaller than the precision for piston measurements.

To compare these figures with data obtained with APE, the tilt errors have to be adapted to the size of the Active Segmented Mirror. With a scale factor of approximately 60 between the VLT primary mirror and the ASM, the fundamental precision limit for tilt measurements on the ASM is therefore of the order of 35”.

One can now compare the ratio of the precision obtained for piston and tilt measurements with the Zernike Phase Contrast Sensor. Comparing the Figures 5.24 and 5.25, showing the measured signals for different values for the piston steps and the tilts, respectively, one can estimate the limits for the visibilities for the effects of piston steps and tilts as 30 nm for a piston step and 6” for a tilt. For the piston steps there is a ratio of approximately 3 between the fundamental precision of 100 nm and the estimated limit of 30 nm for measurements with bright stars, which are, however, affected by various sources of noise. Applying the same ratio to the tilt measurements, one would expect a limit of $35”/3 \approx 12”$ for the limit for visibility limit. This is approximately 2 times larger than the measured visibility limit. The reason may be that in the case of the Zernike Phase

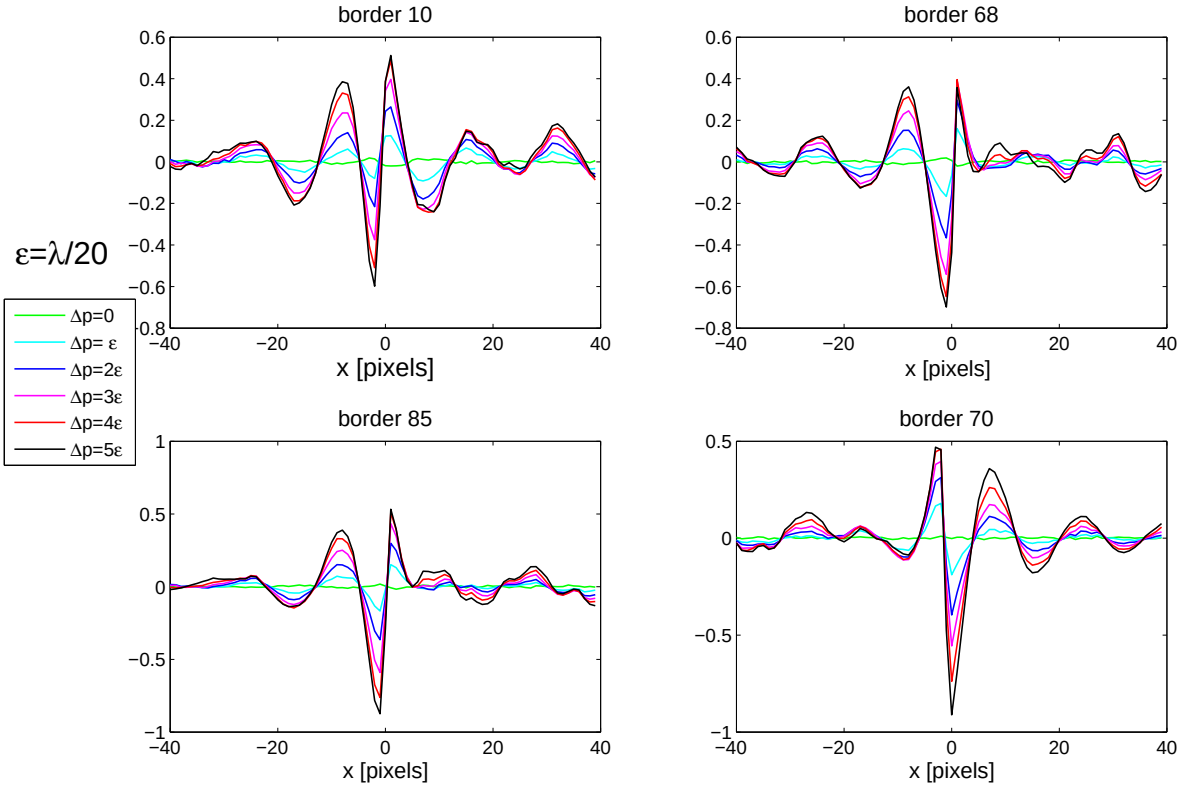

Figure 5.24: Signal of the Zernike Phase Contrast Sensor obtained for piston steps, Δp, from 0 to 5 ϵ, where $\epsilon = \lambda/20$ nm. The images have been acquired with the following parameters: $\lambda = 650$ nm, the phase mask has a diameter $a = 1$".

Contrast Sensor a much larger subaperture contributes to the signal than the 120 mm used in the calculation of the fundamental precision limit above. If this was true, the tilts could be measured by the Zernike Phase Contrast Sensor with a somewhat higher precision and consequently also with fewer photons than with the Shack-Hartmann sensor. However, a clarification of this point requires further measurements and analyses.

5.5.4 Optimal Optical Path Difference of the phase mask

The optimal phase shift ψ_0 introduced by the OPD δ_0 of the phase mask ($\psi_0 = k\delta_0$) has also been studied with the Fisher information. In the calculations, the diameter of the phase mask is $a = 1.5$" and the wavelength of the light is $\lambda = 650$ nm.

Figure 5.26 shows the Fisher information density for different values of the phase shift ψ_0, from $\psi_0 = 0$ to $\psi_0 = \pi$.

The corresponding Fisher Information is shown in the plot of Figure 5.27. The values obtained are perfectly symmetric around $\psi_0 = \pi/2$.

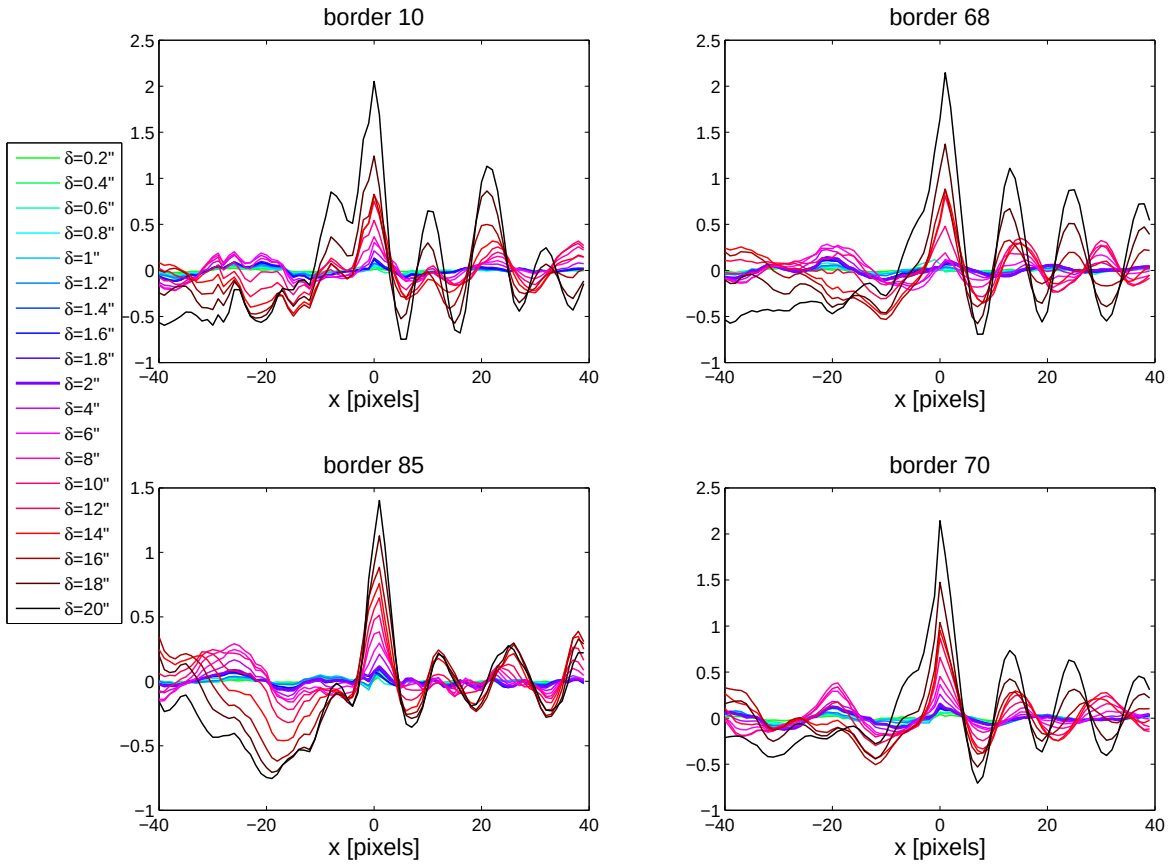

Figure 5.25: Signal of the Zernike Phase Contrast Sensor obtained for a differential tilt, δ, from 0.2" to 20". The images have been acquired with the following parameters: $\lambda = 650$ nm, the phase mask has a diameter $a = 1$".

As expected (see Section 5.4), the Fisher information is maximal for $\psi_0 = \pi/2$ and zero for $\psi_0 = 0$ and $\psi_0 = \pi$. This confirms our choice for the OPD $\delta_0 = \lambda/4$.

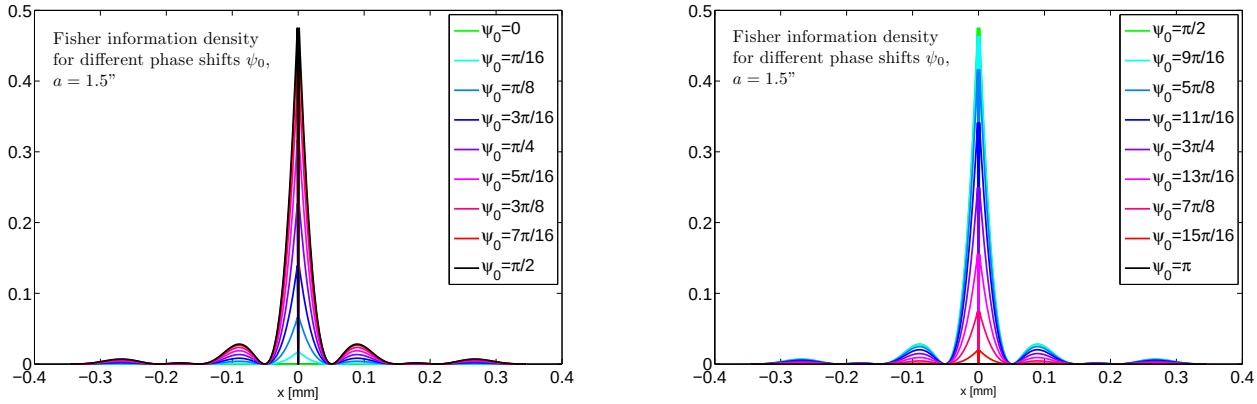

Figure 5.26: Fisher information density for different phase shifts introduced by the phase mask. Left: from $\psi_0 = 0$ to $\psi_0 = \pi/2$. Right: from $\psi_0 = \pi/2$ to $\psi_0 = \pi$.

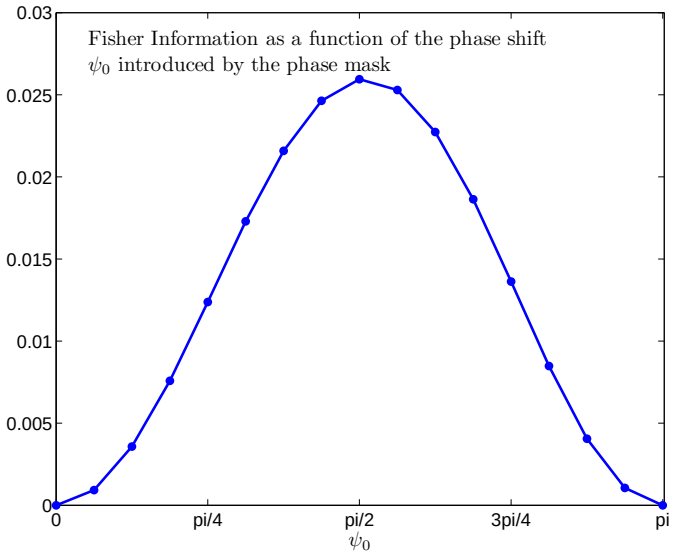

Figure 5.27: Fisher information as a function of the phase shift introduced by the phase mask, from $\psi_0 = 0$ to $\psi_0 = \pi$.

Chapter 6

Phasing algorithm

The methods and algorithms used to retrieve the piston, tip and tilt values from the raw images obtained with the Zernike Phase Contrast Sensor are discussed in this section. All the steps are listed in the order of their execution. The first step is the image normalization which has to be performed for every image. The second step is the localization of the border signals in the normalized image with a sufficient accuracy with a pupil registration algorithm. In the third step, the signals are extracted and analyzed with a fitting algorithm. Different methods to increase the capture range are also presented. Finally, in the last step, the piston, tip and tilt values of each individual segment are reconstructed with an inverted interaction matrix derived by a singular value decomposition (SVD).

The methods and algorithms presented in this Chapter have been developed by myself in the course of my thesis. A summary of this Chapter has been presented in Surdej et. al. [75].

6.1 Image Normalization

The goal of the image normalization procedure is to obtain a signal equivalent to $F(x)$ described by Eq. (5.30) where the values of $F(x)$ are all in the range $[-1, +1]$.

The signal image I^{S} is the CCD image of the intensity in the plane of the exit pupil of the sensor. An example of an image obtained on sky is shown in Figure 6.2.

If B_0 is the background in the CCD image, $\overline{I^{\mathrm{S}}} = I^{\mathrm{S}} - B_0$ corresponds to the intensity $S(x) = |U_2(x)|^2$ expressed by Eq. (5.26). The background B_0 is directly measured in the signal image I^{S} outside the image of the pupil.

Sufficiently far away from the borders of the segments, the intensity of the signal image is uniform. $\langle I^{\mathrm{S}} \rangle$ is defined as the mean value of the intensity of the image I^{S} calculated inside the segments (excluding areas affected by the spider and the obscuration by M2). With $\langle \overline{I^{\mathrm{S}}} \rangle = \langle I^{\mathrm{S}} \rangle - B_0$ corresponding to the intensity $|U_1(x)|^2$ defined in Section 5.2 one gets

$$\overline{I^{\mathrm{S}}} = \langle \overline{I^{\mathrm{S}}} \rangle \, (1 + F(x)). \tag{6.1}$$

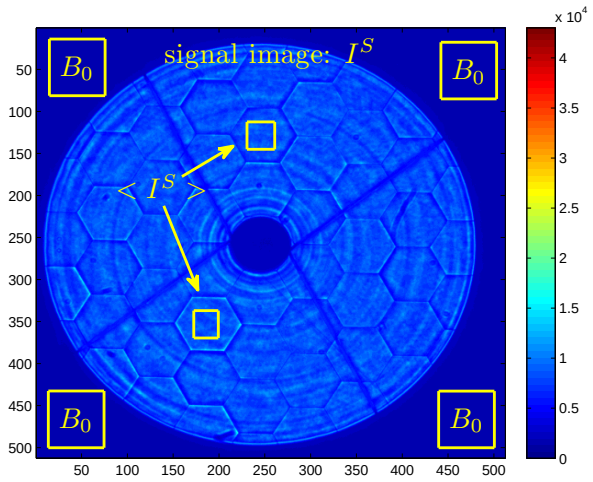

Figure 6.1: CCD image, or signal image I^{S}, obtained with the Zernike phasing sensor at the VLT with the following parameters: $\theta_{\mathrm{seeing}} \approx 0.55$", $a = 1$", $\delta_0 = 175$ nm, $\lambda = 650$ nm.

Solving Eq. (6.1) for $F(x)$ one obtains

$$F(x) = \frac{\overline{I^{\mathrm{S}}} - \langle \overline{I^{\mathrm{S}}} \rangle}{\langle \overline{I^{\mathrm{S}}} \rangle} = \frac{I^{\mathrm{S}} - \langle I^{\mathrm{S}} \rangle}{\langle I^{\mathrm{S}} \rangle - B_0}. \tag{6.2}$$

The value of a pixel (i, j) in the normalized signal image I^{N} is given by

$$I^{\mathrm{N}}_{ij} = \frac{I^{\mathrm{S}}_{ij} - \langle I^{\mathrm{S}} \rangle}{\langle I^{\mathrm{S}} \rangle - B_0}. \tag{6.3}$$

The internal metrology is used as a reference to quantify the precision of the piston, tip and tilt measurements performed by the different phasing sensors. The piston, tip and tilt values of each individual ASM segment are measured by the Internal Metrology (IM) in an area located inside each segment. For the correction however, they are deduced from measurements with the phasing sensor performed in areas located at the inter-segment borders. Since the optical surface quality of the ASM segments is of the order of 25 nm peak to valley (PtV), the measurements of the phasing sensor differ from the measurements of the IM as illustrated in Fig. 6.4 where, as an example, the phasing sensor measures a piston step of 25 nm surface and the IM measures identical piston values for the segments 1 and 2.

One solution to eliminate this inconsistency is to subtract from I^{S} the image acquired with the phasing sensor when, according to the IM, the ASM is in the flat configuration called I^{ref}, instead of subtracting the constant value $\langle I^{\mathrm{S}} \rangle$. This image must be acquired with the same optical filter and the same phase mask as the signal image I^{S}. The normalized

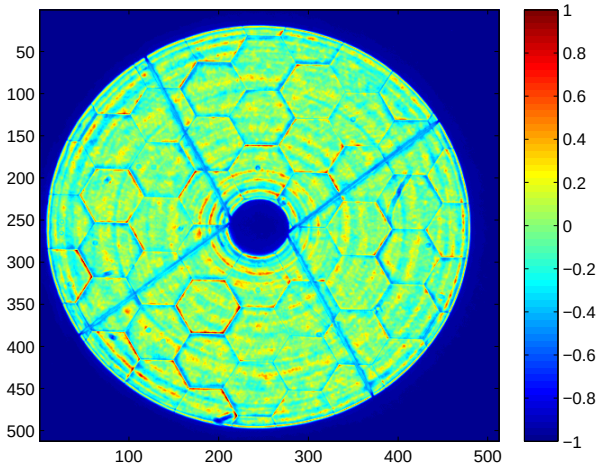

Figure 6.2: CCD image (of Figure 6.2) normalized using Eq. (6.3).

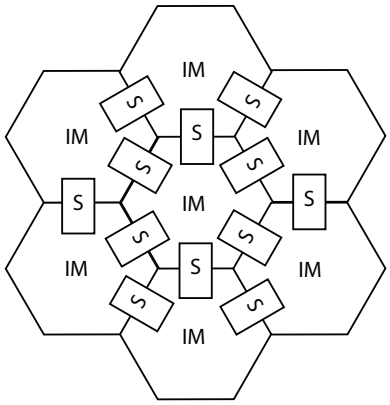

Figure 6.3: The definition of a *flat* mirror is different for the IM and for the PWFS because the phase is measured at different locations. The IM measures the piston, tip and tilt in an area located inside the segment. The phasing sensor (S) measures the piston, tip and tilt information in an area located at the inter-segment edges.

pixel values can now be expressed as

$$I_{ij}^{\mathrm{N}} = \frac{I_{ij}^{\mathrm{S}} - I_{ij}^{\mathrm{ref}}}{\langle I^{\mathrm{S}} \rangle - B_0}. \tag{6.4}$$

Figure 6.5 shows the normalization of the CCD image shown in Figure 6.2 obtained using Eq. (6.4).

For most measurements, the use of Eq. (6.4) is preferred since the IM is the reference for the performance of the phasing sensor. However, Eq. (6.3) can also be used if the goal

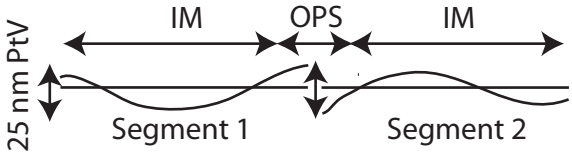

Figure 6.4: Difference between IM measurements and optical phasing sensor measurements. The IM measures the mean phase of the wavefront inside the segment and the optical phasing sensor measures the phase at the inter-segment edges. If the segments are not ideally flat, the IM and the optical phasing sensor measure two different quantities.

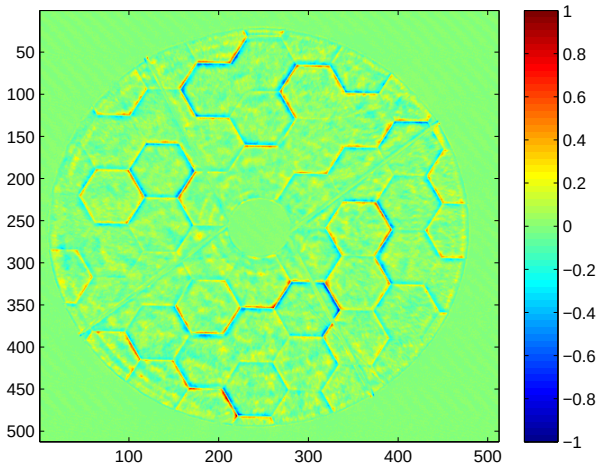

Figure 6.5: CCD image (of Figure 6.2) normalized using Eq. (6.4).

of the measurement is to phase the segmented mirror without the use of any calibration.

6.2 Pupil registration

The misalignments of the segments produce intensity variations on a CCD detector that correspond to the locations of the segment edges. The positions of the segment edges on a CCD image must first be determined with an accuracy of the order of one pixel to localize the signals, which can then be analyzed in a second phase with a robust signal analysis algorithm.

A pupil registration algorithm to retrieve the locations of the edges has been developed by Surdej et al. [74] and is presented here. Another method, which is based on the use of the Hough transform, has also been studied by Surdej et al. [73].

The pupil registration algorithm consists of three main steps. First, the orientation of the hexagonal pattern is measured, using measurements of the directions of the gradients

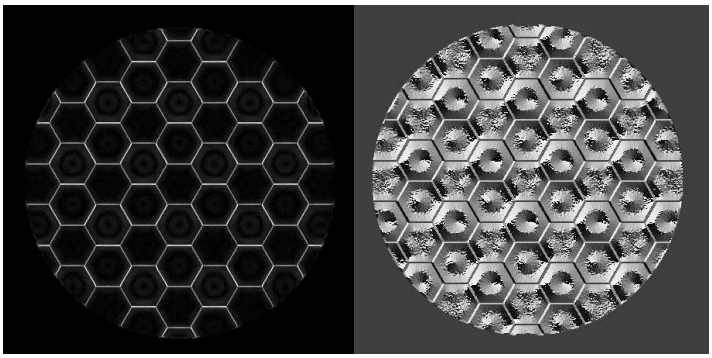

(a) (b)

Figure 6.6: (*a*) Modulus of the gradient ($\sqrt{G_x^2 + G_y^2}$) (*b*) Gradient direction γ, each pixel value corresponding to an angle in the range $[0, 2\pi]$.

in the image. Once the orientation is determined, the hexagon size can be measured using a projection of the image onto lines perpendicular to the edges. Finally, the position of the centers of the hexagons are calculated as the intersection of three lines.

The algorithm has to be able to cope with small piston errors and, if it is used during observations, also with a small number of photons.

6.2.1 Detection of the orientation

The one-dimensional signals generated by the Zernike Phase Contrast Sensor in the case of piston steps are given by luminosity variations with gradients perpendicular to the edges of the hexagonal pattern.

If G_x and G_y are the gradient images of the signal image, in the x and y directions, respectively, the value of the amplitude of the local gradient, $G(i, j)$, of pixel (i, j), is given by

$$G(i, j) = \sqrt{G_x^2(i, j) + G_y^2(i, j)} \tag{6.5}$$

where $G_x(i, j)$ and $G_y(i, j)$ are the values of the gradients at the location of the pixel (i, j) in the x and y directions, respectively. The direction $\gamma(i, j)$ of the local gradients, for the pixel (i, j), is simply given by

$$\gamma(i, j) = \arctan \frac{G_y(i, j)}{G_x(i, j)}. \tag{6.6}$$

Images of the amplitude of the gradient and of the associated angle are shown in Fig. 6.6.

Measuring the amplitudes of the local gradients $G(i, j)$ and their associated angles $\gamma(i, j)$ with $\gamma \in [0, 2\pi[$, the dominant orientation of the gradients $\overline{\gamma}$ of the image can be

calculated with the following standard algorithm :

$$z = \left(\sum_i \sum_j G(i,j) \cdot e^{i\gamma(i,j)\cdot p} \right) \tag{6.7}$$

$$\overline{\gamma} = \frac{1}{p} \cdot \arctan\left(\frac{\Im(z)}{\Re(z)} \right) \tag{6.8}$$

where p stands for a periodic factor in the orientation. With a hexagonal tessellation this periodic factor is equal to 6. It makes the contributions of all angles $\alpha + (k-1)\pi/3$, $k = 1, \ldots, 3$ identical. However, it does not make sense to compute a mean angle in the range $[0 \ldots 2\pi[$. The final division by p scales the angle back to the range $[0 \ldots \frac{2\pi}{p}[= [0 \ldots \frac{\pi}{3}[$.

The mean angle $\overline{\gamma}$ corresponds to the direction of the gradient, perpendicular to the segment edges along the three directions $\alpha_k = \overline{\gamma} + (k-1)\pi/3$, $k = 1, 2, 3$.

6.2.2 Measurement of the hexagon size

The first step of this analysis is to project the modulus of the original image onto the lines of directions α_k $(k = 1, 2, 3)$, shown in Figure 6.7. The projection is weighted by the term $\sin^{2n}(\alpha_k - \gamma_{ij})$. This gives more weight to those edges where the gradients are perpendicular to the projection direction. The constant n can be any number; $n = 3$ has been found to be a good choice.

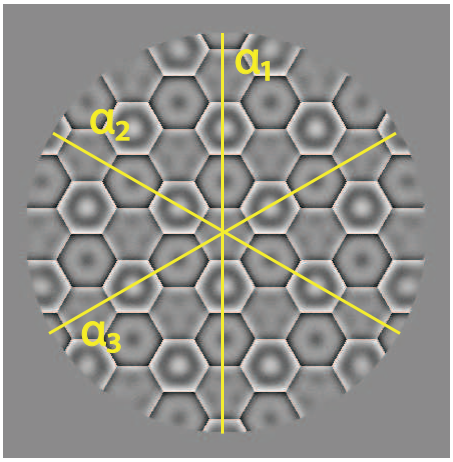

Figure 6.7: Definition of the three lines of direction α_k, $k = 1, 2.3$, perpendicular to the edges of the segments.

The result of this projection onto one line is shown in the upper graph of Figure 6.8. The distance between the evenly spaced peaks corresponds to half of the flat to flat distance of the hexagon. A measurement of the peak positions and the mean distance between them leads to a good approximation for the hexagon size.

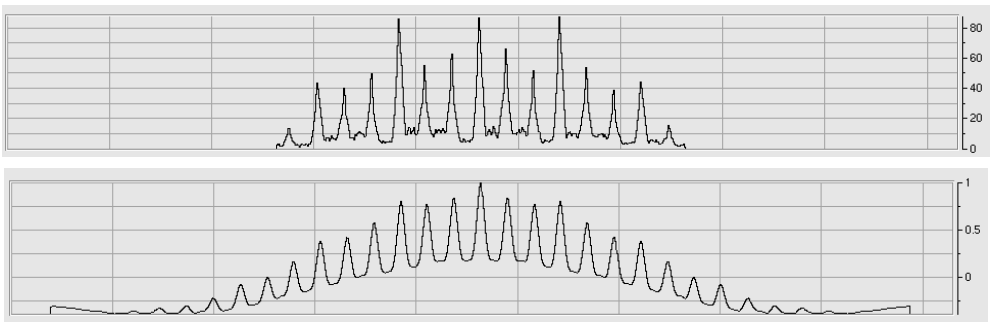

Figure 6.8: Top: Projection along one of the three directions of the lines previously calculated. Bottom: Normalized auto-correlation of the projection.

In order to improve this estimate, the normalized auto-correlation of the projection is calculated [41]:

$$c(k,l) = \frac{\sum_s \sum_t [f(s,t) - \overline{f}(s,t)][f(k+s,l+t) - \overline{f}(k+s,l+t)]}{\sqrt{\sum_s \sum_t [f(s,t) - \overline{f}(s,t)]^2 \sum_s \sum_t [f(k+s,l+t) - \overline{f}(k+s,l+t)]^2}} \tag{6.9}$$

where f represents the image and $\overline{f}(s,t)$ is the mean of f in a region around the pixel with coordinates (s,t). This normalized auto-correlation, lies in the range between -1 and 1 and is independent of scale changes in the amplitude of f.

The form of the normalized auto-correlation still contains equally spaced peaks. The center is given by the position of the highest peak with a value of 1.

The average of the mean distances between these peaks over all three directions is the final estimate of the size of the hexagon.

6.2.3 Estimate of the position of the center

From the positions of the peaks in the projections, one can calculate the position of the intersegment edges in the image. Then, knowing the orientation angles and the size of the hexagons, the lines that run along the intersegment edges can be constructed. Ideally, lines along three different directions intersect in the centers of the hexagons. The estimate for the centers of the hexagons including the center of the whole pattern can then be obtained from a best fit of the expected hexagonal pattern to the intersections of the lines.

6.2.4 Results

The paper by Surdej et al. [74] contains a discussion of the performance of the pattern recognition algorithm as a function of the number of photons, the amplitude of the segment misalignments and their distribution. The accuracy achieved under conditions similar to the ones expected during observations is also discussed. For a sufficiently large number of

photons and large piston heights, the RMS of the estimation error of the orientation angle is smaller than 0.1 degree, the one of the hexagon size is smaller than 0.1 pixel and the one of the coordinates of the center is smaller than 1 pixel.

6.3 Extraction of the signal

After the pupil registration algorithm, which enables the localization of the edges, the signals are extracted from a two dimensional window centered on the hexagon border, as shown in Fig. 6.9*a*. The projections of the measured profiles onto the axis perpendicular to the edge are similar to the expected theoretical profile described by Eq. (5.30) (see Fig. 6.10).

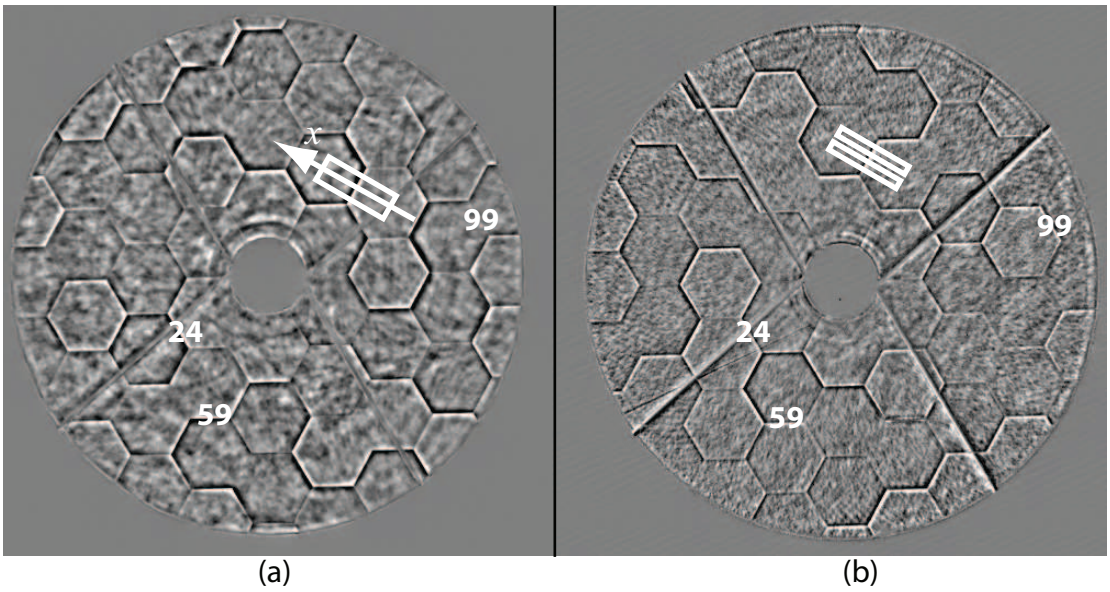

Figure 6.9: Normalized images acquired on sky with a filter centered on the 650 nm wavelength and with a bandwidth of 100 nm. The seeing conditions were around 0.5" (a) and 1.2" (b). The phase mask of 1" diameter has been used in (a) and of 1.5" diameter in (b). The subaperture centered on a segment edge is used to extract the signal of that edge. The two subapertures centered on one border shown in (b) are used to retrieve, in addition, the relative tip-tilt between the segments.

6.4 Fitting algorithm

The theoretically expected signal of Eq. (5.30) can be expressed as a function of the piston step and a few other nuisance parameters, which affect the signal but do not alter the information on the piston step. A theoretically derived function with a few free parameters

is fitted in the least squares sense to the measured intensity profiles perpendicular to the segment edges.

Expressing the theoretical equation of the signal (Eq. (5.30)) as a function of the fitted parameters results in the following formula:

$$F(x) = a_3 + a_4(x - a_5) + [1 - f(u)]\{a_1 \text{sign}(x - a_5)\sin(\psi_0) - (1 - a_2)f(u)(1 - \cos(\psi_0))\} \quad (6.10)$$

where $u = a_6|x - a_5|$. a_i, $(i = 1 \dots 6)$, are six free fitting parameters. The first term a_3 represents a constant background, the second term a constant slope in the signal, a_5 represents the shift of the signal with respect to the origin and a_6 determines the signal width.
$f(u)$, (Eq. (3.25)), is the normalized sinc integral for the sharp edge mask (round pinhole):

$$f(u) = \frac{2}{\pi}\text{Si}(u) = \frac{2}{\pi}\int_0^u \frac{\sin(t)}{t}\text{d}t, \quad (6.11)$$

and for the gaussian pinhole (or in the presence of atmospheric turbulence) $f(u)$ is given by the Gaussian error function (Eq. (3.24)):

$$f(u) = \Phi(u) = \frac{2a_6}{\sqrt{\pi}}\int_0^u \exp(-t^2)\text{d}t. \quad (6.12)$$

In the presence of atmospheric turbulence, a simplified model of the signal, as presented in Section 5.4.5, is used.

The piston step information is contained in the two parameters, a_1 and a_2, which are proportional to the sine and cosine of the phase $\Delta\varphi$, respectively,

$$\begin{cases} a_1 = C_1 \sin(\Delta\varphi) \\ a_2 = C_2 \cos(\Delta\varphi) \end{cases}. \quad (6.13)$$

Under ideal conditions, C_1 and C_2 are equal to 1, as described by Eq. (5.30). However, in the presence of noise such as atmospheric disturbances or polishing errors the values of C_1 and C_2 are modified and are smaller than 1, as explained in [86]. In the fitting, it is assumed that a_1 and a_2 are two independent parameters.

The equations (6.13) are called calibration curves.

Only the information contained in the anti-symmetric term, given by the fitting parameter a_1 is used for the determination of the piston step:

$$\Delta p = \frac{\lambda}{2\pi}\arcsin\left(\frac{a_1}{C_1}\right). \quad (6.14)$$

The values of the piston step deduced from the fitting parameter a_2 are, in the presence of atmospheric turbulence, not accurate, as will be shown by the experimental results presented in the sections 7 and 8.

The capture range is limited to $\pm\lambda/4$. The availability of the cosine term represented by a_2 would have increased the capture range of the sensor to $\pm\lambda/2$.

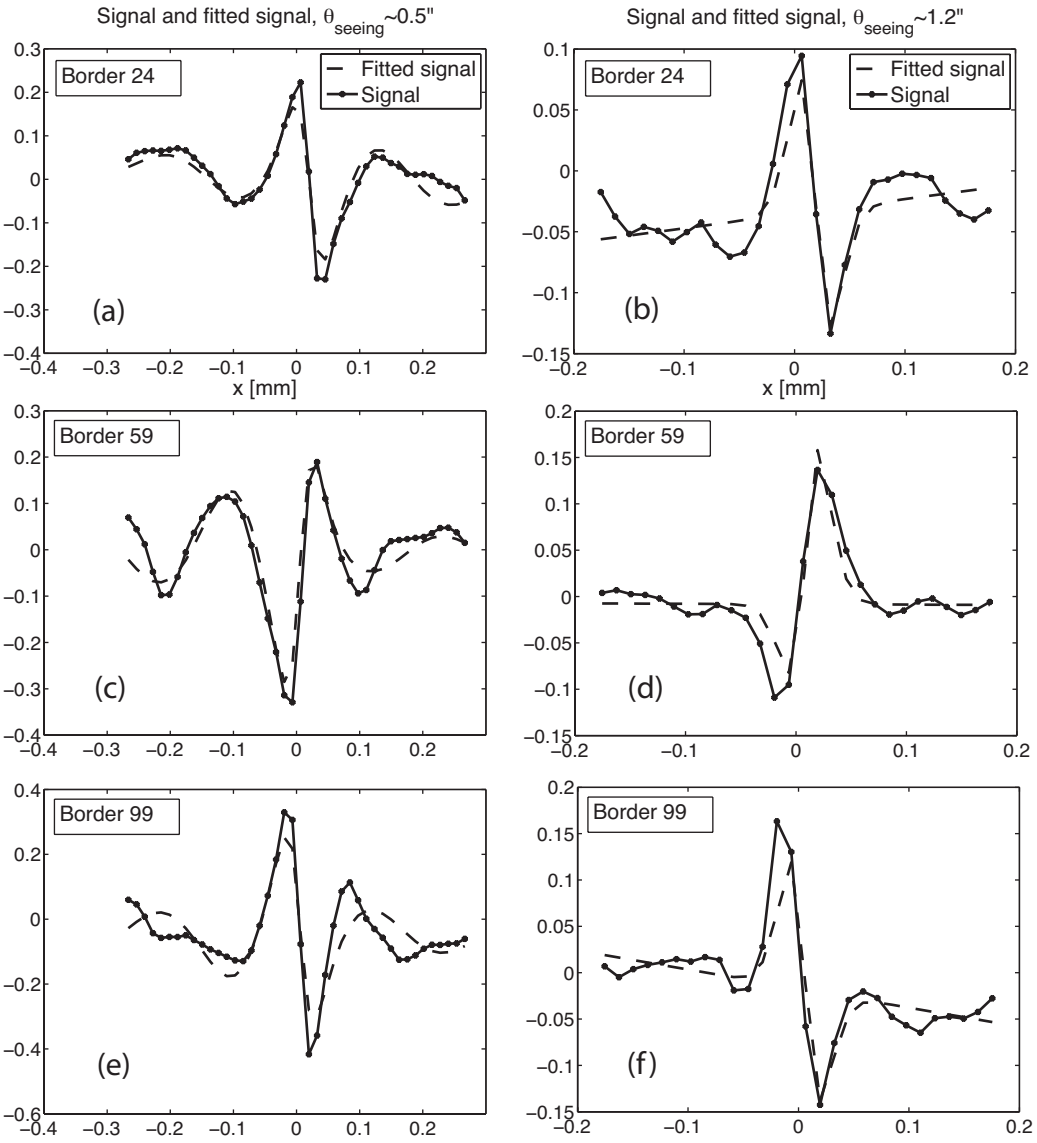

Figure 6.10: Each of the following three sets contains the identification number of the border, the real piston step value, and the two measured piston steps obtained from the data in Fig. 6.9(a) and Fig. 6.9(b). (24, -65.4 nm, (a) -39.8 nm, (b) -74.9 nm) (59, 60.5 nm, (c) 54.8 nm, (d) 91.9 nm) (99, -80 nm, (e) -66.4 nm, (f) -98.3 nm).

Fitted signal profiles for different borders from images acquired on sky are shown in Fig. 6.10. The signal profiles in the plots (a), (c) and (e), which are extracted from Fig. 6.9(a) ($\theta_{\text{seeing}} \approx 0.5$"), are fitted using the sharp-edge phase mask expression. Plots (b), (d) and (f), extracted from Fig. 6.9(b) with $\theta_{\text{seeing}} \approx 1.2$" are fitted using the apodized-edge phase mask expression. The side lobes of the theoretical signal are smoothed in the presence of stronger turbulence.

6.5 Capture range

When measuring at a single wavelength λ, the range of non-ambiguity for the Zernike Phase Contrast Sensor is given by $\pm\lambda/4$.

Two methods can be used to enlarge the capture range of a phasing sensor:

- the multiple wavelength method: the ambiguity on the measurements can be removed by repeating the same measurement at a different wavelength.
- the coherence method: a filter, centered on the wavelength λ and with a bandwidth $\Delta\lambda$ has a finite coherence length. The usage of this property, the coherence, results in a large increase of the capture range.

6.5.1 Multiple wavelength method

With the use of two wavelengths, the range of non-ambiguity for the step heights can be increased to $\Lambda/2$ where Λ is the synthetic wavelength defined as

$$\Lambda = \frac{\lambda_1 \lambda_2}{|\lambda_1 - \lambda_2|} \tag{6.15}$$

with λ_1 and λ_2 denoting the two individual wavelengths.

Löfdahl and Eriksson [46] describe a procedure which allows to increase the capture range above the synthetic wavelength when the two wavelengths are chosen appropriately and when the absolute error on the piston steps is small. This technique has also been used by Schumacher et al. [72]. A different approach, called the two wavelengths closed loop technique, has been proposed by Esposito et al. [25]. The technique has been successfully tested at the William Herschel Telescope in 2006 [64] and in the framework of the Active Phasing Experiment together with two very innovative techniques: the wavelength sweep technique and the segment sweep technique, which are also described in [64]. The wavelength sweep technique has been successfully tested in the laboratory with the Active Phasing Experiment with a commercial tunable filter [4].

Finally, Vigan et al. [79, 78] have implemented, for the Zernike Phase Contrast Sensor, a new algorithm based on the two wavelengths closed loop technique. The technique has been successfully tested on sky in the framework of the Active Phasing Experiment [79, 78].

6.5.2 Coherence method

Another method, called the broadband phasing algorithm, to increase the capture range has been implemented by Chanan et al. for the phasing of the Keck telescopes [12]. It exploits the finite spread in the wavelength of the light. For a filter with a finite bandpass $\Delta\lambda$ centered on the wavelength λ, a signal can be detected as long as the piston step is not larger than the coherence length $l_c = \lambda^2/\Delta\lambda$ of the optical filter. This method has also been successfully tested in the framework of the Active Phasing Experiment by Gonté et al. [39] with the Shack-Hartmann phasing sensor (SHAPS).

This efficient method, to which we refer to as the coherence method, has also been tested with the Zernike Phase Contrast Sensor in the laboratory. The results are presented in Section 7.2.

6.6 Tip-tilt algorithm

The tip-tilt is a rotation of the segment about two horizontal axes.

Three particular cases, shown in Figure 6.11, are considered. The configuration shown in Figure 6.11(a) produces a signal similar to a piston error. In the second case, (b), the tip-tilts of the segments produce a change of the phase step along the inter-segment border. The third case (c), is a differential tilt between the segments. The signal is constant along the edge and symmetric with respect to the border.

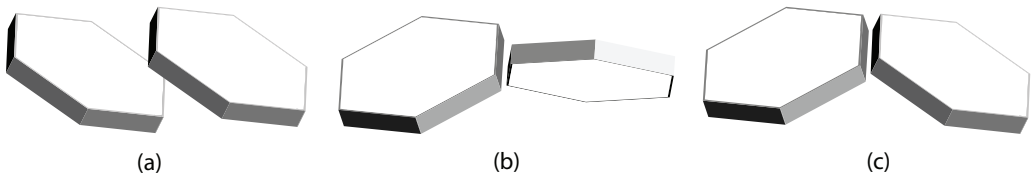

Figure 6.11: Three different tip-tilt configurations. (a) The tip-tilt of the segments produces only locally a differential piston, constant along the edge. (b) The tip-tilt of the segments produces only locally a differential piston, varying along the edge. (c) The tip-tilt produces locally only differential tilt, constant along the edge.

Therefore, instead of using one subaperture (Fig. 6.9(a)) which is sufficient for the evaluation of the piston, two subapertures (Fig. 6.9(b)) are used to extract, in addition, the relative tilt between the two segments around an axis perpendicular to the border and parallel to the surface [15].

Since the tip-tilt of the segments is deduced from the differential piston, the capture range for the determination of the tip-tilt is related to the capture range for the measurement of the individual phase steps.

The details of the relationship between the tips, the tilts and the phase steps along the borders are omitted in this manuscript and can be found in the publications by Chanan et al. [8] and Chueca et al. [15].

6.7 Singular value decomposition

The last step of the phasing algorithm consists of converting the differential pistons along each border to segment pistons, tips and tilts with the help of an inverted interaction matrix derived by Singular Value Decomposition (SVD).

6.7.1 Short introduction to SVD

Each segment piston is determined from up to six piston step measurements. This can be expressed mathematically by a system of linear equations with M equations, where M is the number of edges, and N unknowns, where N is the number of segments:

$$\begin{aligned} p_j - p_k &= \Delta p_i \\ i &= 1, \ldots, M \\ j, k &= 1, \ldots, N \end{aligned} \tag{6.16}$$

where p_j and p_k are the piston values of two adjacent segments j and k corresponding to sensor i and Δp_i is the measured piston step.

A signal vector $\mathbf{u} = \{\Delta p_1, \ldots, \Delta p_i, \ldots, \Delta p_M\}$ is related to an actuator vector $\mathbf{v} = \{p_1, \ldots, p_i, \ldots, p_N\}$ by the linear mapping represented as the two dimensional matrix $\mathbf{A}$ [59, 8]:

$$\mathbf{A}\mathbf{v} = \mathbf{u}. \tag{6.17}$$

The matrix $\mathbf{A}$ maps the N-dimensional actuator space $\mathcal{P}$ into a M-dimensional signal space $\mathcal{S}$. The image space $\mathcal{Q}$ is therefore a N-dimensional sub-space of $\mathcal{S}$. The SVD finds the unique orthonormal basis vectors $\{\mathbf{p}_i, i = 1, \ldots, N\}$ for the actuator space and $\{\mathbf{s}_i, i = 1 \ldots, N\}$ for the signal space, such that a basis vector $\mathbf{p}_i$ is mapped onto a basis vector $\mathbf{s}_i$:

$$\mathbf{A}\mathbf{p}_i = \sigma_i \mathbf{s}_i. \tag{6.18}$$

In other words, well distinguishable basis vectors in the actuator space $\mathcal{P}$ are mapped onto well distinguishable basis vectors in the signal space $\mathcal{Q}$.

The factors σ_i are called the singular values. They describe the sensitivity of the system to piston errors in the mode described by the vector $\mathbf{v}_i$.

Technically, the SVD factorizes the matrix $\mathbf{A}$:

$$\mathbf{A} = \mathbf{S}\mathbf{\Sigma}\mathbf{P}^T \tag{6.19}$$

where

- $\mathbf{S}$ is a matrix of dimension $M \times N$ containing the N basis vector $\mathbf{s}_i$.
- $\mathbf{\Sigma}$ is a square diagonal matrix of dimension $N \times N$ which contains the N singular values σ_j.
- $\mathbf{P}^T$ is a square matrix of dimension $N \times N$ containing the N basis vector $\mathbf{p}_i$.

Solving Eq. (6.17) for the unknown vector $\mathbf{v}$ requires the pseudo-inverse $\mathbf{B}$ of $\mathbf{A}$.

The pseudo-inverse $\mathbf{B}$ of the matrix $\mathbf{A}$ maps vectors only from the image space $\mathcal{Q}$, which describes all possible signals which can be generated by actuator movements, to $\mathcal{P}$. Therefore, applying $\mathbf{B}$ to a signal vector, the signal vector is first projected onto the space $\mathcal{Q}$, eliminating all signals that cannot be generated by actuator movements. A correction

based on the actuator commands calculated by applying $\mathbf{B}$ on a signal vector, therefore corrects perfectly the errors created by segment misalignments and is, in a least squares sense, the best possible correction of the signal vector.

The control matrix $\mathbf{B}$, is defined as

$$\mathbf{B} = \mathbf{P}\boldsymbol{\Sigma}^{-1}\mathbf{S}^T. \tag{6.20}$$

The diagonal matrix $\boldsymbol{\Sigma}^{-1}$ consists of the values σ_j^{-1}. If a value σ_j is zero, its inverse σ_j^{-1} in the matrix $\boldsymbol{\Sigma}^{-1}$ is set to zero.

To exclude the least sensed modes with zero or very small singular values, the corresponding σ_j^{-1} in the SVD are simply replaced by zero. The threshold depends on the amount of noise in the system, since σ_j^{-1} determines the noise propagation from the signal space into the actuator space [88].

6.7.2 Modes of the ASM in the case of pure piston error

The ASM is a segmented mirror with 61 segments and 156 edges. Six outer segments of the ASM are hidden by the pupil of the primary mirror of the VLT while the central segment is obstructed by the secondary mirror. Therefore, these 7 segments are not controlled[1]. The corresponding 24 edges are also ignored in the analysis[2]. The dimensions of the interaction matrix $\mathbf{A}$ are therefore $N = 61 - 7 = 54$ and $M = 156 - 24 = 132$.

The singular values of the interaction matrix are shown in Figure 6.12. A small σ_i

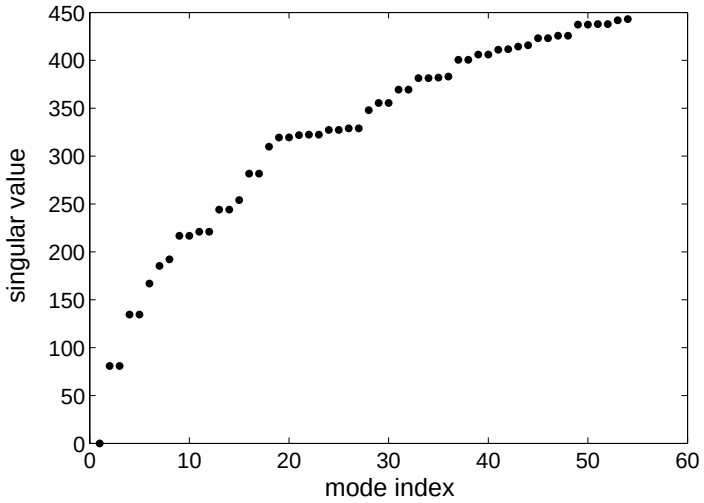

Figure 6.12: Singular values of the ASM for pure piston error.

expresses the fact that segment displacements in this mode i only generate small sensors

[1]The 7 ignored segments are the following: $\{0, 37, 41, 45, 49, 53, 57\}$. APE indexation is shown in A.1.

[2]edges ignored: $\{152, 151, 148, 147, 144, 143, 139, 140, 136, 135, 155, 132, 125, 118, 111, 104, 97, 90, 0, 1, 2, 3, 4, 5\}$

signals. This is the case for the smooth modes like the modes shown in Figure 6.13. The low order modes are similar to the classical optical aberrations such as global piston, global tip, global tilt, defocus, astigmatism, coma, etc. On the other hand, the modes with higher spatial frequencies, like the ones shown in Figure 6.14, have large singular values.

If only the segment piston errors are controlled the number of eigenmodes is M-1 since the rigid body motion (global piston) of the segmented mirror as a whole has no effect at the segment edges. It corresponds to the first mode with a singular value $\sigma = 0$. Modes 2 and 3 have identical singular values and correspond to tip and tilt of the ASM.

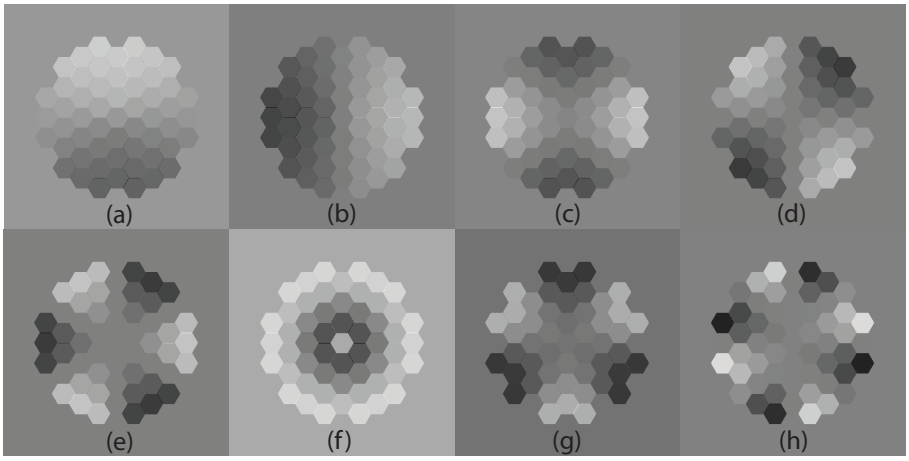

Figure 6.13: Modes 2 to 9 of the ASM.

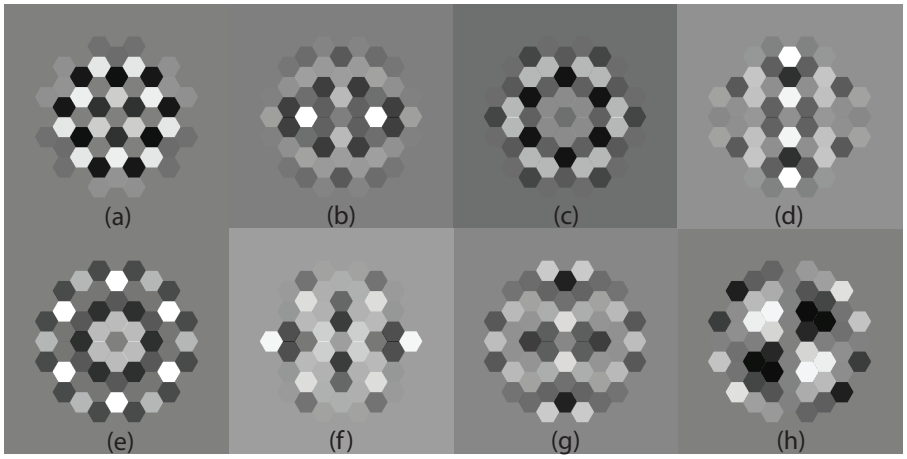

Figure 6.14: (a) Mode 54, (b) Mode 46, (c) Mode 43, (d) Mode 39, (e) Mode 36, (f) Mode 32, (g) Mode 29, and (h) Mode 16 of the ASM.

Chapter 7

Experimental results in the Laboratory

The results presented in this chapter are from images acquired in the laboratory with the following configuration: $a = 1$", $\psi_0 = \lambda/3.7$, and $\lambda = 650$ nm. When the turbulence generator is used, it is configured to simulate a seeing of $\theta_{\text{seeing}} = 0.65$".

All the presented results are given in nanometer, measured on the wavefront, and not on the surface.

7.1 Calibration curves

The fitted parameters a_1 and a_2, defined in Section 6.4, can be plotted for each border as a function of the piston step Δp.

Calibration curves, in the absence and in the presence of atmospheric disturbances are first presented. The effect of a misalignment of the phase mask on the calibration curves is then shown and requirements on the alignment of the phase mask are deduced.

7.1.1 Calibration curves in the absence and in the presence of atmospheric disturbances

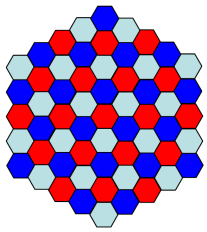

Figure 7.1: Three families of segments.

There are three families of segments on the segmented mirror with no borders in common. The three families are shown in Figure 7.1 in three different colors.

A set of 21 images has been acquired by moving a family of segments in piston from $-\lambda/2$ to $+\lambda/2$ (measured at the wavefront) with steps of $\lambda/20$. For each acquired image, the fitting parameters a_1 and a_2 are calculated for all the borders. The procedure has been performed both with and without the turbulence generator. The calibration curves are plotted in Figure 7.2 for 8 different borders. These curves are compared with the theoretical sine curve for a_1 and cosine curve for a_2, shown as the dashed lines in the plots.

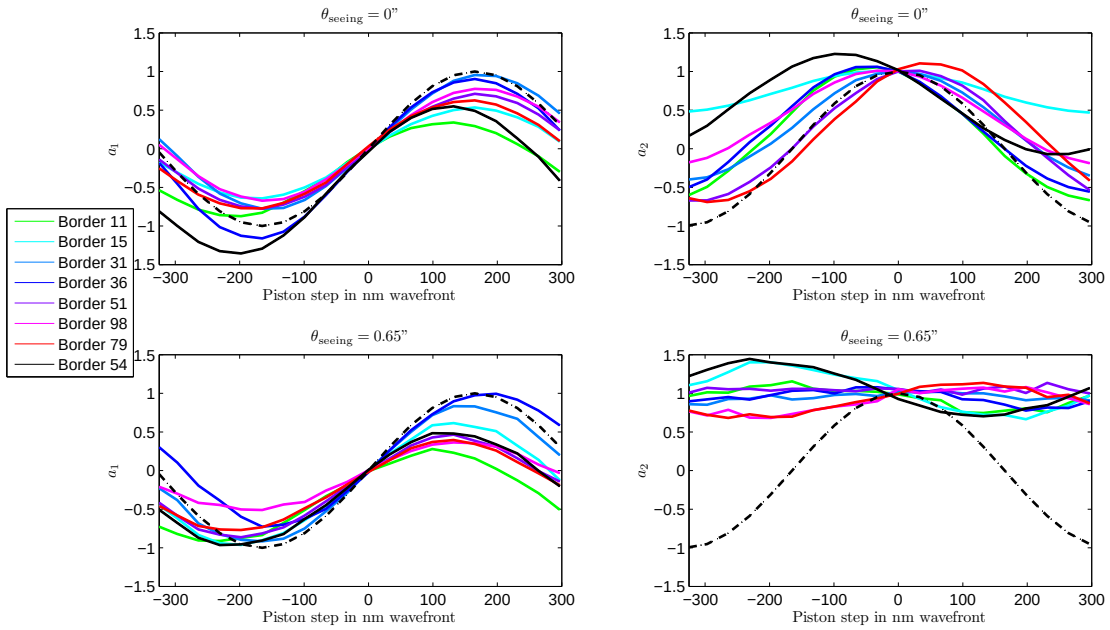

Figure 7.2: a_1 (left column) and a_2 (right column) calibration curves for different borders, without (top row) and with atmospheric turbulence with $\theta_{\text{seeing}} = 0.65$" (bottom row).

The curves of the parameter a_1 are well defined, irrespective of aberrations introduced by atmospheric turbulence, whereas the curves for the parameter a_2 acquired with the turbulence generator are noisy and cannot be used for the determination of the piston step.

For some of the edges and a piston step $\Delta p = \lambda/4$, the signals and the associated fitted signals, obtained without and with atmospheric turbulence, are shown in Figure 7.3. The signals shown in the left column were obtained without and the ones in the right column with atmospheric turbulence. The values of the fitted parameters a_1 and a_2 are also indicated in the plots. The plots in the same row correspond to the same border.

All obtained signals are strongly affected by the atmospheric disturbances. First, the amplitude of the signals and of the side lobes is reduced (note that the scale in both Figures is different). The theoretical predictions described in Section 5.4.3 seem to be consistent with the data obtained in the laboratory. The amplitude of the central peak

of the symmetric term, which is amplified in the presence of the atmosphere, strongly affects the fitting of the signal. This is illustrated with the peak drawn in the second row of Figure 7.3. The superposition of the two signals and the suppression of the side lobes generates a signal, on the right, which looks anti-symmetric. This new peak is interpreted by the fitting algorithm as the positive peak of the anti-symmetrical signal. In Figure 5.15, the amplitude of the peak of the symmetric term is plotted as a function of the seeing for different diameters of the phase mask. For $a = 1$" and $\theta_{\text{seeing}} = 0.65$", the amplitude of the peak is about 0.35, which is in agreement with the amplitudes observed in the plots in Figure 7.3. The fitting parameter a_2 can therefore not be used for the measurements of the piston step, in the presence of atmospheric turbulence, at least with the current signal analysis algorithm. The influence of atmospheric turbulence on the symmetric term should be taken into account in the model used for the fitting of the signal, which is given by Eq. (6.10).

All calibration curves, in Fig. 7.2, show two main discrepancies with respect to the theoretical sine and cosine curves:

- a vertical offset of the calibration curves,
- a change in the scale of the calibration curves.

These discrepancies can be modeled with a modification of Equations 6.13:

$$a_1 = A\sin(\Delta\varphi + \delta_1) - A\sin(\delta_1) \tag{7.1}$$
$$a_2 = C\cos(\Delta\varphi + \delta_2) - C\cos(\delta_2) + C \tag{7.2}$$

where δ_1 and δ_2 represent offsets of the calibration curves, and A and C represent the changes in scale.

A misalignment of the system, that is a shift of the phase mask with respect to the central peak of the point spread function, generates a shift of the calibration curves. This effect is analyzed in Section 7.1.2.

In the presence of atmospheric disturbances, the amplitude of the signal decreases. This is expressed through the parameters A and C (A and C are smaller than 1). For the parameter a_1 the ratio of the mean value of A with turbulence ($\theta_{\text{seeing}} = 0.65$") to A without turbulence is given by

$$\chi = \frac{\overline{A}|_{\theta_{\text{seeing}}=0.65"}}{\overline{A}|_{\theta_{\text{seeing}}=0"}} = 0.88. \tag{7.3}$$

More generally, a simple visual inspection of Figure 7.2 shows that each edge has its own calibration curve. Indeed, all the segments have different optical properties such as different inter-segment gaps, different segment aberrations, different edge profiles, different segment reflectivity, etc., which can influence the calibration curves of the edges. All these effects result in discrepancies between the theoretical sine and cosine curve and the experimental data. For an optimal performance of the sensor in open loop, it is necessary to calibrate the segmented mirror in order to determine the piston steps accurately. However, since all the calibration curves pass through zero, the performance in closed loop is not modified.

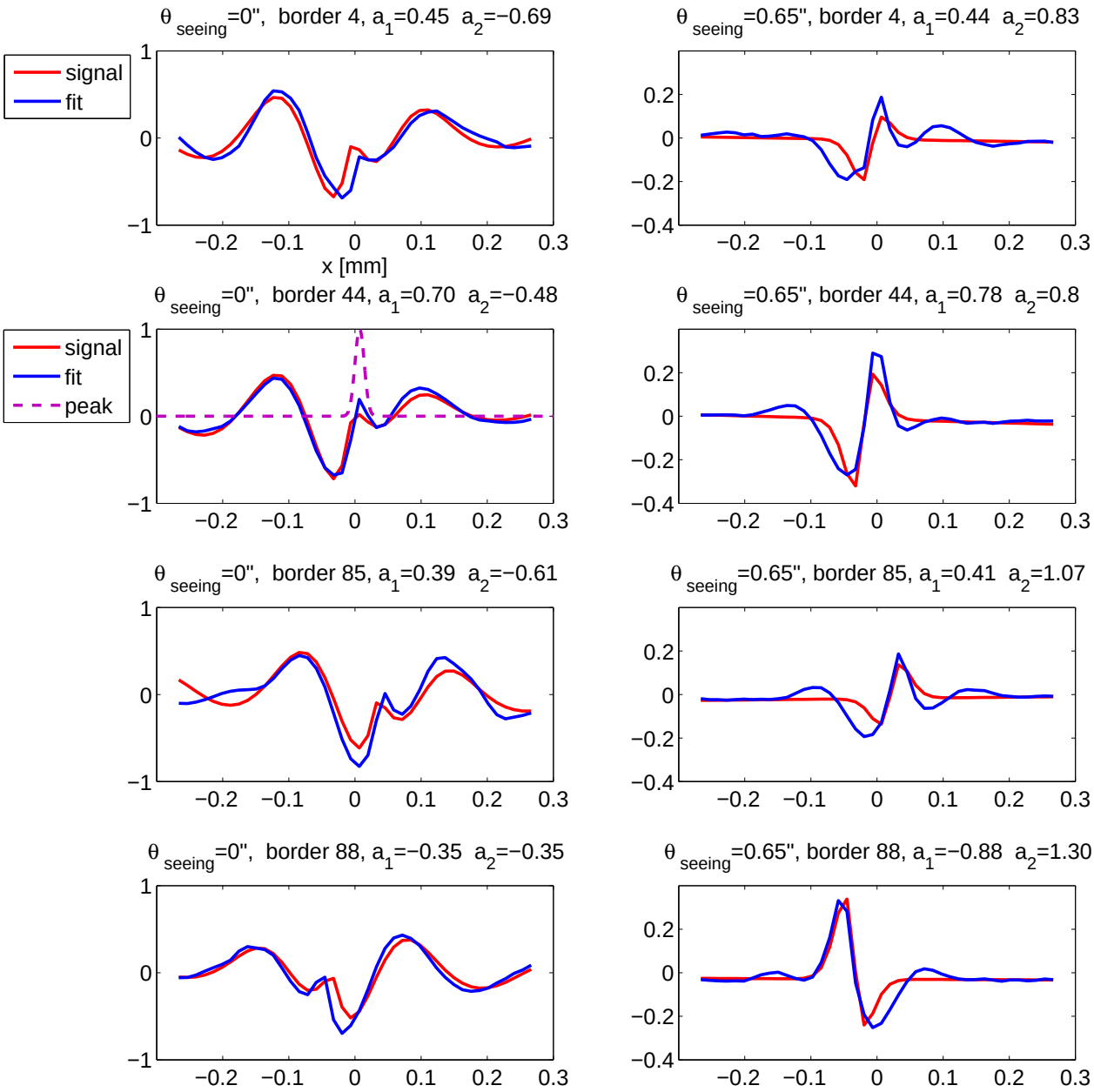

Figure 7.3: Signals and their associated fitted signals for different borders, $\Delta p = \lambda/2$, without turbulence in the left column and with turbulence in the right column.

7.1.2 Phase mask misalignment

A shift of the phase mask with respect to the central peak of the point spread function has a major impact on the calibration curves.

For the measurements described below, the *reference position* of the mask is the *best* alignment achieved for the phase mask.

To measure the effect of such a shift, the phase mask is shifted by ±0.15" in the x and y directions around the reference position and the calibration curves for each alignment of the phase mask are evaluated. The calibration curves for three borders of different orientation are plotted in Figure 7.4.

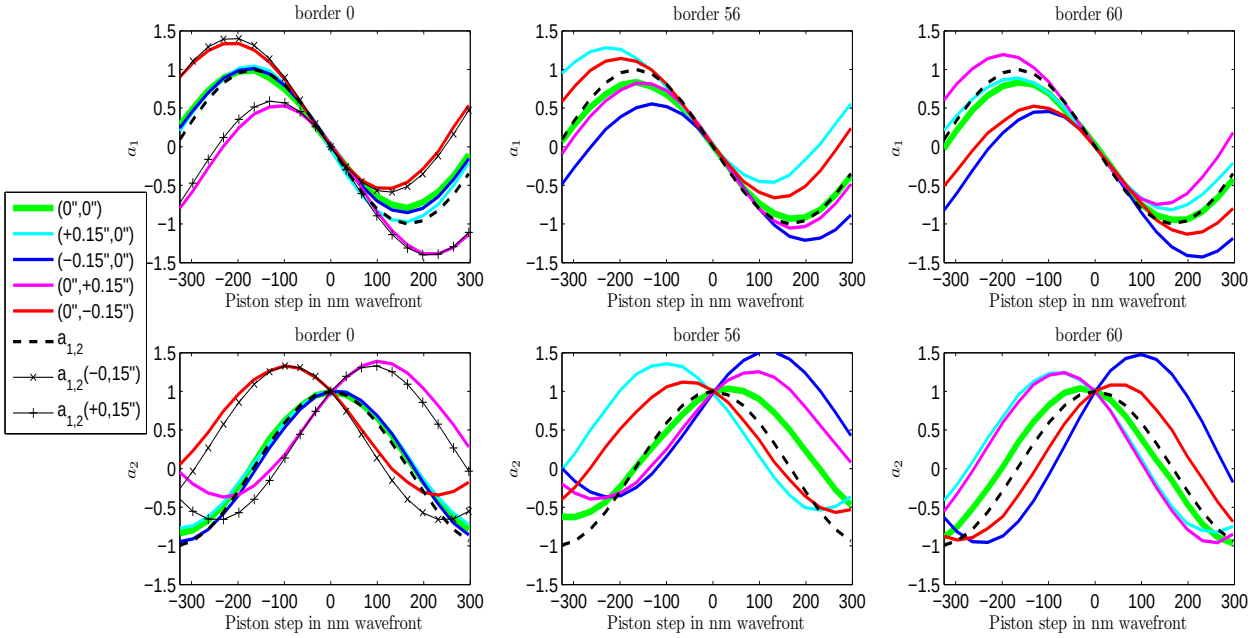

Figure 7.4: Calibration curves for the fitting parameters a_1 (top row) and a_2 (bottom row) for different alignments of the phase mask and different borders. The three borders shown have different orientations: border 0 is oriented at 0 degree, border 56 at 60 degrees and border 60 at -60 degrees (Figure A.1 in Appendix A shows the indexation used on the ASM.) For border 0, the theoretical calibration curves given by Eqs.(7.4) for a_1 and (7.6) for a_2 are shown for $\delta_1 = +0.15$" and $\delta_1 = -0.15$".

A misalignment of the mask leads to a vertical shift of the calibration curve, which will, however, still pass through zero. The slope of the calibration curve around zero also remains unchanged. Therefore, the requirements on the alignment for closed loop operation can be relaxed.

Border 0 is an edge which is parallel to the horizontal axis. A horizontal shift of the mask has no influence on the calibration curves while a vertical shift does. A positive vertical misalignment leads to a decrease in the amplitude of the signal while a negative vertical

misalignment leads to an increase in the amplitude of the signal. This effect has been theoretically analyzed by Yaitskova et al. for the Mach-Zehnder interferometer [86]. The result was that a shift of the pinhole in a direction corresponding to the higher segment greatly decreases the signal intensity, while a shift of the pinhole in the other direction similarly increases the signal intensity [86].

The calibration curves can be described by the expression [86]:

$$a_1(\Delta\varphi) = A\sin(\Delta\varphi + \delta_1) - A\sin(\delta_1). \tag{7.4}$$

The parameter δ_1 depends on the ratio of the phase mask misalignment w_x to the diameter of the phase mask a. For $w_x < a/4$, it can be shown theoretically that δ_1 is approximately a linear function of the shift [86]:

$$\delta_1 \approx 2.8\frac{w_x}{a}. \tag{7.5}$$

For the fitting parameter a_2, the following function, which models the misalignment of the phase mask, has been determined with a standard fitting procedure:

$$a_2(\Delta\varphi) = C\cos(\Delta\varphi + 2\delta_1) - C\cos(2\delta_1) + C. \tag{7.6}$$

Eqs. (7.4) and (7.6) are plotted for border 0 for $\delta_1 = \pm 0.15$" in Figure 7.4. The curves are indicated in the legend of the plots as $a_{1,2}(-0.15")$ and $a_{1,2}(+0.15")$.

The shifts of the calibration curves of borders 56 and 60 is different since they are oriented at 60 and -60 degrees. Figure A.1 in Appendix A shows the indexation used on the ASM.

To find tolerances for the misalignment of the phase mask, the phase mask is shifted in steps of 0.16" in the y direction, perpendicular to the horizontal edges, from -0.5" to +0.5", around the reference position. For each position of the phase mask, the calibration curves are recorded. Only the borders parallel to the horizontal axis (or perpendicular to the phase mask shift) are analyzed. The results are shown in Figure 7.5.

While all calibration curves still pass through zero, the changes in the slope of the calibration curves around zero start to be critical for misalignments of the mask larger than $|w_x| > 0.33$", when the focal point is on the edge of the phase mask.

From this result and with the addition of a safety margin, a requirement for the alignment of the phase mask is defined as:

$$|w_x| < \frac{a}{4}. \tag{7.7}$$

With $a = 1$", $|w_x| < 0.25$" and, in the case of ZEUS, 1" = 0.6 mm in the focal plane, the requirement is $|w_x|[\text{mm}] < 0.15$ mm.

The plate scale of the future E-ELT is of 3.6 mm per arcsecond. The requirement, $|w_x| < \frac{a}{4}$, is, in mm for $a = 1"$: $|w_x|[\text{mm}] < 0.9$ mm, which can easily be achieved with a tip-tilt mirror.

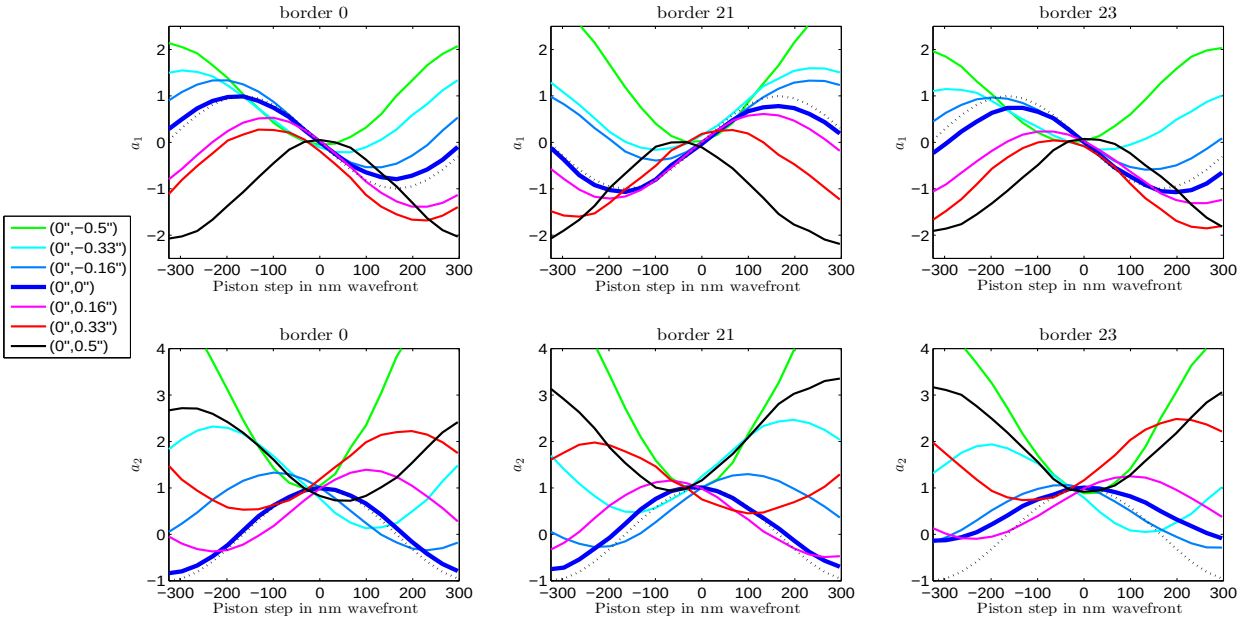

Figure 7.5: Calibration curves for the fitting parameters a_1 (top row) and a_2 (bottom row) for different alignments of the phase mask in the y direction and different borders. The three borders are oriented at 0 degrees. (Figure A.1 in Appendix A shows the indexation used on the ASM.)

7.2 Coherence method

Different methods to increase the capture range of a phasing wavefront sensor have been presented in Section 6.5. A multi-wavelength phasing algorithm has been implemented and successfully tested on sky [78] with the Zernike Phase Contrast Sensor. This section shows the results obtained with the coherence method.

An optical filter, with a central wavelength $\lambda = 650$ nm and a finite bandwidth $\Delta\lambda = 100$ nm has been used. The coherence length l_c of this filter is then given by

$$l_c = \frac{\lambda^2}{\Delta\lambda} = \frac{650^2}{100} = 4225 \text{ nm} = 6.5\ \lambda. \tag{7.8}$$

The coherence function of a filter of coherence length l_c is given by:

$$\Gamma(x) = A\ \sin\left[\frac{2\pi(x - x_0)}{\lambda}\right] \text{sinc}\left(\frac{x - x_0}{l_c}\right) \tag{7.9}$$

where x_0 represents the location of the maximum of the coherence.

The segments are moved in such a way that the range covered by the piston movements is $[-12\lambda, +12\lambda]$, which is larger than the coherence length l_c with steps of $\lambda/4$ between each movement of the segments. The edge signals are then analyzed with the fitting algorithm

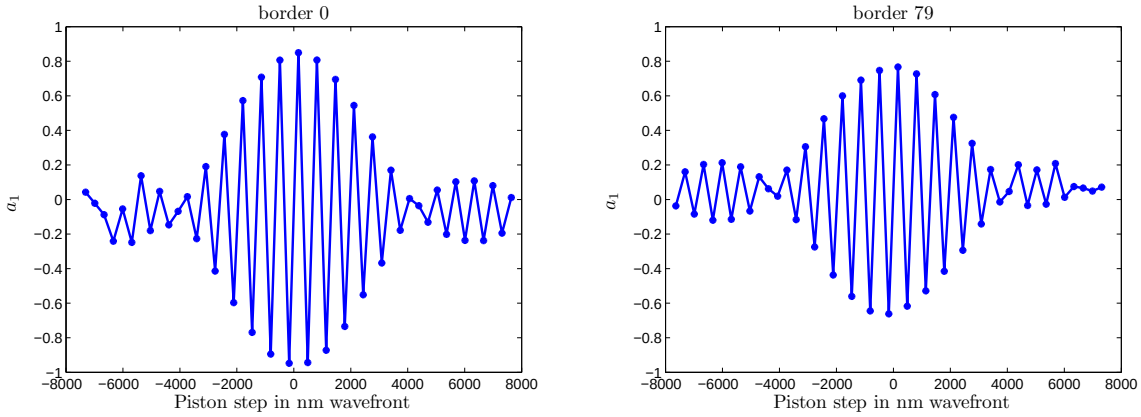

Figure 7.6: a_1 fitting parameter for two edges as a function of the piston step height. Each point represents a measurement. A broad band filter ($\lambda = 650$ nm, $\Delta\lambda = 100$ nm) with a coherence length $l_c = 4225$ nm has been used for the measurement.

described in Section 6.4. Figure 7.6 shows the fitting parameter a_1 plotted as a function of the piston step.

The amplitude of the fitting parameter a_1 is modulated by the coherence envelope (Eq. (7.9)) of the broadband filter. A similar result has been obtained for the fitting parameter a_2.

The well defined shape of the envelope shows that the capture range of the Zernike Phase Contrast Sensor can be extended from $\pm\lambda/4$ to a few μm, depending on the bandwidth of the optical filter.

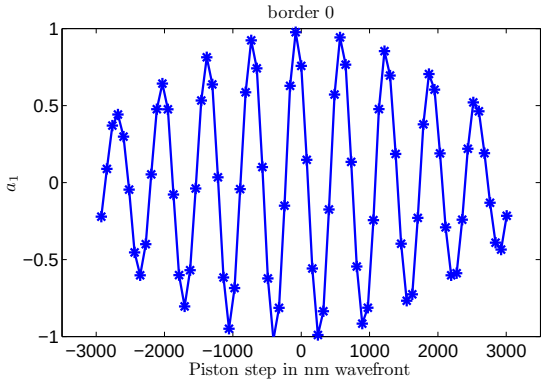

Figure 7.7: a_1 fitting parameter for border 0 as a function of the piston step height without the turbulence generator. Each star represents a measurement.

The same procedure has been repeated, but with steps of $\lambda/16$ between two consecutive movements of the segments and with a smaller range, $[-4.5\lambda, +4.5\lambda]$, covered by the piston movements. The results are shown for the same edges, without and with the turbulence generator, in Figures 7.7 and 7.8, respectively. The optimum alignment corresponding to

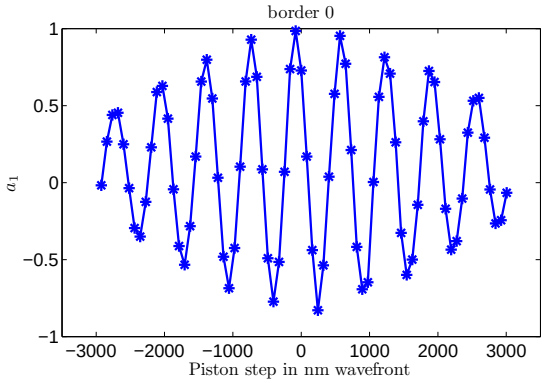

Figure 7.8: a_1 fitting parameter for border 0 as a function of the piston step height with the effects of atmospheric turbulence emulated by MAPS ($\theta_{\text{seeing}} = 0.65$"). Each point represents a measurement.

the maximum of the coherence, can now be determined with a precision of approximately $\lambda/4$.

Figure 7.8 shows that the atmospheric disturbances (generated by MAPS in the laboratory) do not modify the coherence measurements, apart from a small decrease in the amplitude.

The coherence method can be used in operation, changing the spectral bandwidth of the optical filter at every iteration. The measurements can be started with a narrow bandwidth filter covering a large range of pistons at the expense of a reduced accuracy. The bandwidth of the optical filter shall then be increased to improve the precision of the measurement of the optimum alignment.

One can fit the coherence function (Eq. (7.9)) associated with the filter to the data in order to find the maximum of coherence.

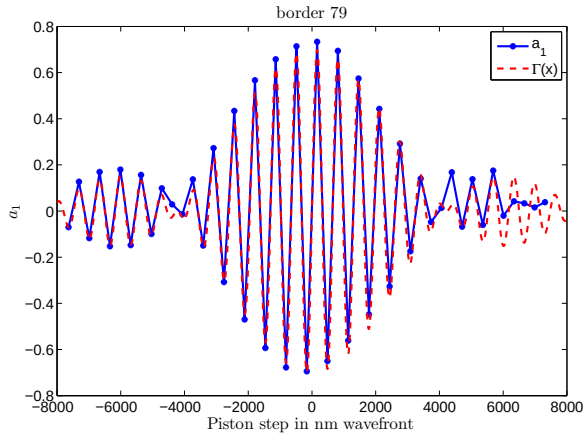

Figure 7.9: a_1 fitting parameter for border 79 as a function of the piston step height. The coherence function of the filter, $\Gamma(x)$, is fitted to the data.

The coherence length of an optical filter with a central wavelength of 800 nm and a bandwidth of 10 nm is $l_c = 64$ μm. Measured at the surface of the mirror, the segments must be aligned within a range of $\approx \pm 30$ μm for this particular filter. Since the mechanical alignment of the segments will provide a precision of about 20 μm, measured at the surface of the mirror, this technique can be used when segments are exchanged. However, a bright star is required to compensate for the loss of photons due to the narrow bandwidth of the filter.

In Figure 7.9, $\Gamma(x)$ is fitted to the data of the edge 79. One obtains $A = 0.7$ and $x_0 = 0$ in this particular case, that is, the segments are already well aligned.

7.3 Closed loop measurements

Most of the measurements, which have been performed in the laboratory and on sky, were performed in closed loop. In this section, a typical closed loop cycle convergence curve is shown and the principle is explained.

The initial ASM configuration, unless mentioned otherwise, is a random distribution of pure segment piston with a wavefront RMS of 52 nm and a wavefront peak to valley of 200 nm (Figure 7.10). We refer to this configuration as *Random200*.

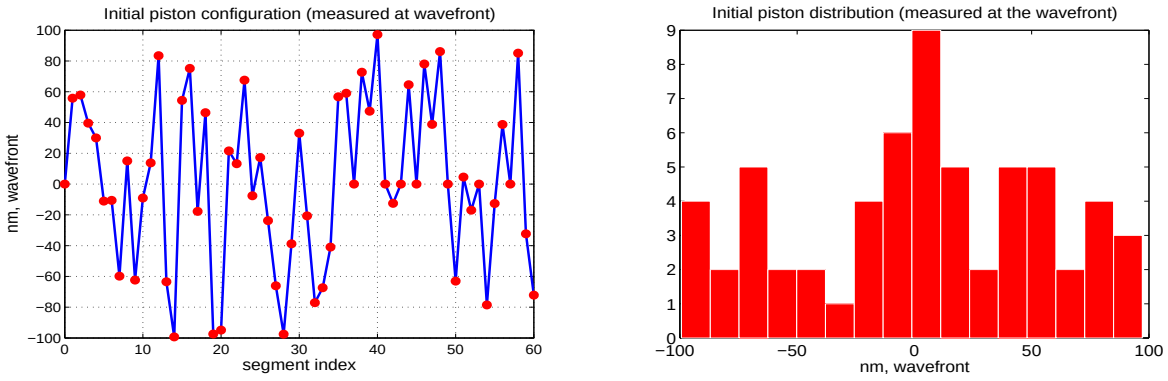

Figure 7.10: Initial piston distribution for the configuration *Random200*.

Starting from the initial ASM configuration using a closed loop correction cycle, the phasing sensor measurements of piston, tip and tilt usually converge after 3 iterations and the process is stopped after 10 iterations. The *final accuracy* σ_{fa}, which is used to quantify the performance of the phasing sensor, is defined as the average value of the RMS of piston, tip and tilt as measured by the IM over the last 3 to 5 iterations. The stability of the loop is defined as the standard deviation of the RMS calculated over these 3 to 5 stable iterations.

The same optical filter, centered on the 650 nm wavelength with a bandwidth of 100 nm, was used for all the tests.

Two typical closed loop cycle convergence curves obtained in the laboratory with and without the turbulence generator are shown in Figure 7.11. The seeing generated with the turbulence generator was $\theta_{\text{seeing}} = 0.65$" and the integration time was 20 seconds. The

RMS of the piston error during the closed loop converges to $\sigma_{\text{fa}} = 3.6$ nm without the turbulence generator and to $\sigma_{\text{fa}} = 4.1$ nm with the turbulence generator.

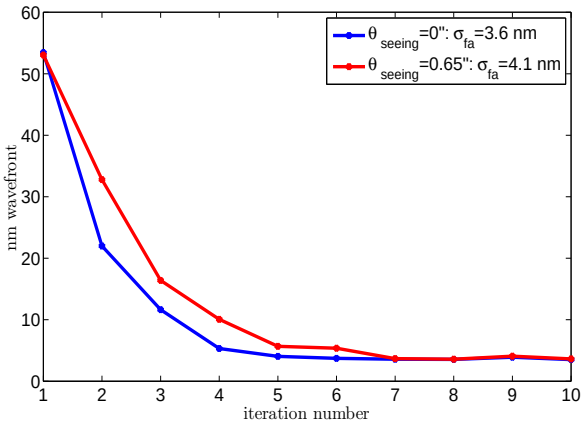

Figure 7.11: Two closed loop convergence cycle curves, with and without turbulence. The final accuracy is, without the turbulence generator, of $\sigma_{\text{fa}} = 3.6$ nm and $\sigma_{\text{fa}} = 4.1$ nm with the turbulence generator.

7.4 Final accuracy

The purpose of the following test is to measure the final accuracy of the phasing loop as a function of the flux and to establish a limiting star magnitude, which is defined as the faintest star magnitude with which the phasing sensor is capable of driving the segmented mirror in closed loop to a final accuracy smaller than 30 nm RMS [83]. We define ν_{30} as the number of counts per pixel in the CCD image which corresponds to this limiting star magnitude.

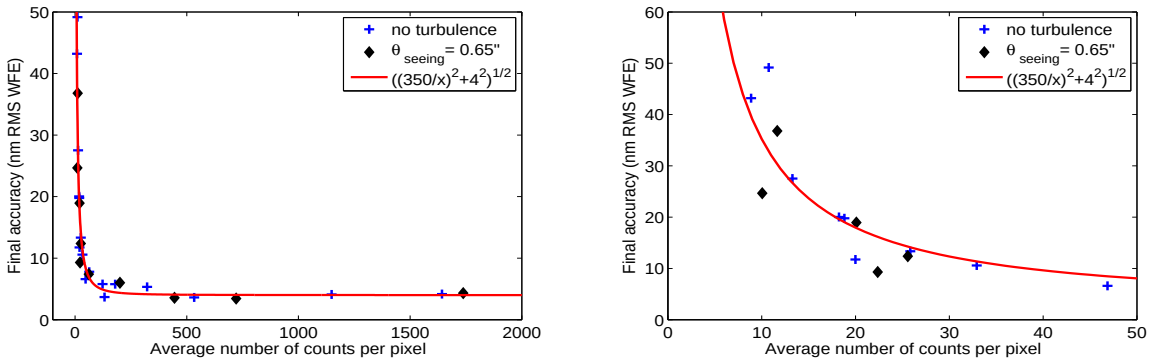

Figure 7.12: Final accuracy as a function of the average number of counts per pixel with and without the turbulence generator.

Figure 7.12 shows the final accuracy obtained with and without atmospheric turbulence as a function of the average number of counts per pixel, ν. One can distinguish between a low and a high flux regime. In the high flux regime, for $\nu > 40$, the final accuracy converges to 4 nm RMS wavefront, with and without atmospheric turbulence.

In the low flux regime, however, the performance is limited by the noise of the CCD. Figure 7.13 shows the normalized images for $\nu = 8.9$ and $\nu = 18.2$ photons per pixel. The noise of the CCD appears as lines which, in this case, are parallel to edges and disturb the measurements.

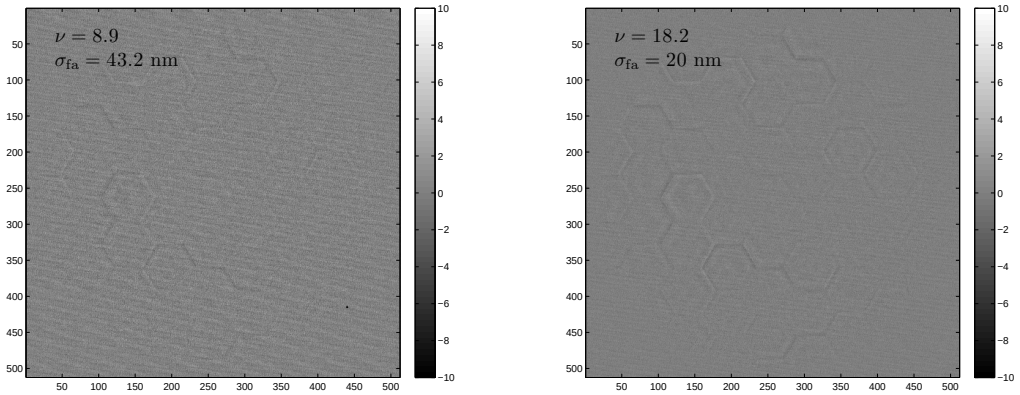

Figure 7.13: Normalized images for $\nu = 8.9$ (left) and $\nu = 18.2$ (right) photons per pixel. The noise of the CCD appears as lines parallel to the edges.

The magnitude M_{V} of the star can be calculated from the number of counts on the CCD image:

$$M_{\text{V}} = -2.5 \left[\log \left(\frac{\phi \ \epsilon}{\Delta\lambda \ \mathcal{A} \ \tau \ \rho \ \Delta t} \right) + Z_0 \right] \tag{7.10}$$

where

- ϕ is the number of photons that hit the CCD per second. The CCD gain G is 1.5, therefore $\phi = N/G$ where N is the number of ADUs.
- ϵ is the energy per photon, $\epsilon = \frac{hc}{\lambda_m}$, with $\lambda_m = 650$ nm, $c = 3 \cdot 10^8$ m $\cdot$ s^{-1} and $h = 6.67 \times 10^{-34}$ USI.
- $\Delta\lambda$ is the bandwidth of the light. In our case, $\Delta\lambda = 100$ nm.
- τ is the light transmission of the optics, in front of the sensor. We assume a transmission of $\tau = 0.65$ for the telescope and $\tau = 0.7$ for the phasing sensor.
- ρ is the quantum efficiency of the CCD: $\rho = 87\%$ at 650 nm.
- $Z_0 = 7.6408$ is the zero point at a wavelength of 640 nm [23].

- $\mathcal{A}$ is the collecting area. We assume the collecting area $\mathcal{A}$ to be the one of the VLT. With a central obscuration of about 1.8 %, $\mathcal{A} \approx 0.98 \cdot \pi \cdot 4.1^2 \mathrm{m}^2$.
- Two different integration times are considered: $\Delta t = 20$ sec and $\Delta t = 60$ sec.

Figure 7.14 shows the star magnitudes which correspond to the average number of counts per pixel of Figure 7.12, computed with Eq. (7.10), taking into account the two selected integration times.

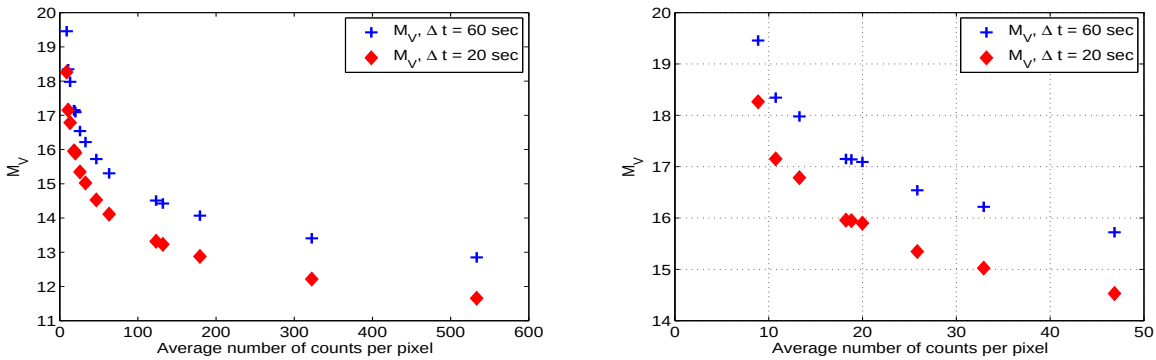

Figure 7.14: Star magnitude M_V which corresponds to the average number of counts of Figure 7.12, calculated with Eq. (7.10), considering two different integration times: $\Delta t = 60$ sec and $\Delta t = 20$ sec.

With an equivalent star magnitude $M_\mathrm{V}|_{\Delta t=20} = 17$ and $M_\mathrm{V}|_{\Delta t=60} = 18$ ($\nu_{30} \sim 13$ counts per pixel), with and without atmospheric turbulence, the sensor is still able to measure phase steps with a precision that is sufficient for the ASM piston distribution to converge to a final accuracy σ_fa of 27.5 nm wavefront RMS.

Chapter 8

Experimental results on sky

The measurements obtained in the laboratory have validated the methods and algorithms developed for the Zernike Phase Contrast Sensor (Chapter 6).

The main difference between the experiments made in the laboratory and the ones made on sky comes from the effects generated by atmospheric turbulence. The turbulence generator used in the laboratory emulates a periodic atmosphere with a constant seeing value. On sky, the seeing conditions can change very fast. We have hoped to cover a range of seeing conditions as large as possible. Unfortunately, most of the time the seeing was only in the range $[0.5", 1.2"]$.

The Zernike Phase Contrast Sensor has been studied on sky during a total of 6 nights. We first show in Section 8.1 how calibration curves, acquired on sky with $\theta_{\text{seeing}} > 1.5"$, are still well defined for the fitted parameter a_1. The optimal integration time required to average the seeing is discussed in Section 8.3. The results presented in Section 7.4 have been repeated on sky, and we show how the limiting star magnitude depends on the strength of the atmospheric disturbances. In Section 8.5 we analyze the optimal diameter of the phase mask for different seeing conditions. The dependence of the performance the correction type (piston or tip-tilt) (Section 8.6), the normalization type used (Section 8.7) and the effects of the seeing on the final accuracy (Section 8.8) are also presented.

The initial configuration of the ASM is the *Random200* (defined in Section 7.3), with a random distribution of pure segment piston with a wavefront RMS of 52 nm and a wavefront peak to valley of 200 nm.

All the presented results are always given in nanometer, measured on the wavefront, and not on the surface.

The results of this Chapter have also been presented in the paper by Surdej et. al. [75].

8.1 Calibration curves

Figures 8.1 (a) and (b) show the fitted coefficients a_1 and a_2, defined in Section 6.4, as functions of the piston step for three different borders of the ASM. These curves have been acquired on sky with seeing conditions higher than 1.5". The phase mask with a diameter

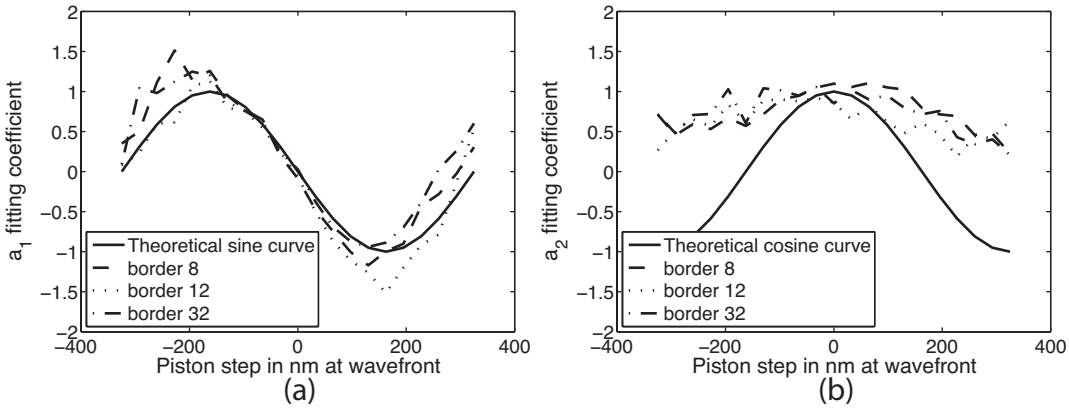

Figure 8.1: Parameters a_1 (a) and a_2 (b) as functions of Δp for three different borders. $\lambda = 650$ nm and $\Delta\lambda = 100$ nm. $\theta_{\text{seeing}} \approx 1.5$", $a = 2$".

$a = 2$" has been used.

Despite the bad seeing conditions, the curves of the parameter a_1 are still well defined. The Zernike Phase Contrast Sensor would be capable of measuring the piston steps also for bad seeing conditions in the range $[1.5", 2"]$.

During the acquisitions of these curves, the internal metrology was in an unstable state, due to vibrations of the bench. The noise on the calibration curves comes from this instability and not from the poor seeing conditions.

As for the results obtained in the laboratory, described in Section 7, the curves for the parameter a_2 are noisy and cannot be used for the determination of the piston step.

8.2 Closed loop convergence cycle

The evolution of the RMS of the piston error during a typical closed loop cycle, performed on sky with a bright star, under seeing conditions with $\theta_{\text{seeing}} \approx 0.5$" (phase mask size $a = 1$"), and with an integration time of 20 seconds, is shown in Fig. 8.2. The RMS of the piston error reaches a final accuracy of 6.7 nm after 4 iterations.

8.3 Final accuracy and integration time

The aim of this test is to determine the required integration time to sufficiently average out the effects generated by the turbulence. This test has been performed under different seeing conditions.

Fig. 8.3 shows that the optimal integration time Δt, is, under good seeing conditions, of the order of 10 seconds to 20 seconds.

With integration times longer than $\Delta t = 20$ seconds the final accuracy will not be improved.

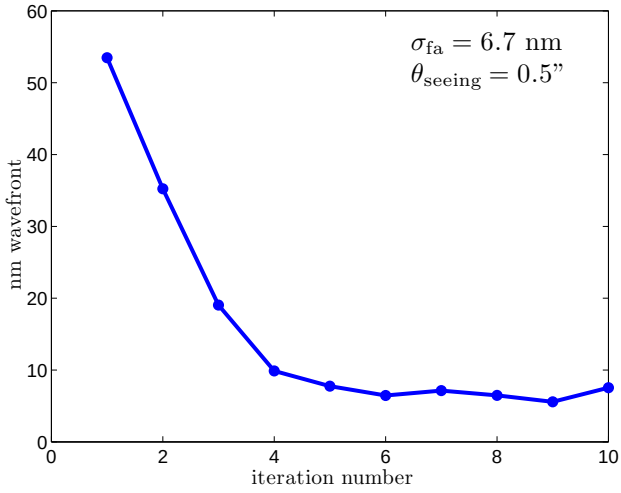

Figure 8.2: closed loop cycle obtained on sky with a bright star, seeing of 0.5” and the phase mask of diameter $a = 1$”.

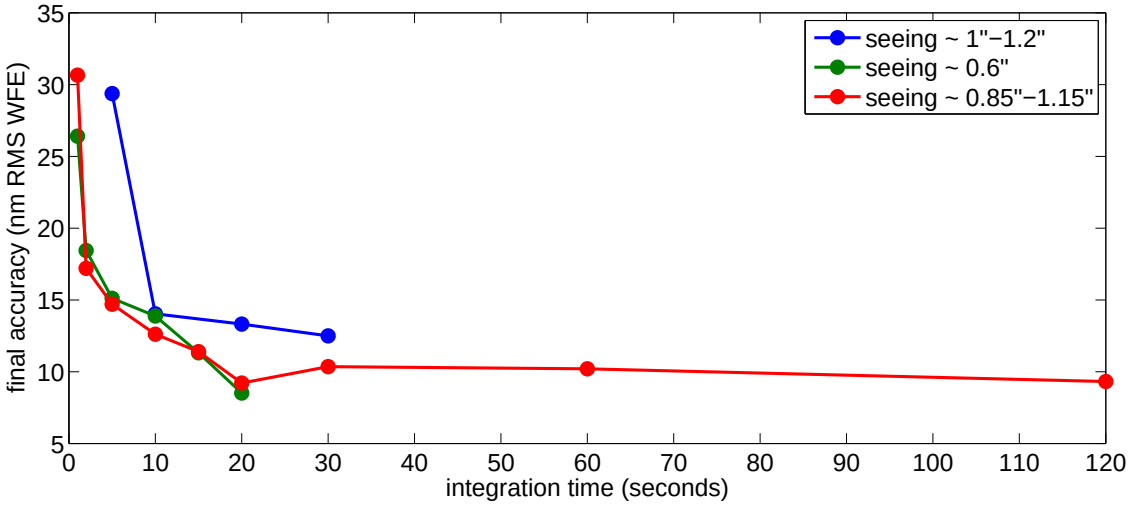

Figure 8.3: Final accuracy as a function of the integration time for different seeing conditions.

8.4 Final accuracy and star magnitude

As mentioned in the general introduction, a phasing sensor that could work with a faint star would give the option to perform optical phasing measurements during operation and therefore deliver continuous closed loop updates of the reference values of the edge sensors. Therefore, as in the Chapter dedicated to laboratory measurements, we have repeated the test performed in Section 7.4 to establish a limiting star magnitude with which the phasing sensor is capable of driving the segmented mirror in closed loop to a final accuracy smaller than 30 nm RMS [83].

The change in flux was done by choosing stars with different magnitudes and/or adding a neutral density filter. Binning 2×2 (*bin2*) has also been used with fainter stars. We define ν_{30} as the number of counts per pixel in the CCD image which corresponds to the limiting star magnitude M_{V}.

The equivalent values of the star magnitudes, $M_{\mathrm{V,sky}}$ are calculated from the catalogue values of the observed stars taking into account the absorption from the neutral density filters and the rest of the optics on the APE bench.

This test has been performed under different seeing conditions and with different integration times:

- *Test1*: $\theta_{\mathrm{seeing}} \approx 1" - 1.2"$, $a = 1.5"$, $\Delta t = 60$ sec,
- *Test2*: $\theta_{\mathrm{seeing}} \approx 0.5" - 0.8"$, $a = 1"$, $\Delta t = 20$ sec.

The final accuracies as functions of the number of counts are shown in the plots of Figures 8.4 and 8.5 for *bin1* and *bin2*, respectively. Table 8.1 gives a summary of the results with Δt representing the integration time, a the diameter of the phase mask, Δw the signal width in pixels in the *bin1* configuration, and $M^{\mathrm{bin1}}_{\mathrm{V,sky}}$ and $M^{\mathrm{bin2}}_{\mathrm{V,sky}}$ are the limiting star magnitudes achieved for *bin1* and *bin2*, respectively.

$\sigma_{\mathrm{HighFlux}}$ is the value to which the final accuracy converges in the high flux regime, independently of the number of counts.

Table 8.1: Final accuracy and limiting star magnitude

Test	θ_{seeing}	Δt	a	Δw	$\sigma_{\mathrm{HighFlux}}$	ν_{30}	$M^{\mathrm{bin1}}_{\mathrm{V,sky}}$	$M^{\mathrm{bin2}}_{\mathrm{V,sky}}$
1	1"-1.2"	60 sec	1.5"	6.8 pixels	12 nm	114	14	15
2	0.5"-0.8"	20 sec	1.0"	11.3 pixels	8 nm	38	14.7	15.7

The influence of atmospheric turbulence on long exposure images is, as seen in Section 5.4.4, to reduce the amplitude of the signal as well as the width of the signal. The width of the signal is also affected by the diameter of the phase mask. The seeing conditions and the diameter of the phase mask will therefore affect the final accuracies obtained as well as the limiting star magnitude.

In Fig. 8.4, one can clearly distinguish between a high flux regime and a low flux regime.

In the low flux regime, the CCD electronic noise and the turbulence are the main contributors to the final accuracy and the limiting star magnitude rather than the photon shot noise. The noise in the images is analyzed in the frequency domain in Section 9.3.1.

In the high flux regime, many parameters are responsible for the limiting accuracy $\sigma_{\mathrm{HighFlux}}$, for example the residual turbulence, the obscuration created by the foot-print of the secondary mirror support and polishing errors. The pupil of the telescope is not de-rotated during the observations, i.e. the spider and the polishing errors rotate with respect to the ASM. Therefore, at each image acquisition with the sensor, the spider and the residual polishing errors of M1 are at different locations in the image. In the normalized

image, given by Eq. (6.4), I^{ref} is subtracted from I^{S}, the residual polishing errors and the secondary mirror support foot-print are added due to the rotation of the pupil. However, very few borders are affected and the fitting process is rather insensitive to the narrow obstruction of the signal by the spider. The major polishing errors of M1 are of the order of 35 nm RMS. These effects are analyzed in the frequency domain in Section 9.3.2.

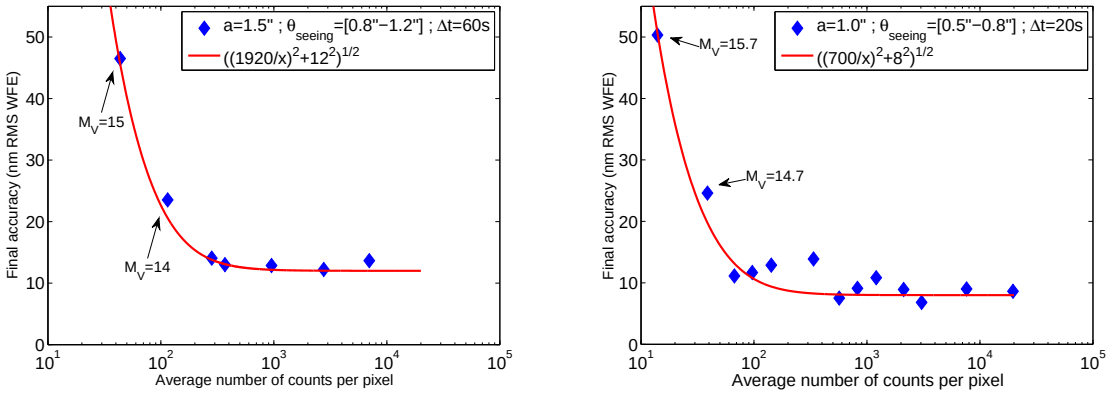

Figure 8.4: Final accuracy as a function of the average number of counts per pixel for different seeing conditions, phase masks and integration times. The CCD is configured with binning 1×1. Left: *Test1*, Right: *Test2*.

When the CCD is configured to *bin2*, the limiting star magnitude is increased by one as illustrated in Fig. 8.5. The limiting star magnitudes achieved in *Test1* and *Test2* are 15 and 15.7, respectively.

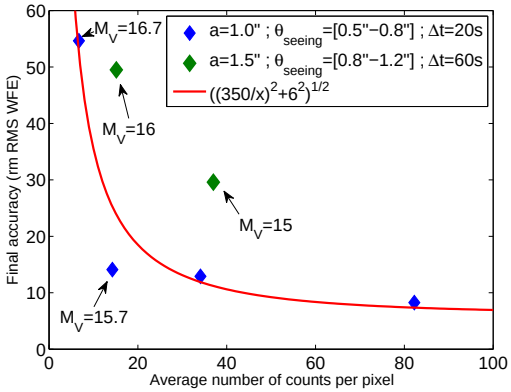

Figure 8.5: Final accuracy as a function of the average number of counts per pixel for different seeing conditions, phase masks and integration times. The CCD is configured with binning 2×2. The number of counts corresponds to the number of counts in the binning 1×1 case.

8.4.1 Comparison between on sky and laboratory measurements

In the laboratory, the same results are obtained with and without atmospheric disturbances. The limiting star magnitudes achieved for integration times $\Delta t = 20$ sec and $\Delta t = 60$ sec are $M_{\mathrm{V}}|_{\Delta t=20} = 17$ and $M_{\mathrm{V}}|_{\Delta t=60} = 18$, respectively, which correspond to a number of $\nu_{30} \sim 13$ counts per pixel.

The limiting star magnitudes $M_{\mathrm{V,sky}}$ shown in Table 8.1 are calculated from the catalogue values of the observed stars, taking into account the loss of light due to the optics on the APE bench.

The limiting star magnitudes obtained on sky can be calculated from the number of counts (Eq.(7.10)) assuming integration times $\Delta t = 20$ sec and $\Delta t = 60$ sec. With the plot in Figure 7.14, the magnitudes can be directly deduced from the number of counts:

- *Test1* : $\nu_{30} = 38$, $M_{\mathrm{V}}|_{\Delta t=20} = 14.8$ and $M_{\mathrm{V}}|_{\Delta t=60} = 16$ ($M^{\mathrm{bin1}}_{\mathrm{V,sky}}$=14.7),
- *Test2* : $\nu_{30} = 114$, $M_{\mathrm{V}}|_{\Delta t=20} = 13.5$ and $M_{\mathrm{V}}|_{\Delta t=60} = 14.7$ ($M^{\mathrm{bin1}}_{\mathrm{V,sky}}$=14).

The catalogue values, $M_{\mathrm{V,sky}}$, and the calculated values of star magnitude are in good agreement.

There is an improvement of two star magnitudes in the laboratory with respect to the telescope. There are two explanations:

CCD noise: The CCD used in the laboratory, with a noise of 7 counts RMS/sec is different from the one used on sky, with 12 counts RMS/sec.

Environment: The environment is more stable in the laboratory: the IM precision is better, and of course atmospheric turbulence has a major impact on the final accuracy.

In the laboratory, the limiting star magnitude is not modified in the presence of atmospheric disturbances generated by MAPS. On the contrary, on sky, the seeing has a major impact on the limiting star magnitude: the amplitude and the width of the signal are strongly reduced by the seeing, and therefore, the limiting star magnitude is also reduced.

The turbulence generated by MAPS is not as complex as the real atmosphere, and therefore, the effects on the measurements, associated with MAPS, are not as strong as in a real telescope.

With a star magnitude of 15, the sky coverage is of 97% and with a star magnitude of 16, it is of 100 % [5]. Therefore, the star magnitudes achieved, in the laboratory and on sky, allow to perform optical phasing also during observations.

8.5 Phase mask test

The principle of the sensor is based on the filtering of the atmospheric turbulence in the focal plane with a phase mask having a size which can be adapted to the given seeing conditions.

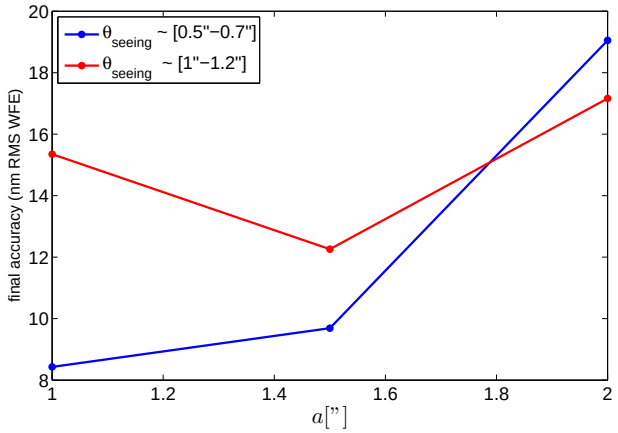

Figure 8.6: Dependence of the final accuracy on the diameter of the phase mask a for different seeing conditions.

Fig. 8.6 shows the final accuracy as a function of the size of the phase mask for different seeing conditions. With a seeing of [0.5"-0.7"], the smaller phase mask with a diameter $a = 1$" is the best choice. For a seeing of [1"-1.2"], the phase mask with a diameter $a = 1.5$" is optimal. Unfortunately, the seeing has very rarely been worse than 1.2".

The optimal size of the phase mask seems to be approximately 1.5 times larger than the size of the seeing disk; that is $a \approx 1.5\ \theta_{\text{seeing}}$. This confirms the theoretical prediction given by Eq. (5.73).

8.6 Tip-tilt

The tip-tilt algorithm as explained in Section 6.6 has been tested on sky with a bright star, under seeing conditions with $\theta_{\text{seeing}} \approx 0.4$" (diameter of the phase mask $a = 1$") and with an integration time of 10 seconds.

The initial configuration of tip-tilt applied on the ASM was a random configuration with 0.15 arcsecond wavefront PtV on the ASM, which corresponds to a wavefront RMS of 0.045 arcsecond. The final accuracy obtained is 0.005 arcsecond in tip and in tilt, which corresponds to approximately 16 nm RMS wavefront of piston step errors at the edges for segments having an inner diameter of 1.05 meter. The closed loop convergence cycle is shown in Figure 8.7. The slow convergence is due to a small gain used in the control loop.

8.7 Final accuracy and different normalization procedures

Closed loop correction cycles have been performed without and with the use of the IM flat reference image, i.e. with Eqs. (6.3) and (6.4), respectively.

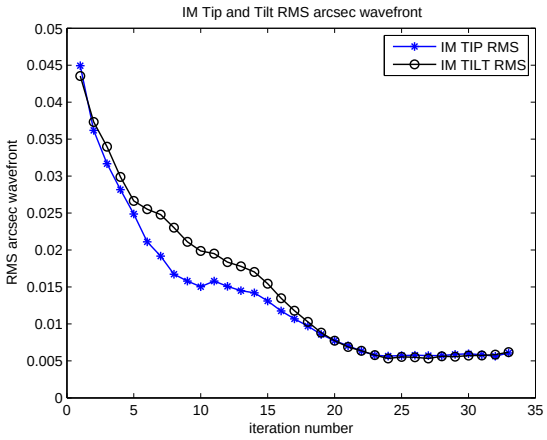

Figure 8.7: Tip-tilt closed loop cycle, $a = 1$", $\theta_{\text{seeing}} \approx 0.4$" and $\Delta t = 10$ sec.

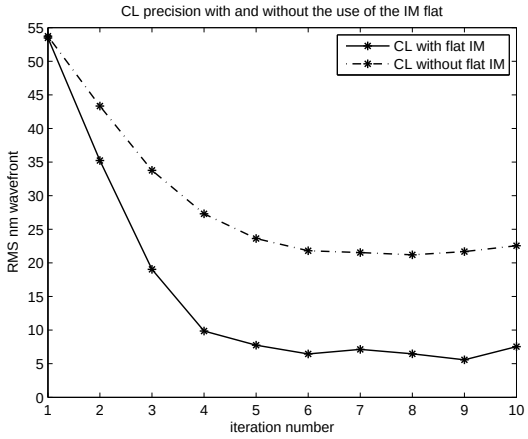

Figure 8.8: Piston correction in closed loop with and without the use of the internal metrology flat image.

The segmented mirror converges to an edge minimizing configuration which corresponds to a final accuracy of 22 nm when the reference image I^{ref} is not used (Eq. (6.3)). For the phasing of future segmented telescopes, no preliminary calibration performed on sky is therefore necessary to achieve the required phasing accuracy if the edge errors of the segments are similar to the ones of the ASM.

With the use of the reference image, see Eq. (6.4), the RMS of the final configuration is 6.7 nm. This is actually the best performance which has been obtained with the Zernike Phase Contrast Sensor during all the tests performed on sky under very good seeing conditions with $\theta_{\text{seeing}} \approx 0.5$" and with a highly stable IM with a precision of 3 nm RMS. The closed loop convergence curve is shown in Fig. 8.2.

8.8 Seeing

The final accuracy as a function of the seeing is shown in Fig. 8.9, containing all the data obtained on sky under similar operational conditions, e.g with the same optical filter and a large number of counts. The seeing variations during a measurement are represented by the horizontal error bar in the plot. The vertical error bars represent the stability of the loop.

Since the seeing is generated by Kolmogorov turbulence, we assume that the final accuracy σ_{fa} has the following dependence on the seeing:

$$\sigma_{\text{fa}} = \sqrt{\tau^2 + \gamma\ \theta_{\text{seeing}}^{5/3}} \tag{8.1}$$

where τ is a constant value due to systematic errors and γ is a numerical coefficient dependent on the wavelength. The following values for the parameters τ and γ are obtained by fitting the data in Fig. 8.9: $\tau = 5.3$ nm and $\gamma = 108$ nm/arcsec$^{5/3}$.

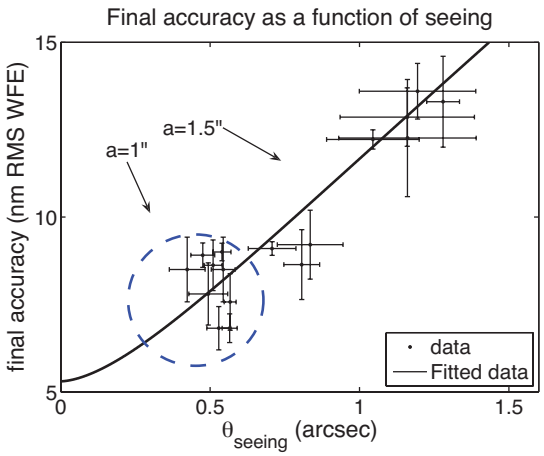

Figure 8.9: Final accuracy as a function of the seeing. The horizontal error bars represent the seeing variation during the closed loop cycle measurements. The vertical error bars represent the stability of the loop. The curve represents the assumed dependence $\sqrt{\tau^2 + \gamma\ \theta_{\text{seeing}}^{5/3}}$ on the seeing, with τ and γ being numerical coefficients. The encircled data have been acquired with a phase mask $a = 1$" and the rest of the points with a phase mask $a = 1.5$".

Chapter 9

Analysis using the theory of diffraction in segmented mirrors

In this chapter a complementary and new approach is used to understand the results obtained with the Zernike Phase Contrast Sensor on sky (Section 8). All the images which are used in this chapter are from the observations performed on sky at the VLT.

The Power Spectral Density (PSD) of the images obtained with the Zernike Phase Contrast Sensor is analyzed with the help of the theory presented in the publications [84, 83]. The work presented here is based on an ESO technical report [89].

Assuming that the phasing sensor can be represented as a linear time invariant system, a filter which models the sensor is calculated from the atmospheric noise in Section 9.2. This filter is very similar to the expression found with a more theoretical approach in Section 5.3.3. In Section 9.3, using the filter, the final accuracy of the sensor is estimated from the measured noise, in the low flux as well as in the high flux regimes. The results are in good agreement with the ones presented in Section 8.4.

The methods presented in this Chapter can be used for measuring the average piston error. The sensor can also be modeled as a high pass filter on the phase of the incoming wavefront.

9.1 PSD of the image of the pupil

The Zernike Phase Contrast Sensor can also act as a pupil camera when the optical beam only passes through the substrate of the mask, and is not affected by the phase filtering of the mask. In this case, we obtain an image of the pupil on the CCD detector, shown in the left image of Figure 9.1. One can see the gaps of the ASM, the obstruction generated by the secondary mirror of the VLT, and the spider. The corresponding PSD is shown in the right image of Figure 9.1.

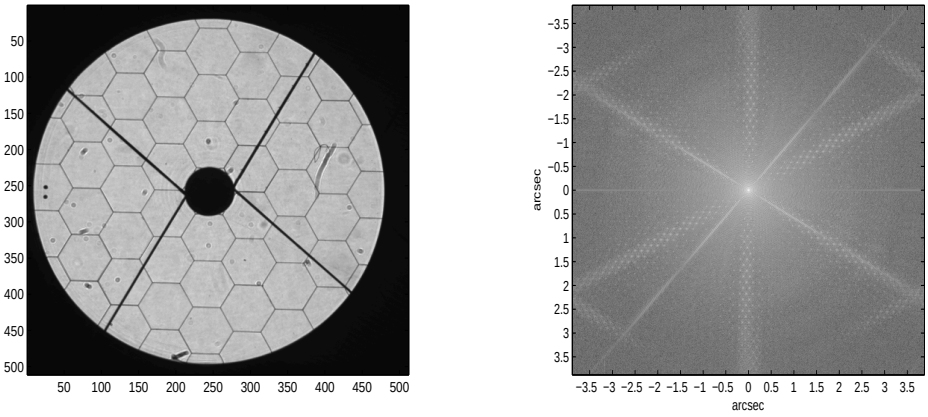

Figure 9.1: (Left:) Image of the pupil. (Right:) PSD of the image of the pupil.

9.2 Description of the system by a transfer function

In Section 5.3.3 we have demonstrated that the Zernike Phase Contrast Sensor behaves as a high pass filter on the phase.

$$\Phi_{\text{signal}}(\mathbf{w}) = H(\mathbf{w})\Phi_{\text{phase}}(\mathbf{w}) \tag{9.1}$$

The filter is given by the following expression:

$$H(\mathbf{w}) = (1/\kappa a)^4|\mathbf{w}|^4, \begin{cases} \kappa = 0.28 & \text{for the sharp edge phase mask ,} \\ \kappa = 0.42 & \text{for the gaussian profile phase mask .} \end{cases} \tag{9.2}$$

In this section, we will derive a similar expression for the filter, but following a different approach.

In Section 2.1.3 of the introduction, we have shown that the statistically averaged PSD of the phase is equivalent to the halo of the PSF [83]:

$$\Phi_{\text{phase}}(\mathbf{w}) = \frac{\sigma_n^2}{N}|t_n(\mathbf{w})|^2. \tag{9.3}$$

In the particular case of pure piston errors, $n = 1$, $\sigma_1^2 = \sigma_{\text{piston}}^2$ and $t_n(\mathbf{w}) = t_1(\mathbf{w})$, which is shown in Figure 2.2, the analytical expression for Φ_{phase} is given by Eq. (2.4).

Introducing Eq. (9.3) into Eq. (9.1) gives

$$\Phi_{\text{signal}}(\mathbf{w}) \quad = \quad H(\mathbf{w})\frac{\sigma_1^2}{N}|t_1(\mathbf{w})|^2. \tag{9.4}$$

$|t_1(\mathbf{w})|^2$ can be derived theoretically, and $H(\mathbf{w})$ will be derived from the variations of the signal due to atmospheric noise. With $t_1(\mathbf{w})$ and $H(\mathbf{w})$ known, σ_1 can then be deduced from Eq. (9.4).

Two sets of data have been used to produce the results presented in this section. The configuration of the system was the following: $a = 1$", $\psi_0 = \lambda/3.7$, $\lambda = 650$ nm, $\theta_{\text{seeing}} \approx 0.5$", and $\Delta t = 20$ sec. The light of bright stars has been used.

9.2.1 Determination of the shape of the filter from the atmospheric noise

The goal of this section is to estimate the expression for the filter $H(\mathbf{w})$ from the variations of the signal generated by atmospheric noise only.

We assume that the Zernike Phase Contrast Sensor acts as a linear time invariant system.

The response of the system to atmospheric turbulence is calculated. The shape of the filter $H(\mathbf{w})$ is calculated from the following assumption:

$$\Phi_{\text{signal,atm}}(\mathbf{w}) = H(\mathbf{w})\Phi_{\text{atm}}(\mathbf{w}) \tag{9.5}$$

where $\Phi_{\text{signal,atm}}(\mathbf{w})$ is the PSD of the signal, which is generated only by the effects of atmospheric turbulence and $\Phi_{\text{atm}}(\mathbf{w})$ is the PSD of the atmosphere, given by the Kolmogorov spectrum of turbulence: $\Phi(\rho) = 0.033\ C_n^2\ \rho^{-11/3}$, where C_n^2 is the atmospheric structure constant.

The PSD of the signal, $\Phi_{\text{signal,atm}}(\mathbf{w})$, is calculated from normalized images of the Zernike Phase Contrast Sensor as follows.

In a closed loop convergence cycle, when the loop is stable, a set of differential images, is calculated from pairs of successive images. The alignment of the segments is assumed to be stable and only the changes induced by atmospheric turbulence contribute to the differential images. The set of differential images is then normalized using the procedure described in Section 6.1, which results in the images I_{Dj}^N. The PSDs of the N normalized differential images is then calculated, $\Phi_{\text{signal,atm}}^{Dj}(\mathbf{w}) = |\widehat{I}_{Dj}^N|^2$. The symbol$\widehat{\ }$represents the Fourier transform. Finally, the mean PSD is calculated from the N individual PSDs: $\Phi_{\text{signal,atm}}(\mathbf{w}) = \sum_{j=1}^{N} \Phi_{\text{signal,atm}}^{Dj}(\mathbf{w})/N$.

It is easier to process the data in one dimension. Therefore, the azimuthal average of $\Phi_{\text{signal,atm}}(\mathbf{w})$ is calculated, and we obtain $\overline{\Phi}_{\text{signal,atm}}(\rho)$. The PSD $\Phi_{\text{atm}}(\rho) = \alpha\rho^{-11/3}$ of the atmosphere is finally fitted to the data, as shown in the left plot of Figure 9.2.

Finally, the filter is calculated from

$$H(\rho) = \frac{\overline{\Phi}_{\text{signal,atm}}(\rho)}{\Phi_{\text{atm}}(\rho)}. \tag{9.6}$$

The results for both sets of data which are shown in the right plot of Figure 9.2, are quite similar. The best fit of the filter is given by the expression:

$$H(\rho) = \text{erf}^2\left[\left(\frac{\rho}{125}\right)^2\right],\ \rho < 222 \tag{9.7}$$

for lower frequencies, and for higher frequencies, a good fit is given by

$$H(\rho) = \exp\left[-\left(\frac{\rho - 222}{300}\right)^2\right],\ \rho > 222 \tag{9.8}$$

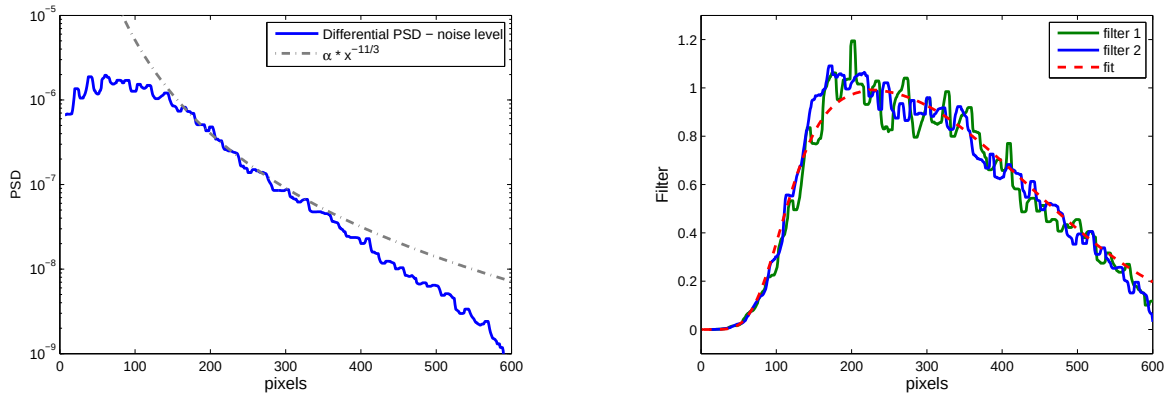

Figure 9.2: Left: $\overline{\Phi}_{\text{signal}}(\rho)$ fitted with the Kolmogorov spectrum of turbulence. Right: Two filters obtained with the corresponding two sets of data.

where ρ is measured in pixels. Using the conversion: 1 pixel$\widehat{=}$0.2295 cycle/pupil $\widehat{=}$ 0.004", Eqs. (9.7) and (9.8) can be expressed in units of arcsecond:

$$H(w) = \text{erf}^2\left[\left(\frac{2w}{a}\right)^2\right], \; w < 0.89", \tag{9.9}$$

$$H(w) = \exp\left[-\left(\frac{w-0.89}{1.2a}\right)^2\right], \; w > 0.89". \tag{9.10}$$

For the low frequencies, the shape of the filter depends only on the diameter a of the phase mask. For small values of w, the erf function can be expanded in a series. If only the lowest term is kept, $H(w)$ is given by:

$$H(w) \approx \left(\frac{w}{0.47a}\right)^4. \tag{9.11}$$

Eq. (9.11) can be compared with Eq. (9.2). The value of the new coefficient, $\kappa = 0.47$, found with the experimental data obtained on sky is close to the two values found analytically for the gaussian profile phase mask ($\kappa = 0.42$) and the sharp edge phase mask ($\kappa = 0.28$).

The approximation given by Eq. (9.11) seems to be valid only for $w < 0.3"$.

The same procedure has been applied to data acquired with the 1.5" phase mask. A widening of the filter by a factor 1.5 has been observed.

9.2.2 Verification of the filter found with the signal image

The aim of this section is to verify the filter $H(\rho)$, calculated in the previous section, and given by Eqs. (9.7) and (9.8), on normalized signal images with segment alignment errors.

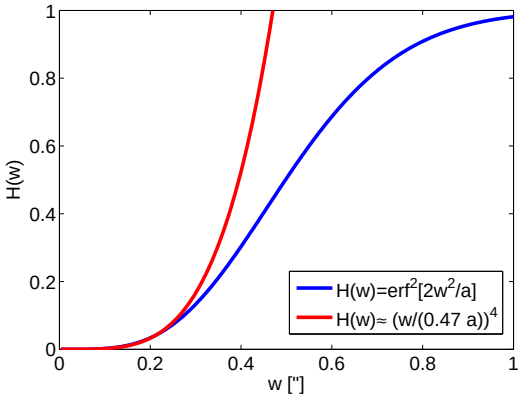

Figure 9.3: Filter and its approximation for small w

The data used in this section are from the same closed loop convergence cycles as in the previous section. However, the first image of the closed loop convergence cycle is used, with the configuration *Random200* generated on the ASM [1].

The steps to evaluate the PSD of the signal are similar to the steps described in the previous section. To remove the speckles from the one-dimensional PSD (after azimuthal averaging), a median filter is applied to the one-dimensional profile.

With

$$\gamma = \frac{\sigma_1^2}{N}, \tag{9.12}$$

we want to solve Eq. (9.4) for γ:

$$\gamma = \frac{\Phi_{\text{signal}}(\mathbf{w})}{H(\mathbf{w})|t_1(\mathbf{w})|^2}. \tag{9.13}$$

The function $|t_1(\mathbf{w})|^2$, which represents the PSF of a single segment, is shown in Figure 2.2 and its analytical expression is given by Eq. (2.4), in Section 2.1.

It is easier to perform this analysis in the one-dimensional case. Therefore, we perform an azimuthal average of all the power spectral densities.

The azimuthal average, $\Phi_{\text{t1}}(\rho)$, of the function $|t_1(\mathbf{w})|^2$, is shown in Figure 9.4.

$\Phi_{\text{signal}}(\mathbf{w})$ is calculated from both sets of data. The left image of Fig. 9.5 is the normalized signal image with a RMS piston error of 52 nm on the wavefront and the right image of Fig. 9.5 is the corresponding PSD. After azimuthal averaging, we obtain $\Phi_{\text{signal}}(\rho)$.

To determine γ, we proceed as follows:

$$\gamma H(\rho)\Phi_{\text{t1}}(\rho) = \Phi_{\text{signal}}(\rho). \tag{9.14}$$

The left hand side of Eq. (9.14) is fitted to the right hand side of the equation, adjusting the coefficient γ.

The result is shown in Figure 9.6. Some segments are masked by the obstruction in

[1] The corresponding segment piston error has a wavefront RMS of 52 nm and a wavefront peak to valley of 200 nm.

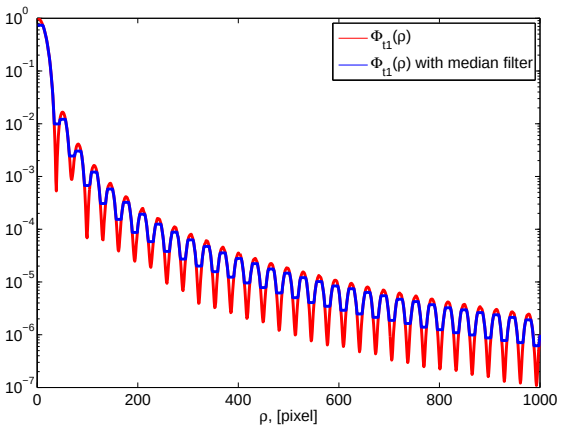

Figure 9.4: $\Phi_{t1}(\rho)$. A median filter has been applied to the profile $\Phi_{t1}(\rho)$ to remove the speckles.

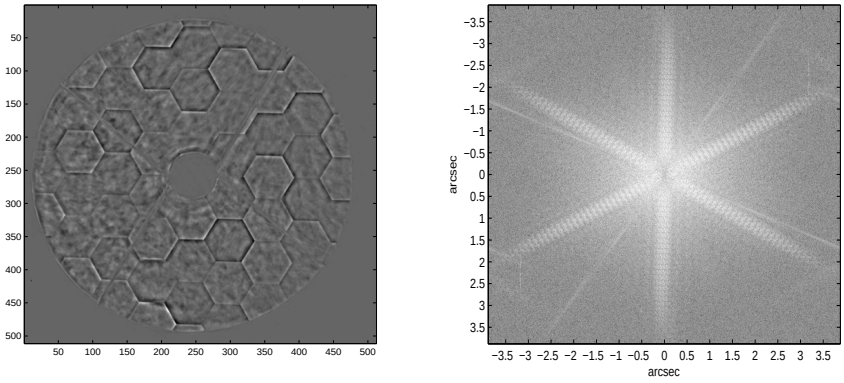

Figure 9.5: Left: Normalized signal image with $\sigma_1^2 = 52$ nm RMS. Right: Power spectral density of the normalized image: Φ_{signal}.

the pupil of the primary mirror of the VLT. In this case, it is better to use the expression $N = A_{\text{tel}}/A_{\text{seg}}$ for the number of segments in Eq. (9.12) where A_{seg} is the area of a single segment and A_{tel} is the total are of the pupil[2].

Finally, the following coefficients γ are obtained for the two sets of data:

- Data 1: $\gamma = 0.0035$ and RMS $= 42$ nm wavefront.
- Data 2: $\gamma = 0.0029$ and RMS $= 38$ nm wavefront.

The calculated values are close to the 52 nm RMS of piston error applied on the ASM.

[2]The size of a segment, flat to flat is 70 pixels, the inner pupil diameter is 70 pixels and the outer pupil diameter 470 pixels. $A_{\text{seg}} = 3659$ and $A_{\text{tel}} = 169646$ pixels^2.

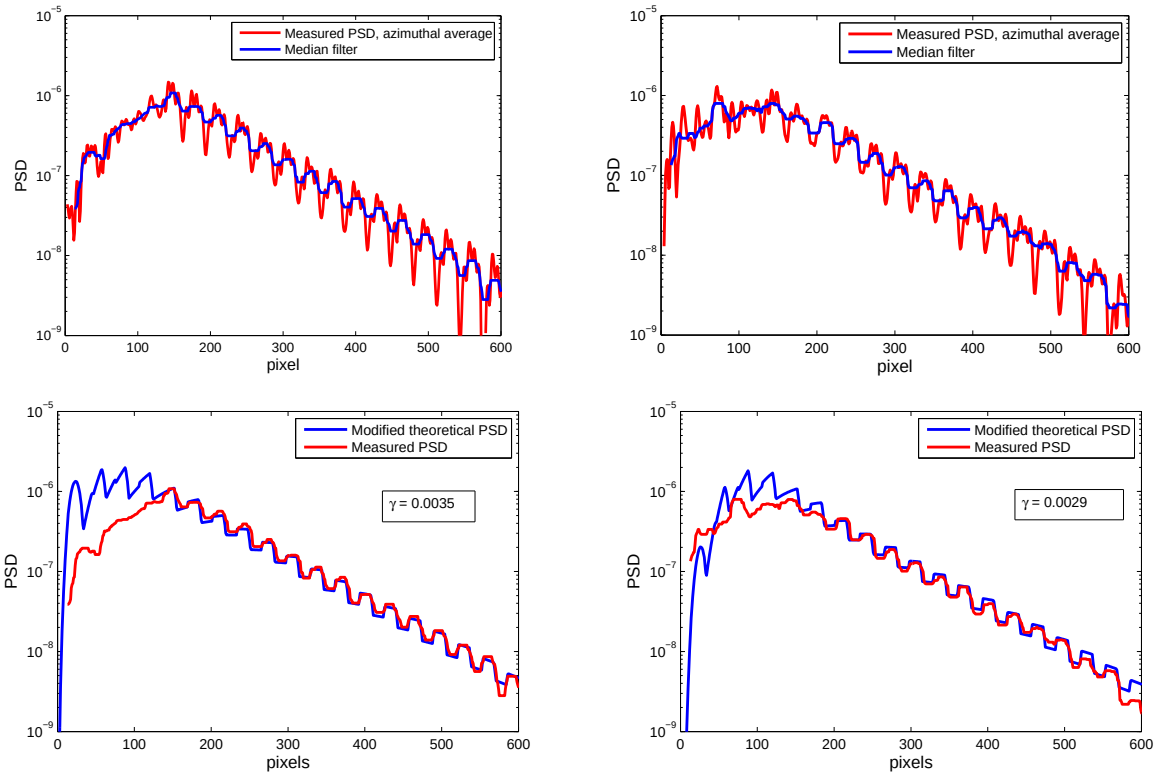

Figure 9.6: Left: First set of data. Right: Second set of data. Top: Measured PSD and median filtering of the function. Bottom: Comparison of the measured PSD and the modified theoretical PSD.

9.3 Estimation of the final accuracy from the measured noise

This section deals with the influence of the different types of noise on the *final accuracy*, which has been measured experimentally in Section 8.4 of Chapter 8.

The different types of noise which affect the *final accuracy* are

- photon noise,
- atmospheric turbulence,
- CCD electronic noise,
- time delay between the acquisition of the signal image and the reference flat image.

In the high flux regime, as explained in Section 8.4, the final accuracy converges to a value σ_{HighFlux} independent of the number of counts. Many parameters are responsible for limiting the accuracy σ_{HighFlux}, for example the residual turbulence, the obscuration created by the foot-print of the secondary mirror support, and the residual polishing errors, which

are amplified by the rotation of the primary mirror with respect to the ASM. In the low flux regime, the image quality is mainly affected by the electronic noise of the CCD.

9.3.1 Low flux regime

The final accuracy obtained in closed loop is related to the amplitude of the noise. The noise in the signal images can be studied in the frequency domain by analyzing the Power Spectral Density of the images.

The images analyzed in this section are from *Test1* and *Test2*, presented in Section 8.4.

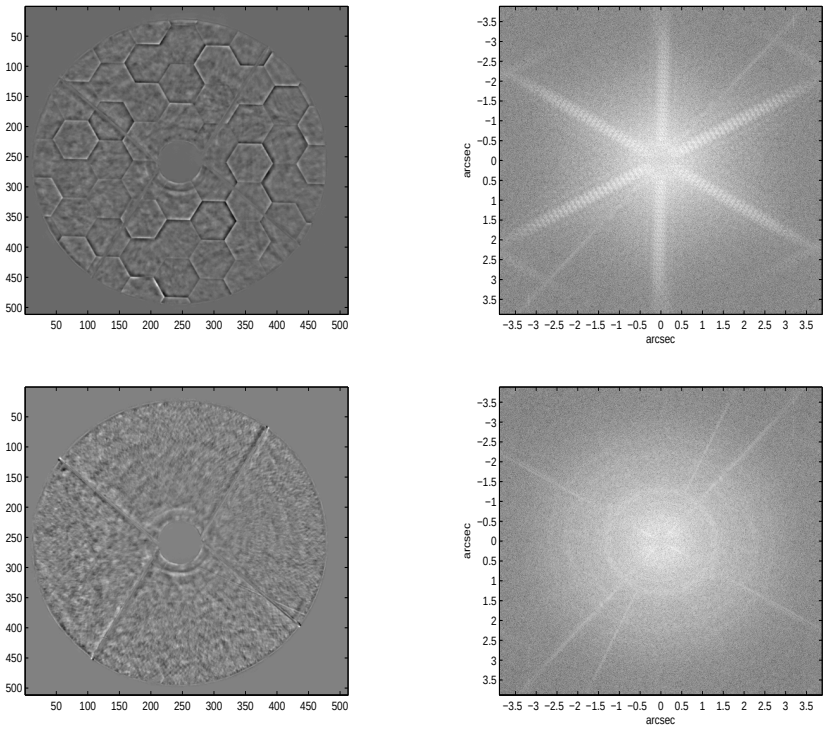

Figure 9.7: Left: normalized image, Right: the corresponding PSD. Initial (top) and after last (bottom) iterations of the closed loop. These images are from *Test2* with 19011 counts per pixel.

The PSDs of the normalized images, obtained from the initial state and after the last iterations of the closed loop, are shown in the left column (top and bottom respectively) of Figure 9.7. The right column shows the corresponding PSDs. In the initial state, the information for the segmentation error is contained in the six rays, which are perpendicular to the edges of the segments. The evolution of the PSD during the closed loop is shown in the right plot of Figure 9.8. During the closed loop, the amplitude of the six rays decreases to finally disappear in the noise in the last iterations [3].

[3] An azimuthal average of the PSD is performed along the 6 rays of the PSD (0.1 radian).

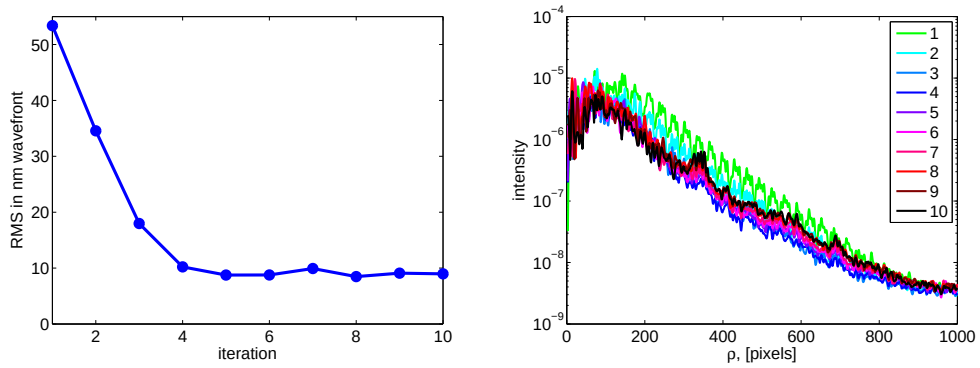

Figure 9.8: Left: RMS of the piston error at each iteration of the closed loop convergence cycle. Right: Evolution of the corresponding PSD during the closed loop. The data shown here corresponds to the images of Figure 9.7.

The RMS of the PSD is calculated in 6 subapertures along the 6 rays of the PSD, where the segment alignment error is predominant.

The RMS σ_{PSD} of the PSD, is calculated from the last four stable iterations of the closed loop convergence cycle and the result is compared to the final accuracy values, σ_{fa}, presented in section 8.4. The strong correlation between σ_{PSD} and the final accuracy σ_{fa} is shown in the plots of Figure 9.9. The coefficient of proportionality, μ_{fit}, was found with a standard fitting procedure.

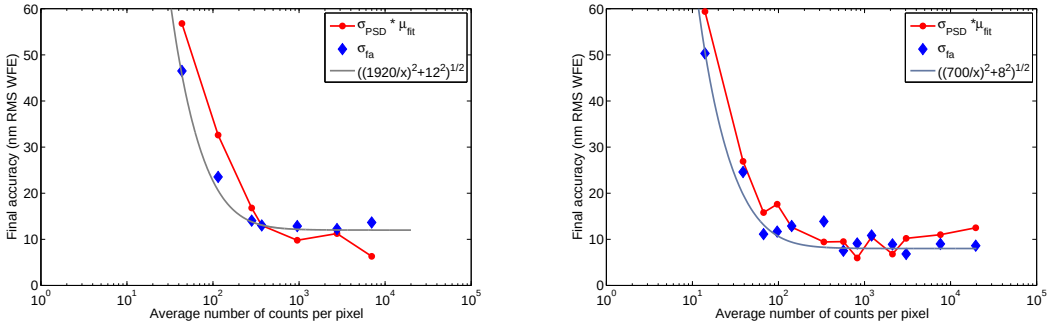

Figure 9.9: Final accuracy as a function of the average number of counts per pixel for different seeing conditions, phase masks and integration time. Left: *Test1*, Right: *Test2*

In the low flux regime, the final accuracy is limited by the electronic noise of the CCD. Figure 9.10 shows the normalized image and the corresponding PSD of the last iteration of the closed loop for different numbers of counts per pixel. Below 150 counts per pixel, the image suffers from a periodic electronic noise. In the frequency domain the periodicity is derived from the peaks, which are symmetrically distributed with respect to the center of the image.

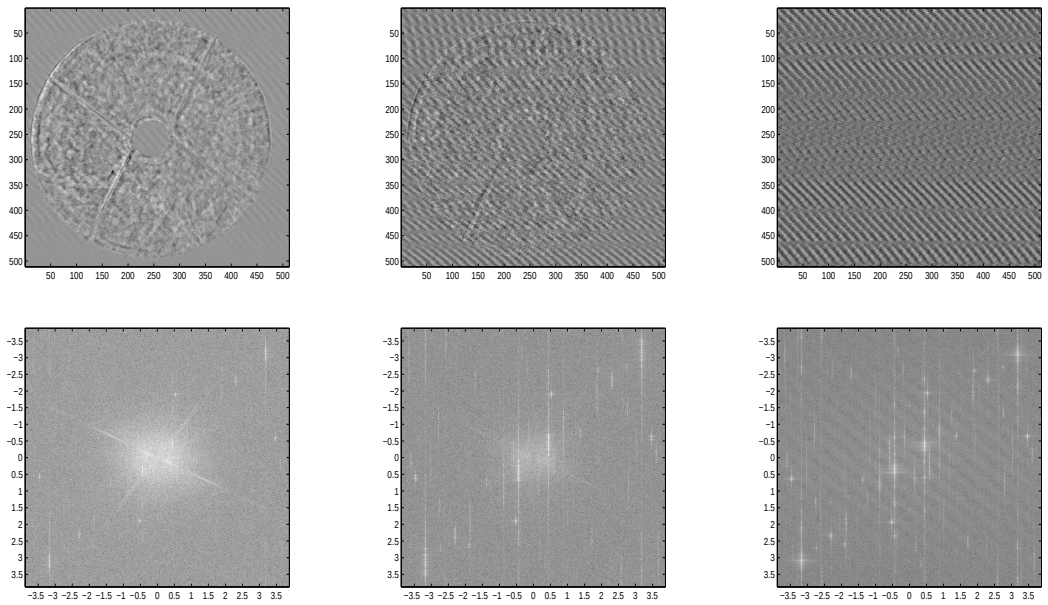

Figure 9.10: Normalized images of the last iteration of the closed loop (top images) and their corresponding PSDs (bottom images) for different intensities. Left: 862 counts per pixel, middle: 142 counts per pixel, right: 8 counts per pixel

9.3.2 High flux regime

All the images analyzed in this section were acquired with integration times of 20 seconds, $a = 1$" and $\lambda = 650$ nm.

Since APE is installed on a Nasmyth platform and does not include a pupil derotator, the VLT pupil and, in particular the spider and the residual polishing errors of the primary mirror rotate with respect to the ASM. Therefore, on each acquired CCD frame, the image of the VLT pupil is in different locations with respect to the image of the ASM pupil. When the normalization procedure is performed using Eq. (9.15):

$$I^{\mathrm{N}} = \frac{I^{\mathrm{S}} - I^{\mathrm{ref}}}{\langle I^{\mathrm{S}} \rangle - B_0}. \tag{9.15}$$

where I^{S} is the signal image and I^{ref} the reference image, the spider is in different locations in I^{S} and in I^{ref}. Therefore in the normalized image, two spiders appear, a negative one and a positive one. The angle between the spiders depends on the time delay Δt between the acquisition of I^{S} and I^{ref}. The left image of Figure 9.11 shows the normalized image, where the time delay Δt is of 527 seconds. The corresponding PSD is shown in the right image of Figure 9.11 where the bright cross in the center comes from the spider.

In Figure 9.12, the PSD is plotted for different time delays Δt. Up to $\Delta t = 160$ sec (which corresponds to the rotation of one pixel at the edge of the pupil) the PSD is similar to the filtered atmospheric turbulence, $\Phi_{\mathrm{signal,atm}}$. With the increase of the time

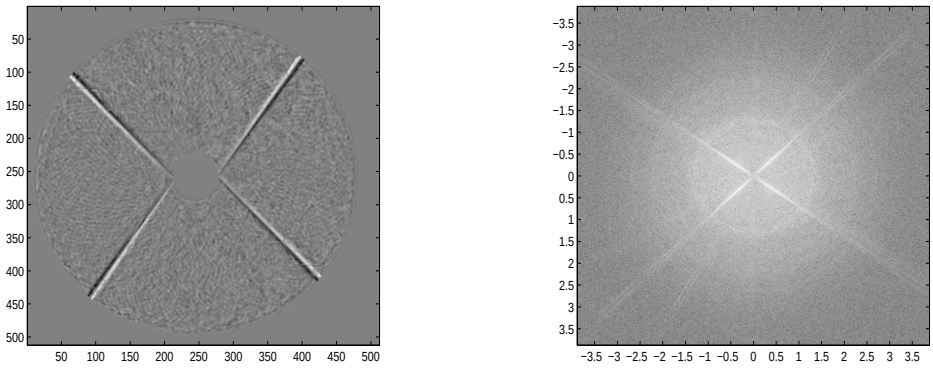

Figure 9.11: Normalized image (left) and PSD (right) for a time delay of 8 min 47 sec.

delay Δt, the amplitude of the PSD increases and a characteristic peak appears at 335 pixels (equivalent to 77 cycles/pupil or 1.34"). We assume that this frequency, which is equivalent to 10 cm projected on the VLT pupil, comes from residual polishing errors, which are not canceled by the subtraction of the images but on the contrary amplified by it. The residual polishing errors which are centro-symmetric are subtracted during the normalization procedure and disappear in the normalized images.

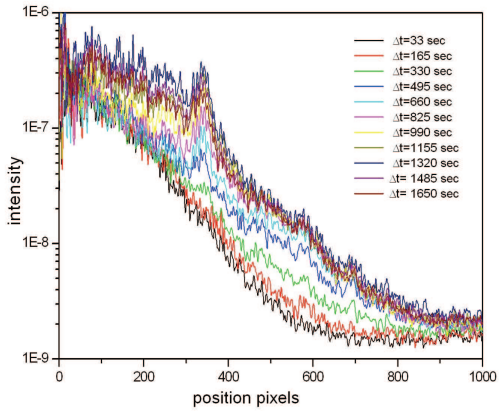

Figure 9.12: PSD of the differential signal for different time delays Δt between the signal image and the ASM flat image. The reference and the signal images were acquired with the ASM in the flat configuration.

Determination of the precision limit for the measurement of the piston steps

According to Eq. (9.3), the intensity of the PSD is proportional to the square of the segmentation error. The azimuthally averaged PSD of the normalized images for different RMS values of the phase errors is shown in Figure 9.13.

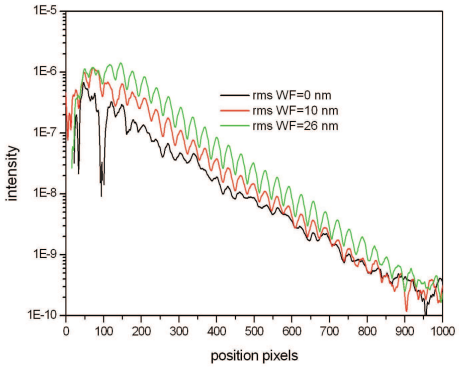

Figure 9.13: PSD of normalized images, for three different RMS values of phase errors. The time delay between the acquisition of the signal image and the reference image is less than 100 sec.

Any type of noise increases the amplitude of the PSD, as seen in the previous section, and therefore limits the amplitude of the measurable piston errors. With the increase of the time delay, the minimal measurable piston error increases.

The lower limit for the measurable piston errors can be calculated by solving Eq. (9.3) for σ_1 and using the PSDs in Figure 9.12.

The left plot of Figure 9.14 shows one of the PSDs of Figure 9.12. Fitting the theoretical PSD, given by $\frac{\sigma_1^2}{N}|t_n(\mathbf{w})|^2$, and multiplying by the filter $H(\rho)$ found in Section 9.2 to the measured PSDs, the value of σ_1 can be deduced.

The results are shown in the right plot of Figure 9.14.

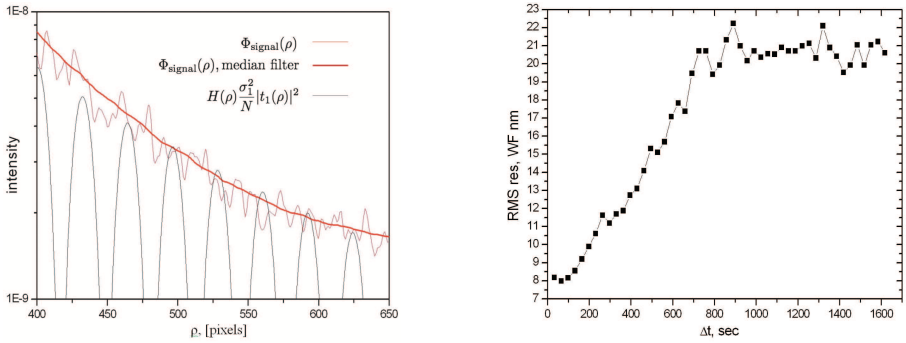

Figure 9.14: Left: Fitting of the theoretical PSD, multiplied by the filter $H(\rho)$ to the measured PSDs. Right: Limiting RMS value of the piston error which can be measured by the sensor as a function of the time delay Δt.

For time delays Δt shorter than 2 minutes the value of the measurable piston error is of the order of 8 nm RMS on the wavefront, which is exactly the figure found with *Test2* in Section 8.4. Then, the RMS increases linearly with the time delay and finally saturates at 21 nm for time delays longer than 800 seconds.

Conclusions

Objectives and results

Segmentation seems to be the only promising technique for the construction of mirrors with diameters of 20 meters and more. The primary mirrors of *Extremely Large Telescopes* will consist of hundreds of hexagonal segments. In order to achieve high spatial resolution and high contrast images, the segments of the primary mirror will have to be phased with a precision of the order of 30 nm RMS.

A phasing wavefront sensor is required to measure the segmentation error with such a high precision. A new technology for the measurement of segment misalignments, the Zernike Phase Contrast Sensor, has been presented in this thesis.

As a first contribution, we have demonstrated, using Fourier optics, the capability of the Zernike Phase Contrast Sensor to measure phase discontinuities, and in particular, piston errors. In the absence of atmospheric disturbances, the signal of the sensor for a phase step is an analytical expression. It is the sum of two terms, an anti-symmetrical part and a symmetrical part. The anti-symmetrical part is identical to the signal obtained with the Mach-Zehnder interferometer. Under the influence of atmospheric disturbances the shape of the anti-symmetric term is still quite similar to the anti-symmetric term without atmospheric disturbances. Therefore, this term can be used for robust measurements of the phase step irrespective of the atmospheric conditions. The symmetric term, however, is strongly modified by the atmosphere.

The second part of our work focused on the development of robust algorithms for the measurement of the phase errors in a segmented mirror. These algorithms have been implemented in the framework of the Active Phasing Experiment, where a mirror made of 61 segments was to be phased with different sensor technologies, including the Zernike Phase Contrast Sensor.

The signal analysis algorithm is based on analytical expected shapes of the signal. Therefore, in principle, no calibration is required, which makes this sensor extremely robust to variations of external parameters such as the operating wavelength and the seeing.

The results obtained in the laboratory and on sky confirm the theoretical predictions.

With measurements performed in the laboratory, we show that in the presence of atmospheric disturbances and without a precise knowledge of the atmospheric conditions, the symmetric term cannot be used to retrieve the information on the piston step. The required precision for the alignment of the mask can be easily achieved in an Extremely

Large Telescope. With monochromatic light, the capture range of the Zernike Phase Contrast Sensor is limited to half of the central wavelength of a color filter. We show that with the coherence method, a technique which has already been successfully demonstrated at the Keck telescopes with the Shack-Harmann sensor, the capture range can be increased from $\pm\lambda/4$ to several wavelengths, and even to a range of ± 30 μm. The precision obtained with the sensor for the measurement of the phase steps is of the order of 4 nm RMS in the laboratory. Finally, the equivalent limiting star magnitude obtained in the laboratory is 18.

On sky, the APE Active Segmented Mirror, of 61 segments was conjugated to the primary mirror of a Unit Telescope of the ESO VLT. The sensor could measure the piston error with an accuracy which has always been below 15 nm RMS wavefront under seeing conditions up to 1.2". The performance which has been achieved lies well within the requirements of 30 nm RMS. The sensitivity to seeing can be minimized by adapting the size of the phase mask in its focal plane to the seeing conditions. Three different phase masks are sufficient to cover a range of seeing from 0.3" up to 2". The best performance achieved under good seeing conditions was 6.7 nm RMS wavefront. A star magnitude of 15.7 was sufficient to achieve an accuracy of 14 nm RMS wavefront. By measuring the discontinuities at two locations along each segment border, the Zernike Phase Contrast Sensor is also capable of measuring the tip-tilt of the individual segments.

We have also analyzed the results obtained on sky with a complementary approach, based on the theory of diffraction for segmented mirrors. Our study demonstrates that the Zernike Phase Contrast Sensor can be modeled as a high-pass phase filter. With the expression derived for this filter, one could confirm the average values for the RMS of the piston steps obtained on sky with other types of measurements.

Perspectives

The Zernike Phase Contrast Sensor is a good candidate to phase the primary mirrors of future Extremely Large Telescopes.

For a 40 meter telescope and a CCD with a sampling of 2048×2048 pixels, the size of a hexagon, from corner to corner, on the CCD would be of the order of 50 pixels, which corresponds to a higher sampling than the one used in this experiment and leaves the possibility to configure the CCD to a 2×2 binning to allow the use of the sensor with fainter stars.

No precise alignment of the pupil on the detector is required as in the case of the Shack-Hartmann type detector, since the position of the pupil on the detector is determined by a registration algorithm. We have shown that the alignment of the phase mask with respect to the focal plane is easy to achieve for an Extremely Large Telescope: it must be better than 0.25" on sky, which corresponds to a displacement of 0.9 mm in the focal plane.

We have shown that Zernike Phase Contrast Sensor can also cope with bad seeing conditions in the range $[1.5", 2"]$.

There is also the possibility to perform optical phasing during observations with the

Zernike Phase Contrast Sensor. The stars, with which a sufficiently accurate alignment was achieved, are faint enough to cover the entire sky, even close to the Galactic pole.

Appendix A

First annex

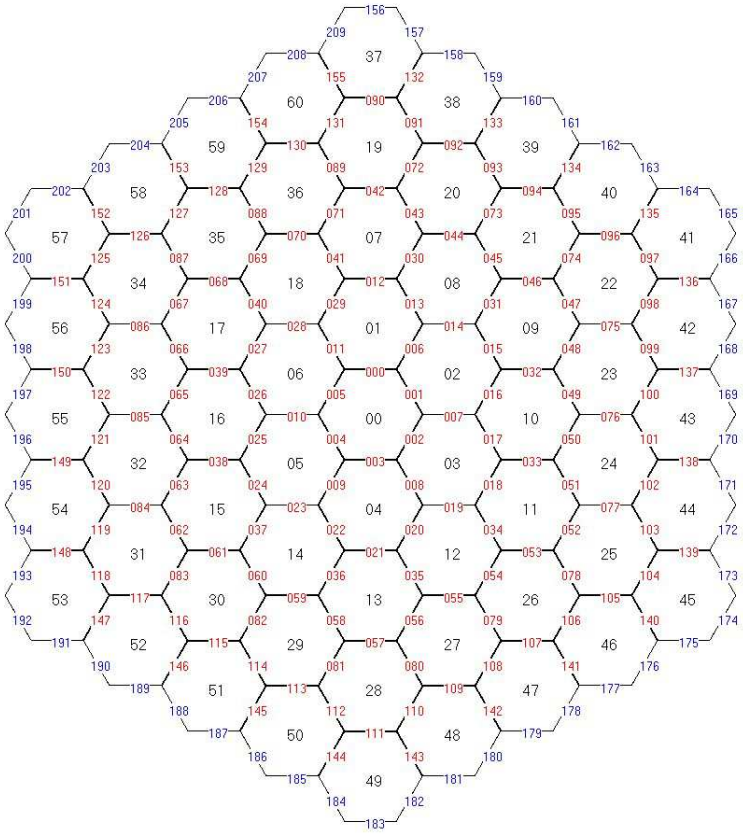

Figure A.1: Indexation of the Active Segmented Mirror

Notations and acronyms

Units

arcmin (or $'$)	minute of arc (2.90888×10^{-4} radian)
arcsec (or $''$)	second of arc (4.848137×10^{-6} radian)
mas	milli-arcsec (10^{-3} arcsec)

Notations

λ	wavelength of the light
$k = 2\pi/\lambda$	wavenumber
r_0	atmospheric coherence length
θ_{seeing}	seeing disk
Ω	Optical Transfer Function
a	Diameter of the pinhole
δ_0	Optical Path Difference
$\psi_0 = k\delta_0$	Phase shift introduced by the Optical Path Difference
$\Delta\varphi$	Differential phase generated by the differential piston Δp
Δp	Differential piston, measured on the wavefront
N	Number of segments
M	Number of edges
$\widehat{\ }$	Fourier transform

Acronyms

ADUs	Analog to Digital Units
AO	Adaptive Optics
APE	Active Phasing Experiment
ASM	Active Segmented Mirror
CCD	Charged Coupled Device
DM	Deformable mirror
DIPSI	Diffraction Image Phase Sensing Instrument
ELT	Extremely Large Telescope
E-ELT	European Extremely Large Telescope
ESO	European Southern Observatory
FWHM	Full Width at Half Maximum
GTC	Gran Telescopio Canarias
HST	Hubble Space Telescope
IM	Internal Metrology
JWST	James Webb Space Telescope
MAPS	Multi Atmospheric Phase screens and Stars
NTT	New Technology Telescope
MZ	Mach-Zehnder
PS	Phase Screen
PSD	Power Spectral Density
PSF	Point Spread Function
OPD	Optical Path Difference
OTF	Optical Transfer Function
OWL	OverWhelmingly Large Telescope
PDS	Phase Discontinuity Sensing
PEACE	Phasing ELT with Adaptive Optics Control Experiment
PSF	Point Spread Function
PSD	Power Spectral Density
PtV	Peak to Valley
PWFS	Phasing WaveFront Sensor
RMS	root mean square
SALT	South African Large Telescope
SVD	Singular Value Decomposition
PTT	Piston Tip Tilt
PYPS	PYramid Phasing Sensor
SHAPS	Shack-Hartmann Phasing Sensor
TMT	Thirty Meter Telescope
UT	Unit Telescope
VLT	Very Large Telescope
WFS	WaveFront Sensor
ZEUS	Zernike Unit for Segment phasing

Bibliography

[1] P. Alvarez, J. M. Rodriguez Espinosa, F. J. Castro Lopez-Tarruella, M. Pi, P. Hammersley, L. Cavaller, B. Siegel, J. Molgo, J. Pancorbo, R. Ascanio, G. Prieto, and J. Calvo. The GTC project: under commissioning. volume 7012, page 701202. SPIE, 2008.

[2] J. R. P. Angel. Ground-based imaging of extrasolar planets using adaptive optics. *Nature*, 368:203–207, 1994.

[3] P. Y. Bely. *The Design and Construction of Large Optical Telescopes*. Astronomy and Astrophysics Library. Springer, 1st edition, 2003.

[4] M. Bonaglia, E. Pinna, A. Puglisi, S. Esposito, J. C. Guerra, R. Myers, and N. Dipper. First cophasing of a segmented mirror with a tunable filter and the pyramid wavefront sensor. volume 7739, page 77392Y. SPIE, 2010.

[5] H. Bonnet. E-ELT performance analysis report. Technical Report E-TRE-ESO-313-0851, ESO, 2010.

[6] C. Cavarroc, A. Boccaletti, P. Baudoz, T. Fusco, and D. Rouan. Fundamental limitations on earth-like planet detection with extremely large telescopes. *A&A*, 447(1):397–403, 2006.

[7] G. Chanan. Limitations on the control of hexagonal mirror segment figures by means of edge measurements. *Appl. Opt.*, 48(31):6074–6081, 2009.

[8] G. Chanan, D. G. MacMartin, J. Nelson, and T. Mast. Control and Alignment of Segmented-Mirror Telescopes: Matrices, Modes, and Error Propagation. *Appl. Opt.*, 43(6):1223–1232, 2004.

[9] G. Chanan, C. Ohara, and M. Troy. Phasing the Mirror Segments of the Keck Telescopes II: The Narrow-band Phasing Algorithm. *Appl. Opt.*, 39(25):4706–4714, 2000.

[10] G. Chanan and A. Pintó. Efficient Method for the Reduction of Large Piston Errors in Segmented-Mirror Telescopes. *Appl. Opt.*, 43(16):3279–3286, 2004.

[11] G. Chanan and M. Troy. Strehl Ratio and Modulation Transfer Function for Segmented Mirror Telescopes as Functions of Segment Phase Error. *Appl. Opt.*, 38(31):6642–6647, 1999.

[12] G. Chanan, M. Troy, F. Dekens, S. Michaels, J. Nelson, T. Mast, and D. Kirkman. Phasing the Mirror Segments of the Keck Telescopes: The Broadband Phasing Algorithm. *Appl. Opt.*, 37(1):140–155, 1998.

[13] G. Chanan, M. Troy, and C. M. Ohara. Phasing the primary mirror segments of the Keck telescopes: a comparison of different techniques. volume 4003, pages 188–202. SPIE, 2000.

[14] G. Chanan, M. Troy, and E. Sirko. Phase Discontinuity Sensing: A Method for Phasing Segmented Mirrors in the Infrared. *Appl. Opt.*, 38(4):704–713, 1999.

[15] S. Chueca, M. Reyes, A. Schumacher, and L. Montoya. DIPSI: measure of the tip-tilt with a diffraction image phase sensing instrument. volume 7012, page 701213. SPIE, 2008.

[16] M. Clampin. Status of the James Webb Space Telescope (JWST). volume 7010, page 70100L. SPIE, 2008.

[17] S. Cuevas, V. G. Orlov, F. Garfias, V. V. Voitsekhovich, and L. J. Sanchez. Curvature equation for a segmented telescope. volume 4003, pages 291–302. SPIE, 2000.

[18] Delavaquerie, E., Cassaing, F., and Amans, J.-P. Focal-plane wavefront sensing for segmented telescope. page 05018, 2010.

[19] P. Dierickx, E. T. Brunetto, F. Comeron, R. Gilmozzi, F. Y. J. Gonté, F. Koch, M. le Louarn, G. J. Monnet, J. Spyromilio, I. Surdej, C. Verinaud, and N. Yaitskova. OWL phase A status report. volume 5489, pages 391–406. SPIE, 2004.

[20] M. Dimmler, T. Erm, B. Bauvir, B. Sedghi, H. Bonnet, M. Müller, and A. Wallander. E-ELT primary mirror control system. volume 7012, page 70121O. SPIE, 2008.

[21] K. Dohlen. Phase masks in astronomy from the Mach-Zehnder interferometer to coronograhs. *Astronomy with High Contrast Imaging II Instrumentation for Coronagraphy and Nulling Interferometry*, 12:33, 2004.

[22] K. Dohlen, M. Langlois, P. Lanzoni, S. Mazzanti, A. Vigan, L. Montoya, E. Hernandez, M. Reyes, I. Surdej, and N. Yaitskova. ZEUS: a cophasing sensor based on the Zernike phase contrast method. volume 6267, page 626734. SPIE, 2006.

[23] The effect of the object magnitude at a specific observation band. URL: http://www.eso.org/observing/etc/doc/gen/formulaBook/node12.html.

[24] ESO. The European Southern Observatory website, 2011. URL: http://www.eso.org/.

[25] S. Esposito and N. Devaney. Segmented mirror co-phasing using Pyramid Sensor. In *Beyond Conventional Adaptive Optics*.

[26] S. Esposito, E. Pinna, A. Puglisi, A. Tozzi, and P. Stefanini. Pyramid sensor for segmented mirror alignment. *Opt. Lett.*, 30(19):2572–2574, 2005.

[27] P. Dierickx et al. OWL Blue Book, OWL concept design report, Phase A Design Review. Technical Report OWL-TRE-ESO-0000-0001 Issue 2, ESO, 2004.

[28] J. R. Fienup. Phase retrieval algorithms: a comparison. *Appl. Opt.*, 21(15):2758–2769, 1982.

[29] J. R. Fienup. Phase retrieval for the hubble space telescope using iterative propagation algorithms. volume 1567, pages 327–332. SPIE, 1991.

[30] R. W. Gerchberg and W. O. Saxton. A practical algorithm for the determination of the phase from image and diffraction plane pictures. *Optik*, 35(2):237–246, 1972.

[31] R. Gilmozzi and J. Spyromilio. The 42m European ELT: status. volume 7012, page 701219. SPIE, 2008.

[32] Jr. Glenn W. Zeiders and E. E. Montgomery IV. Diffraction effects with segmented apertures. volume 3356, pages 799–809. SPIE, 1998.

[33] R. A. Gonsalves. Phase retrieval from modulus data. *J. Opt. Soc. Am.*, 66(9):961–964, Sep 1976.

[34] R. A. Gonsalves. Phase retrieval and diversity in adaptive optics. *Opt. Eng.*, 1982.

[35] R. A. Gonsalves and R. Childlaw. Wavefront sensing by phase retrieval. volume 207, pages 32–39, 1979.

[36] F. Gonté, C. Araujo, R. Bourtembourg, R. Brast, F. Derie, P. Duhoux, C. Dupuy, C. Frank, R. Karban, R. Mazzoleni, L. Noethe, B. Sedghi, I. Surdej, N. Yaitskova, B. Luong, S. Chueca, M. Reyes, S. Esposito, E. Pinna, A. Puglisi, F. Quiros Pacheco, K. Dohlen, and A. Vigan. On-sky testing of the Active Phasing Experiment. *The Messenger*, 136:25–31, June 2009.

[37] F. Gonté, C. Araujo, R. Bourtembourg, R. Brast, F. Derie, P. Duhoux, C. Dupuy, C. Frank, R. Karban, R. Mazzoleni, L. Noethe, I. Surdej, N. Yaitskova, R. Wilhelm, B. Luong, E, Pinna, S. Chueca, and A. Vigan. Active Phasing Experiment: preliminary results and prospects. volume 7012, page 70120Z. SPIE, 2008.

[38] F. Gonté, C. Dupuy, B. Luong, C. Frank, R. Brast, and B. Sedghi. Active hexagonally segmented mirror to investigate new optical phasing technologies for segmented telescopes. *Appl. Opt.*, 48(32):6392–6399, 2009.

[39] F. Gonté, R. Mazzoleni, I. Surdej, and L. Noethe. On-sky performances of an optical phasing sensor based on a cylindrical lenslet array for segmented telescopes. *Appl. Opt.*, 50(12):1660–1667, Apr 2011.

[40] F. Gonté, N. Yaitskova, F. Derie, C. Araujo, R. Brast, B. Delabre, P. Dierickx, C. Dupuy, C. Frank, S. Guisard, R. Karban, L. Noethe, B. Sedghi, I. Surdej, R. Wilhelm, M. Reyes, S. Esposito, and M. Langlois. The Active Phasing Experiment: Part II. design and developments. volume 6267, page 626730. SPIE, 2006.

[41] R. C. Gonzalez and R. E. Woods. *Digital Image Processing*, volume 1. Tom Robbins, second edition, 2002.

[42] M. Johns. Progress on the GMT. volume 7012, page 70121B. SPIE, 2008.

[43] M. Kasper, J.L. Beuzit, C. Verinaud, R. G. Gratton, F. Kerber, N. Yaitskova, A. Boccaletti, N. Thatte, H.M. Schmid, C. Keller, P. Baudoz, L. Abe, E. Aller-Carpentier, J. Antichi, M. Bonavita, K. Dohlen, E. Fedrigo, H. Hanenburg, N. Hubin, R. Jager, V. Korkiakoski, P. Martinez, D. Mesa, O. Preis, P. Rabou, R. Roelfsema, G. Salter, M. Tecza, and L. Venema. EPICS: direct imaging of exoplanets with the E-ELT. volume 7735, page 77352E. SPIE, 2010.

[44] J. Kolb, S. Oberti, E. Marchetti, and F. Quirós-Pacheco. Full characterization of the turbulence generator maps for mcao. volume 6272, page 627258. SPIE, 2006.

[45] M. Langlois, S. Mazzanti, M. Reyes, E. Hernandez, and L. Montoya. ZEUS Design and Analysis report. Technical report, LAM, 2005.

[46] M. G. Lofdahl and H. Eriksson. Resolving piston ambiguities when phasing a segmented mirror. volume 4013, pages 774–782. SPIE, 2000.

[47] M. G. Lofdahl, R. L. Kendrick, A. Harwit, K. E. M., A. L. Duncan, J. H. Seldin, R. G. Paxman, and D. S. Acton. Phase diversity experiment to measure piston misalignment on the segmented primary mirror of the keck ii telescope. volume 3356, pages 1190–1201. SPIE, 1998.

[48] E. Marchetti, R. Brast, B. Delabre, R. Donaldson, E. Fedrigo, C. Frank, N. Hubin, J. Kolb, M. Le Louarn, Jean-Louis Lizon, S. Oberti, F. Quirós-Pacheco, R. Reiss, J. Santos, S. Tordo, A. Baruffolo, P. Bagnara, A. Amorim, and J. Lima. MAD star oriented: laboratory results for ground layer and multi-conjugate adaptive optics. volume 6272, page 62720O. SPIE, 2006.

[49] Martinez, P., Boccaletti, A., Kasper, M., Cavarroc, C., Yaitskova, N., Fusco, T., and Vérinaud, C. Comparison of coronagraphs for high-contrast imaging in the context of extremely large telescopes. *A&A*, 492(1):289–300, 2008.

[50] R. Mazzoleni, F. Gonté, I. Surdej, C. Araujo, R. Brast, F. Derie, P. Duhoux, C. Dupuy, C. Frank, R. Karban, L. Noethe, and N. Yaitskova. Design and performances of the Shack-Hartmann sensor within the Active Phasing Experiment. volume 7012, page 70123A. SPIE, 2008.

[51] S. Meimon, E. Delavaquerie, F. Cassaing, T. Fusco, L. M. Mugnier, and V. Michau. Phasing segmented telescopes with long-exposure phase diversity images. volume 7012, page 701214. SPIE, 2008.

[52] L. Mertz. *Excursions in astronomical optics*. Springer, 1996.

[53] MMT. The Multiple Mirror Telescope website, 2011. URL: http://www.mmto.org/.

[54] L. Montoya-Martinez, M. Reyes, A. Schumacher, and E. Hernandez. DIPSI: the diffraction image phase sensing instrument for APE. volume 6267, page 626732. SPIE, 2006.

[55] J. Nelson. Segmented Mirror Telescopes. In R. Foy & F. C. Foy, editor, *NATO ASIB Proc. 198: Optics in astrophysics*, page 61, January 2005.

[56] J. Nelson. Thirty-Meter Telescope: progress and approaches. volume 6986, page 698602. SPIE, 2008.

[57] J. Nelson and G. H. Sanders. The status of the Thirty Meter Telescope project. volume 7012, page 70121A. SPIE, 2008.

[58] L. Noethe. History of mirror casting, figuring, segmentation and active optics. *Experimental Astronomy*, 26:1–18.

[59] L. Noethe. Analytical expressions for optimum alignment modes of highly segmented mirrors. *Journal of Modern Optics*, 52(4):603–632, March 2005.

[60] L. Noethe and H.M. Adorf. Optical measurements of phase steps in segmented mirrors - fundamental precision limits. *Journal of Modern Optics*, April 2006.

[61] E-ELT Science Office. An expanded view of the universe, 2009.

[62] R. G. Paxman and J. R. Fienup. Optical misalignment sensing and image reconstruction using phase diversity. *J. Opt. Soc. Am. A*, 5(6):914–923, Jun 1988.

[63] E. Pinna. *Study and Characterization of the Pyramid Wavefront Sensor for Cophasing*. PhD thesis, Universita Degli Studi Di Firenze, 2009.

[64] E. Pinna, S. Esposito, A. Puglisi, F. Pieralli, R. M. Myers, L. Busoni, A. Tozzi, and P. Stefanini. Phase ambiguity solution with the Pyramid Phasing Sensor. volume 6267, page 62672Y. SPIE, 2006.

[65] E. Pinna, F. Quiros-Pacheco, S. Esposito, A. Puglisi, and P. Stefanini. The pyramid phasing sensor (PYPS). volume 7012, page 70123D. SPIE, 2008.

[66] R. Ragazzoni. Pupil plane wavefront sensing with an oscillating prism. *Journal of Modern Optics*, 43(2):289–293, 1996.

[67] C. Roddier and F. Roddier. Wave-front reconstruction from defocused images and the testing of ground-based optical telescopes. *J. Opt. Soc. Am. A*, 10(11):2277–2287, 1993.

[68] F. Roddier. Curvature sensing and compensation: a new concept in adaptive optics. *Appl. Opt.*, 27(7):1223–1225, 1988.

[69] J. M. Rodriguez-Gonzalez and J. J. Fuensalida. Diffractional treatment of curvature sensing in segmented-mirror telescopes. volume 4837, pages 726–736. SPIE, 2003.

[70] J. M. Rodriguez-Ramos and J. J. Fuensalida. Phasing of segmented mirrors: new algorithm and numerical results for piston detection. volume 4003, pages 270–278. SPIE, 2000.

[71] A. Schumacher and N. Devaney. Phasing segmented mirrors using defocused images at visible wavelengths. *Monthly Notices- Royal Astronomical Society*, 366(2):537–546, 2006.

[72] A. Schumacher, N. Devaney, and L. Montoya. Phasing segmented mirrors: a modification of the Keck narrow-band technique and its application to extremely large telescopes. *Appl. Opt.*, 41(7):1297–1307, 2002.

[73] I. Surdej, E. Koenig, N. Yaitskova, and B. Vandame. APE segment pattern recognition in new phasing techniques. volume 6267, page 626738. SPIE, 2006.

[74] I. Surdej, H. Lorch, L. Noethe, N. Yaitskova, and R. Karban. Pattern recognition and signal analysis in a Mach-Zehnder type phasing sensor. volume 6696, page 66960L. SPIE, 2007.

[75] I. Surdej, N. Yaitskova, and F. Gonté. On-sky performance of the Zernike Phase Contrast Sensor for the phasing of segmented telescopes. *Appl. Opt.*, 49(21):4053–4063, Jul 2010.

[76] TMT. The Thirty Meter Telescope website, 2011. URL: http://www.tmt.org/.

[77] M. Troy and G. Chanan. Diffraction Effects from Giant Segmented-Mirror Telescopes. *Appl. Opt.*, 42(19):3745–3753, 2003.

[78] A. Vigan, K. Dohlen, and S. Mazzanti. On-sky multi-wavelength phasing of segmented telescopes with the Zernike Phase Contrast Sensor. *Appl. Opt.*, 50(17):2708–2718, Jun 2011.

[79] A. Vigan, K. Dohlen, I. Surdej, N. Yaitskova, and F. Y. J. Gonté. On-sky results of the ZEUS phasing sensor, closed loop measurement precision in the context of multi-wavelength measurements. volume 7733. SPIE, 2010.

[80] R. Wilhelm, B. Luong, A. Courteville, S. Estival, F. Gonté, and N. Schuhler. Dual-wavelength low-coherence instantaneous phase-shifting interferometer to measure the shape of a segmented mirror with subnanometer precision. *Appl. Opt.*, 47(29):5473–5491, 2008.

[81] N. Yaitskova. Performance analysis of Mach-Zehnder interferometer for detection of wavefront discontinuities. volume 5169, pages 62–71. SPIE, 2003.

[82] N. Yaitskova. Influence of irregular gaps between primary mirror segments on telescope image quality. *J. Opt. Soc. Am. A*, 24(9):2558–2567, 2007.

[83] N. Yaitskova. Adaptive optics correction of segment aberration. *J. Opt. Soc. Am. A*, 26(1):59–71, 2009.

[84] N. Yaitskova, K. Dohlen, and P. Dierickx. Analytical study of diffraction effects in extremely large segmented telescopes. *J. Opt. Soc. Am. A*, 20(8):1563–1575, 2003.

[85] N. Yaitskova, K. Dohlen, and P. Dierickx. Diffraction in OWL: Effects of segmentation and segments edge misfigure. volume 4840, pages 171–182. SPIE, 2003.

[86] N. Yaitskova, K. Dohlen, P. Dierickx, and L. Montoya. Mach-Zehnder interferometer for piston and tip-tilt sensing in segmented telescopes: theory and analytical treatment. *J. Opt. Soc. Am. A*, 22(6):1093–1105, 2005.

[87] N. Yaitskova, F. Gonté, F. Derie, L. Noethe, I. Surdej, R. Karban, K. Dohlen, M. Langlois, S. Esposito, E. Pinna, M. Reyes, L. Montoya, and D. Terrett. The Active Phasing Experiment: Part I. Concept and objectives. volume 6267, page 62672Z. SPIE, 2006.

[88] N. Yaitskova, L. Montoya-Martinez, K. Dohlen, and P. Dierickx. A Mach-Zehnder phasing sensor for extremely large segmented telescopes: laboratory results and close-loop algorithm. volume 5489, pages 1139–1151. SPIE, 2004.

[89] N. Yaitskova and I. Surdej. ZErnike Unit Sensor (ZEUS) : from theory to performance on sky and back to theory. Technical Report GEN-TRE-ESO-21120- 0055, ESO, 2009.

[90] N. Yaitskova and M. Troy. Rolled edges and phasing of segmented telescopes. *Appl. Opt.*, 50(4):542–553, Feb 2011.

[91] F. Zernike. How I Discovered Phase Contrast. *Science*, 121:345–349, 1955.

[92] F. Zernike. Diffraction theory of the knife-edge test and its improved form, the phase-contrast method. *Journal of Microlithography, Microfabrication, and Microsystems*, 1(2):87–94, 2002.